NUMERICAL METHODS FOR COLD ATOM SYSTEMS

BY

SHENGQUAN ZHOU

DISSERTATION

Submitted in partial fulfillment of the requirements
for the degree of Doctor of Philosophy in Physics
in the Graduate College of the
University of Illinois at Urbana-Champaign, 2012

Urbana, Illinois

Doctoral Committee:

Professor Philip W Phillips, Chair
Professor David M Ceperley, Director of Research
Professor Brian L Demarco
Professor Michael T Heath
Professor John D Stack

Abstract

The control afforded by Feshbach resonance phenomena has enabled the exploration of strongly interacting degenerate regimes in dilute ultracold atomic alkali-gases. In these dilute systems, interactions are characterized by a single parameter, the s-wave scattering length. In this dissertation, we review the physics of quantum degenerate atomic gases from a theoretical perspective and present the applications of non-perturbative numerical methods ranging from exact diagonalization to quantum Monte Carlo techniques. Emphasis is given to the effect of interactions. A major goal of this work is to compare theoretical predictions with available experimental results.

We begin by introducing the effective interactions in the many-body alkali-gas system. As simplifications of the real interaction between two alkali atoms, the resonance properties of various short range models, the zero-range model and the two-channel model are investigated. The fundamental result is that under appropriate conditions, the true interaction potential $V(\mathbf{r})$ of two atoms may be replaced by a regularized δ-function of strength $4\pi\hbar^2 a/m$, where a is the low-energy s-wave scattering length.

In collaboration with experimentalists in our department, we developed a unique method to construct localized single-particle wave functions using imaginary time projection and thereby determine lattice Hamiltonian parameters. Our method enables an efficient coarse-grained mapping from a continuum system to a lattice model. We apply the method to a specific disordered potential generated by an optical lattice experiment and calculate for each instance of disorder the equivalent lattice model parameters. Detailed statistical analysis is performed on the resulting probability distributions of the Hubbard parameters.

In the final part, we study the pairing and ferromagnetic instabilities in systems of spin-

1/2 fermions. To interpret a recent experimental study of the possibility of itinerant ferromagnetism in cold atom systems, we investigate the energy spectrum of a system of four spin-1/2 fermions with short range attractive interactions both exactly and within the scattering length approximation. The formation of molecular bound states and the ferromagnetic transition of the excited scattering state are examined systematically as a function of the two-body scattering length. We show that an adiabatic ferromagnetic transition occurs, but at a critical transition point $k_F a$ much higher than predictions from the scattering length approximations. The exact critical interaction strength calculated in the four-particle system is consistent with that reported by experiment. Finally, by constructing a many-body wavefunction satisfying the Bethe-Peierls boundary conditions, we attempted the first variational Monte Carlo calculations of the zero-range model of unitary Fermion gases, eliminating the need for short-range approximations employed by existing QMC calculations.

To my parents and my wife.

Acknowledgments

I am grateful to my advisor, Professor David Ceperley, who provided me with interesting research problems and a supporting atmosphere to work on them. This thesis would not have been possible without his guidance and support. In the six years I worked with him, I developed a respect not only for Professor Ceperley's deep insights and broad knowledge, but also for his great patience and willingness to spend time discussing physics with his students. I could always expect a push forward from our discussions when difficulties made it hard to progress on my research. I also enjoyed listening to his comments on physics, computer programming, experimental mathematics and English writing. It has been a privilege to learn from him over the years.

My research work has been supported with funds from the DARPA OLE Program and ARO (Grant No. 56693PH) and computer time at NCSA.

Table of Contents

List of Tables

List of Figures

Chapter 1

Foreword

1.1 Simulation of cold atom systems

Material properties such as conductivity and magnetism have widespread applications in the electronic components of everyday modern devices. The ability to understand and explain these properties is crucial to the exploitation of materials. The advancement in cold atom experiments in the past decade underlies the potential of ultra-cold atoms as nearly perfectly controlled model systems to study the properties of various types of complex materials, such as high-temperature superconductors and novel magnetic materials that could have applications one day in data storage and improving energy efficiency. This provides an opportunity to compare quantitatively experimental results with parameter free theoretical calculations.

Simulation is the only general method for solving many-body problems. Computer simulation of matter at the atomic scale has been performed since the early days of digital computing. Over the years, the numerical methods have grown in complexity and accuracy, from classical molecular dynamics to fully quantum mechanical simulations.

In Sect. (1.2), we briefly describe the physics of cooling and trapping atoms. In Sect. (1.3), we outline the numerical methods used in this work and the details will be elaborated in Chapter 4 and Chapter 5.

1.2 Cooling and trapping of alkali atoms

Before describing in detail the White *et al.* experiment [1] in Chapter 3 and the Jo *et al.* experiment [2] in Chapter 5, we introduce the basic concepts related to the experimental

techniques of cooling and trapping alkali atoms.

Neutral atoms contain equal numbers of electrons and protons, and therefore the statistics that a neutral atom obey is determined by the number of neutrons N: if N is even, the atom is a boson, and if it is odd, a fermion. Note that alkalis have odd atomic number Z. In Table 1.1 we list N, Z, the nuclear spin quantum number I for some alkali atoms and hydrogen, and the associated nuclear magnetic moment μ which is defined as the expectation value of the z component of the magnetic moment operator in the state where the z component of the nuclear spin, denoted by $m_I\hbar$, has its maximum value [3][4].

Table 1.1: *The proton number Z, the neutron number N, the nuclear spin I, the nuclear magnetic moment μ (in units of the nuclear magneton $\mu_N = e\hbar/2m_p$), and the hyperfine splitting $\nu_{\rm hf} = \Delta E_{\rm hf}/h$ for hydrogen and some alkali isotopes.*

Isotope	Z	N	I	μ/μ_N	$\nu_{\rm hf}$ (MHz)
^{1}H	1	0	1/2	2.793	1420
^{6}Li	3	3	1	0.822	228
^{7}Li	3	4	3/2	3.256	804
^{23}Na	11	12	3/2	2.218	1772
^{39}K	19	20	3/2	0.391	462
^{40}K	19	21	4	−1.298	−1286
^{41}K	19	22	3/2	0.215	254
^{85}Rb	37	48	5/2	1.353	3036
^{87}Rb	37	50	3/2	2.751	6835
^{133}Cs	55	78	7/2	2.579	9193

1.2.1 Hyperfine splitting

In the electronic ground state of alkali atoms, all electrons but one occupy closed shells, and the remaining one is in an s-orbital in a higher shell. For example, the electron configuration for Li is $1s^2 2s^1$. The nuclear spin is coupled to the electronic spin by the *hyperfine interaction*. The magnetic hyperfine splitting effect is especially noticeable for levels due to an outer electron in the s-state, owing to the comparatively high probability that such an electron will be near the nucleus. Since the electrons have no orbital angular momentum ($L = 0$), there is no magnetic field at the nucleus due to the orbital motion, and the coupling arises solely

due to the magnetic field produced by the electronic spin. The coupling of the electronic spin, $S = 1/2$, to the nuclear spin I yields the two possibilities $F = I \pm 1/2$ for the quantum number F for the total spin, according to the rules for addition of angular momentum.

In the absence of an external magnetic field the atomic levels are split by the hyperfine interaction. A simple model of the coupling is represented by a term $H_{\rm hf}$ in the Hamiltonian of the form

$$\hat{H}_{\rm hf} = A\mathbf{I} \cdot \mathbf{J}, \tag{1.1}$$

where A is called hyperfine constant, while $\mathbf{I}$ and $\mathbf{J}$ are the operators for the nuclear spin and the electronic angular momentum, respectively, in units of $\hbar$. Denote the total angular momentum $\mathbf{F} = \mathbf{I} + \mathbf{J}$, we find

$$\mathbf{I} \cdot \mathbf{J} = \frac{1}{2}\left[F(F+1) - I(I+1) - J(J+1)\right]. \tag{1.2}$$

For alkali and hydrogen atoms, $J = S = 1/2$, the splitting between $F = I \pm 1/2$ states is therefore given by

$$\Delta E_{\rm hf} = E_{I+1/2} - E_{I-1/2} = h\nu_{\rm hf} = \left(I + \frac{1}{2}\right) A. \tag{1.3}$$

For ^{6}Li, we have $E_{3/2} = A/2$, $E_{1/2} = -A$ and thus $\Delta E_{\rm hf} = 3A/2$. Typical values range between 1 and 10GHz. Measured values of the hyperfine splitting are given in Table 1.1.

1.2.2 Trapping of atoms

Magnetic trap

The effect of external magnetic field on the energy levels of an atom is taken into account by adding to the hyperfine Hamiltonian Eq.(1.1) the Zeeman terms arising from the interaction of the magnetic moment of the electron and the nucleus with the magnetic field. If we take the magnetic field $\mathbf{B}$ to be in the z direction, the total Hamiltonian is

$$H_{\rm spin} = A\mathbf{I} \cdot \mathbf{J} + CJ_z + DI_z, \tag{1.4}$$

where $C = g\mu_B B$ for $L = 0$ and $S = 1/2$, and $D = -\mu B/I$. Note that the leading radiative correction to the electron g factor is $g = 2(1 + \alpha/2\pi)$. Since $|C/D| \sim m_{\rm p}/m_{\rm e} \approx 2000$, for most applications D may be neglected. At the same level of approximation, the electron g factor may be put equal to 2.

The Hamiltonian Eq.(1.4) can be solved by diagonalization in a basis consisting of $(2I + 1) \times (2J + 1)$ states $|m_I, m_J\rangle$. Note that Hamiltonian Eq.(1.4) conserves the z component of the total angular momentum, and therefore it couples only states with the same value of the sum $m_F = m_I + m_J$. We list the eigenenergies $E(m_F)$ and eigenstates $|m_I, m_J\rangle$ for the nuclear spin $I = 1$ corresponding to ^{6}Li:

$$
\begin{aligned}
&|+1,+1/2\rangle: \quad E = \frac{1}{2} + \frac{b}{2},\\
&|-1,-1/2\rangle: \quad E = \frac{1}{2} - \frac{b}{2},\\
&\{|+1,-1/2\rangle,\, |0,+1/2\rangle\}: \quad E = -\frac{1}{4} \pm \frac{1}{2}\sqrt{\frac{9}{4} + b + b^2},\\
&\{|-1,+1/2\rangle,\, |0,-1/2\rangle\}: \quad E = -\frac{1}{4} \pm \frac{1}{2}\sqrt{\frac{9}{4} - b + b^2}
\end{aligned}
$$

and for the nuclear spin $I = 3/2$ corresponding to ^{23}Na:

$$
\begin{aligned}
&|+3/2,+1/2\rangle: \quad E = \frac{3}{4} + \frac{b}{2},\\
&|-3/2,-1/2\rangle: \quad E = \frac{3}{4} - \frac{b}{2},\\
&\{|+3/2,-1/2\rangle,\, |+1/2,+1/2\rangle\}: \quad E = -\frac{1}{4} \pm \sqrt{1 + \frac{b}{2} + \frac{b^2}{4}},\\
&\{|-3/2,+1/2\rangle,\, |-1/2,-1/2\rangle\}: \quad E = -\frac{1}{4} \pm \sqrt{1 - \frac{b}{2} + \frac{b^2}{4}},\\
&\{|-1/2,+1/2\rangle,\, |+1/2,-1/2\rangle\}: \quad E = -\frac{1}{4} \pm \sqrt{1 + \frac{b^2}{4}},
\end{aligned}
$$

where the energies are in units of hyperfine constant A and the dimensionless quantity

$$b = \frac{C}{A} = \frac{(2I+1)\mu_B B}{\Delta E_{\rm hf}}$$

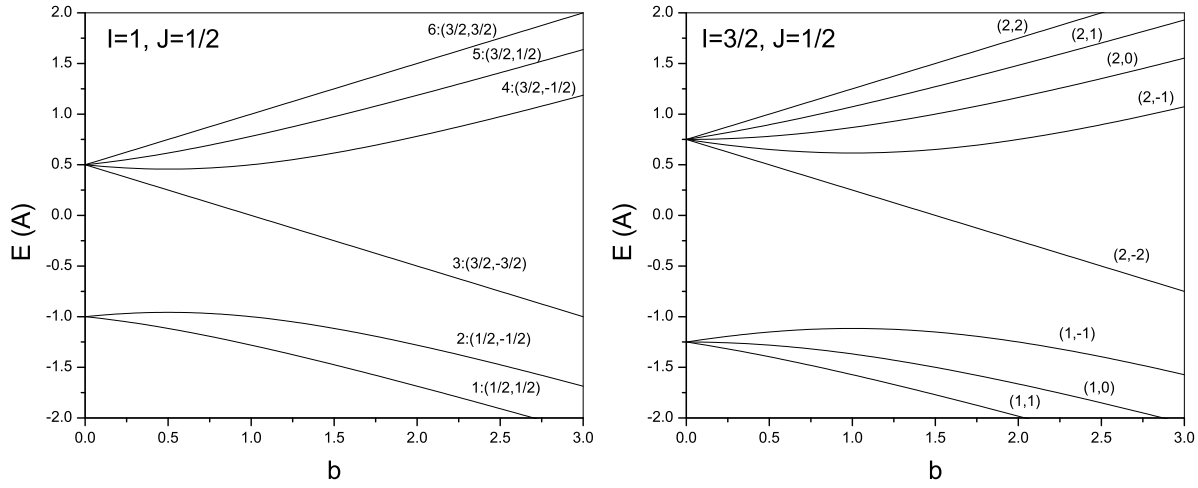

Figure 1.1: For a simple model of hyperfine splitting in magnetic trap $\hat{H}_{\rm hf} = A\mathbf{I}\cdot\mathbf{J} + CJ_z$, where A is called hyperfine constant and $\mathbf{I}$ and $\mathbf{J}$ are the operators for the nuclear spin and the electronic angular momentum, respectively, in units of $\hbar$. The magnetic field is characterized by $b = C/A$. Hyperfine levels are labeled by (F, m_F). **Left**: Hyperfine splittings of ^{6}Li in the presence of magnetic field. **Right**: Hyperfine splittings of ^{23}Na in the presence of magnetic field.

characterizes the strength of the external magnetic field.

Magnetic trapping of neutral atoms is due to the Zeeman effect: the energy of an atomic state depends on the magnetic field, and therefore an atom in an inhomogeneous magnetic field experiences a spatially-varying potential. The atoms experiencing a force tending to drive it to regions of higher field are referred to as *high-field seekers*, and those experiencing a force towards regions of lower field as *low-field seekers*. The task of constructing a magnetic trap is thus to design magnetic field configurations with either a local minimum in the magnitude of the magnetic field, or a local maximum. The latter possibility is ruled out by a general theorem that a local maximum in $|\mathbf{B}|$ is impossible in regions where there are no electrical currents [6].

Many cold atom experiments on alkali atoms are performed in low magnetic fields, for which the Zeeman energies are small compared with the hyperfine splitting. To first order in the magnetic field, the energy may be written as

$$E(F, m_F) \approx E(F) + g_L m_F \mu_B B + \cdots \tag{1.5}$$

where $g_L = \frac{F(F+1)+J(J+1)-I(I+1)}{2F(F+1)}$ is the Lande factor and $E(F)$ is the energy in the absence of magnetic fields. Thus, the energy of an atom in a particular state i may then be written as $E(F, m_F) = C_i - \mu_i B$ where μ_i is the magnetic moment of the state and C_i is a constant. The atoms with a positive magnetic moment are high-field seekers and those with a negative one are low-field seekers. The rich structure of the atomic levels exhibited by the alkalis opens the possibilities of trapping atoms in different magnetic states, with the consequent possibility of generating mixtures of different species of atoms in the same trap, and the possibility of inducing transitions between trapped and untrapped states, thereby controlling the mechanism of evaporation, see Sect. (1.2.3).

Optical trap

Optical trap is formed by electromagnetic radiation, especially lasers. However, the frequency of this laser is usually much higher than the hyperfine splittings and tuned faraway from resonance, so that it does not cause transitions between internal states of the atoms. The interaction between an atom and the electric field is given in the dipole approximation by $H' = -\mathbf{d} \cdot \mathcal{E}$, where $\mathbf{d}$ is the electric dipole moment operator and $\mathcal{E}$ is a time-harmonic electric field with frequency ω. The second-order perturbation theory gives the energy shift of the ground state

$$\Delta E_0 = -\frac{1}{2}\alpha(\omega)\langle \mathcal{E}^2(\mathbf{r}, t)\rangle_t, \tag{1.6}$$

where $\langle \cdots \rangle_t$ denotes a time average, and the dynamical polarizability is given by

$$\alpha(\omega) = \sum_{i \neq 0} |\langle i|\mathbf{d} \cdot \hat{\epsilon}|0\rangle|^2 \left(\frac{1}{E_i - E_0 + \hbar\omega} + \frac{1}{E_i - E_0 - \hbar\omega} \right). \tag{1.7}$$

Differently from the case of the magnetic interaction energy Eq. (1.5), which is linear in B due to the intrinsic magnetic moment of the atom, the electric interaction energy Eq. (1.6) is quadratic in E as a result of the dipole atomic polarizability. In many situations of interest the frequency of the radiation is close to that of an atomic resonance, and it is then a good approximation to neglect all transitions except the resonant one. The polarizability then

reduces to a single term and the finite lifetime due to spontaneous emission of photons can be taken into account phenomenologically by attributing to the excited state an energy with both real and imaginary parts

$$\alpha(\omega)\Big|_{\text{near resonance}} \approx \frac{|\langle i|\mathbf{d}\cdot\hat{\epsilon}|0\rangle|^2}{E_i - i\hbar\Gamma_i/2 - E_0 - \hbar\omega}. \tag{1.8}$$

The shift of the energy level is thus given by

$$V_0(\mathbf{r}) = -\frac{1}{2}\Re\alpha(\omega)\langle\mathcal{E}^2(\mathbf{r},t)\rangle_t, \tag{1.9}$$

where the real part of the polarizability is $\Re\alpha(\omega)\Big|_{\text{near resonance}} \approx -\frac{\hbar^{-1}\delta}{\delta^2+\Gamma_i^2/4}|\langle i|\mathbf{d}\cdot\hat{\epsilon}|0\rangle|^2$ and the difference between the laser frequency and the resonant frequency is defined to the detuning

$$\delta \equiv \omega - \hbar^{-1}(E_i - E_0) = \omega - \omega_{i,0}. \tag{1.10}$$

Positive δ is referred to as *blue detuning* and negative δ as *red detuning*. The rate of loss of atoms from the ground state is given by

$$\Gamma_0 = \frac{1}{\hbar}\Im\alpha(\omega)\langle\mathcal{E}^2(\mathbf{r},t)\rangle_t, \tag{1.11}$$

where the imaginary part of the the polarizability is $\Im\alpha(\omega)\Big|_{\text{near resonance}} \approx \frac{\hbar^{-1}\Gamma_i/2}{\delta^2+\Gamma_i^2/4}|\langle i|\mathbf{d}\cdot\hat{\epsilon}|0\rangle|^2$.

During an absorption or an emission process the momentum of a photon is imparted to or removed from an atom. The rate of absorption of photons by an atom in the ground state is equal to the rate of excitation of the ground state. Therefore if the radiation field is a traveling wave with wave vector $\mathbf{q}$, the total force on the atom due to the absorption process is $\mathbf{F}_{\text{rad}} = \hbar\mathbf{q}\Gamma_0$. This is referred to as *radiation pressure*. Both this force and the energy shift Eq.(1.9) play an important role in optical trapping and cooling. The perturbative treatment given above is valid provided $|\langle i|\mathbf{d}\cdot\hat{\epsilon}|0\rangle| \ll \hbar\sqrt{\delta^2+\Gamma_i^2/4}$. Under most conditions relevant for experiments in cold atom systems, electric fields are weak enough that the perturbative approach is adequate.

By focusing a laser beam it is possible to create a radiation field whose intensity has a maximum in space. If the frequency of the light is detuned to the red, the energy of the ground-state atom $V_0(\mathbf{r})$ has a spatial minimum, and therefore it is possible to trap atoms. One advantage of optical traps is that the potential experienced by an alkali atom in its ground state is essentially independent of the magnetic substates (degeneracy from the quantum number m). This is due to the outermost electron in the ground state of alkali atoms being in an s-state. Optical traps are also important in the context of Feshbach resonances as we shall introduce later. In the vicinity of such a resonance the effective interaction is a strong function of the magnetic field, and therefore it is desirable that the magnetic field be homogeneous. This may be achieved by applying a uniform magnetic field to atoms in an optical trap, but it is not possible with magnetic traps, since without inhomogeneity of the magnetic field there is no trapping.

Magneto-optical trap

Radiation pressure may also be used to confine atoms in space. In the magneto-optical trap (MOT) this is done with the combination of laser beams and a spatially-varying magnetic field. The basic physical effect is that, because atomic levels and the frequencies of transition between them depend on the magnetic field, and magnetic field depends on position, so the radiation pressure depends on position. The use of MOT's is a universal feature of experiments on cold alkali atoms. Not only do they trap atoms, but they also cool them as we shall describe below.

1.2.3 Cooling of atoms

Since laboratory magnetic fields are generally considerable less than 1 tesla, the temperature must be cooled down to $T < \mu_B B \approx 0.67\,\mathrm{K/T} \times 1\,\mathrm{T} = 0.67\,\mathrm{K}$ in order for the atoms to be trapped by magnetic fields. To reduce heating of atoms by absorption of photons, the laser frequency in optical traps must be chosen away from atomic resonances. The resulting optical traps are shallow ($\sim \mu$K) and therefore atoms must be cooled in other sorts of traps

before they can be held by purely optical forces.

Doppler cooling utilizes the laser beams that is tuned to lie just below the frequency of an atomic transition between an excited state $|i\rangle$ and the ground state $|0\rangle$. Because the laser is detuned to the red, the atoms will absorb more photons if they move in the opposite direction of the laser beam, due to the Doppler effect. Thus if one applies light from two opposite directions, the atoms will always absorb more photons from the laser beam pointing opposite to their direction of motion. The result of the absorption and emission process is to reduce the speed of the atom and the lowest temperature attainable by this mechanism is given by the decay rate of the excited state $|i\rangle$

$$k_B T_{\text{Doppler}} = \frac{\hbar \Gamma_i}{2}. \tag{1.12}$$

The Doppler cooling limit for lithium is about $140\,\mu$K.

Sisyphus cooling is a mechanism through which atoms can be cooled using laser beams below the temperatures expected to be achieved by Doppler cooling. Atoms moving through the potential landscape created by the standing wave (created by the interference of the two counterpropagating beams) lose kinetic energy as they move to a potential maximum, at which point optical pumping moves them to a lower-energy state, thus losing the potential energy they had. The process of losing kinetic energy followed by optical pumping will be repeated and thereby leading to continual cooling of the atoms to temperatures corresponding to a thermal energy of order the so-called recoil energy

$$k_B T_{\text{Sisyphus}} = E_R = \frac{\hbar^2 q^2}{2m}. \tag{1.13}$$

This is the energy imparted to an atom at rest when it absorbs a photon of momentum $\hbar q$. These temperatures lie several orders of magnitude below the lowest temperature by the Doppler mechanism. The atomic transitions have energies on the scale of electron volts, while the rest mass of an atom is $\sim A$ GeV, where A is the mass number of the atom. The recoil energy is therefore $6 \times 10^{-6} (\hbar\omega/1\text{eV})^2/A$ K, which is of order $0.1 \sim 1\,\mu$K.

In the experiments performed to date, condensation for bosons is achieved by using *evaporative cooling* after laser cooling. The basic physical effect in evaporative cooling is that, if particles escaping from the system have an energy higher than the average energy of particles in the system, the remaining particles are cooled. In practice one applies radio-frequency (RF) radiation that flips the spin state of an atom from a low-field seeker one to a high-field seeker one, thereby expelling the atom from the magnetic trap. Since the resonant frequency depends on position as a consequence of the Zeeman effect of an inhomogeneous magnetic field, the frequency of the RF radiation can be steadily adjusted to allow loss of atoms with lower and lower energy.

However, the rate of evaporation depends on the energy threshold and the rate of elastic collisions between atoms in the gas, since collisions are responsible for scattering atoms into states at energies high enough for evaporation to occur. The elastic collision rate, which governs the effectiveness of evaporative cooling, behaves differently for fermions and bosons when gases become degenerate. For identical fermions like ^{6}Li, the requirement of antisymmetry of the wave function forces the scattering cross section to vanish at low energy and therefore evaporative cooling with a single species of fermion, with all atoms in the same internal state, cannot work. This difficulty may be overcome by using a mixture of two types of atoms, either two different fermions, which could be different hyperfine states of the same fermionic isotope, or a boson and a fermion. This process is referred to as *sympathetic cooling*. The lowest experimentally obtained temperature to date is $T/T_F \sim 0.05$ [7].

1.3 Numerical methods

1.3.1 Exact diagonalization

Exact diagonalization methods are important tools for studying the physical properties of quantum many-body systems. These methods typically are used to determine a few of the lowest eigenvalues and eigenvectors of models of many-body systems on a finite lattice (grid). From these eigenvalues and eigenstates, various ground state expectation values and correlation functions are easily computed. The complexity of fully quantum calculations

grows exponentially with the number of particles involved, so the methods are limited to small lattice sizes. However, they not only provide useful benchmarks for approximate theoretical calculations and quantum Monte Carlo simulations, but also provide helpful insight into the subtle properties of unsolvable many-body problems in the thermodynamic limit.

The direct diagonalization scheme of a Hermitian matrix, which produces the whole spectrum of eigenvalues, involves a tri-diagonalization phase followed by an iterative diagonalization phase. The complexity of the direct scheme is $O(n^3)$, where n is the matrix dimension, i.e. the total number of sites (grid points) in a lattice model. However, many quantum many-particle problems lead to a sparse matrix representation of the Hamiltonian, where only a small fraction of the matrix elements are non-zero. The preferred diagonalization methods are iterative, i.e. the Hamiltonian matrix $\hat{H}$ is applied repeatedly to a set of vectors from the Hilbert space. The commonly used projectors include the Lanczos iteration, imaginary time evolution operator $e^{-\tau\hat{H}}$ and Green's function operator $(\mathbf{I}-\tau\hat{H})$. Thus, the main programming effort is efficiently performing a matrix-vector multiplication. The complexity of a typical matrix-vector multiply is $O(n^2)$, but for a sparse matrix where only a constant number of elements in each row are non-zero, the complexity of each iteration step is reduced to $O(n)$ for a single state and $O(mn)$ for a set of m state. In addition, orthogonalization is required at each step of the iteration with a complexity of $O(m^2n)$. Thus, the computation time of this algorithm is linear in the number of grid points and the complexity is proportional to

$$(\#\text{ of steps})(\text{const}\times mn+\text{const}\times m^2n), \tag{1.14}$$

where m is the number of states and n is the matrix dimension, i.e. the number of grid points.

The key step to make the problem more tractable is the use of symmetries to block-diagonalize the Hamiltonian. This step produces sequences of smaller matrices along the diagonal by similarity transformations. At implementation level, this can be achieved by

construction of basis states satisfying the prescribed symmetries or by properly symmetrize the state vectors at each step of the projection. Detailed discussion will be found in Chapter 4.

The main limitation of this method is its restriction to small lattices, and thus properties in the thermodynamic limit are difficult to obtain. However, the results for the small lattice might meaningfully represent those of the large systems because many-body interactions are short-ranged and can lead to phenomena with short coherence lengths. If this length is smaller than the lattice size accessible by the exact diagonalization method, physically meaningful results are obtained. In other cases, an extrapolation of results for finite sizes to infinite system sizes (or for discrete grid to continuum systems) is possible. Such extrapolation processes are used in the exact calculations of the ferromagnetic transition of a four-fermion system in Chapter 5.

1.3.2 Metropolis Monte Carlo

The concept of Monte Carlo sampling is equally important for classical, statistical and quantum physical problems. In Metropolis Monte Carlo, a given probability distribution for the atoms is sampled directly using a stochastic method. More specifically, a random change in the positions of the atoms is proposed, and the proposed move is then accepted or rejected based on the ratio of weighting factors of the old and new configurations.

To calculate the expectation value of an observable $\hat{O}$ of a system of N particles in variational Monte Carlo, the weighting factor is chosen to be the squared-norm of the trial wavefunction $|\Psi_T|^2$

$$\langle \hat{O} \rangle = \frac{\int \prod_{i=1}^{N} d^3\mathbf{r}_i \Psi_T^*(\mathbf{r}_1, \cdots, \mathbf{r}_N) \hat{O} \Psi_T(\mathbf{r}_1, \cdots, \mathbf{r}_N)}{\int \prod_{i=1}^{N} d^3\mathbf{r}_i |\Psi_T(\mathbf{r}_1, \cdots, \mathbf{r}_N)|^2}. \tag{1.15}$$

The Monte Carlo algorithm generates a sequence of configurations $\mathbf{R}^{(n)} = \{\mathbf{r}_1^{(n)}, \cdots, \mathbf{r}_N^{(n)}\}$ such that at long time $n \to \infty$ the probability distribution converges to $|\Psi_T|^2$. Monte Carlo

integration estimates the mean of an observable,

$$\langle \hat{O} \rangle \approx \bar{O} \pm \sqrt{\frac{\bar{O^2} - \bar{O}^2}{\mathcal{N}}}, \tag{1.16}$$

where the bar notation on the right hand side denotes taking the arithmetic mean over the $\mathcal{N}$ sample points

$$\bar{O} = \frac{1}{\mathcal{N}} \sum_{n=1}^{\mathcal{N}} O(\mathbf{R}^{(n)}), \quad \bar{O^2} = \frac{1}{\mathcal{N}} \sum_{n=1}^{\mathcal{N}} O^2(\mathbf{R}^{(n)}). \tag{1.17}$$

Here $O(\mathbf{R}^{(n)})$ is called an *estimator* for the observable $\hat{O}$. Any properties calculated from a Monte Carlo simulation necessarily have an associated statistical error, which should always be quoted with published simulation data. These errors can always be reduced by running the simulation longer, assuming that the probability distribution being sampled has a finite variance. It is important to ensure that the sample points are sufficiently uncorrelated, otherwise the statistical error is underestimated. In Metropolis Monte Carlo, a new sample point is generated based on the acceptance or rejection of the old one, which makes the sequence of sample points inevitably correlated. An analysis of auto-correlation time in Monte Carlo steps is then required and block average is used to estimate the statistical error. In this case, $\mathcal{N}$ in Eq. (1.16) refers to the number independent sample points or blocks. According to Gauss' central limit theorem, given enough averaging, the probability distribution of the mean will approach Gaussian as long as the variance is not infinite.

References

[1] M. White, M. Pasienski, D. McKay, S. Q. Zhou, D. Ceperley, and B. DeMarco. Strongly interacting bosons in a disordered optical lattice. *Phys. Rev. Lett.*, 102:055301, Feb 2009.

[2] Gyu-Boong Jo, Ye-Ryoung Lee, Jae-Hoon Choi, Caleb A. Christensen, Tony H. Kim, Joseph H. Thywissen, David E. Pritchard, and Wolfgang Ketterle. Itinerant ferromagnetism in a fermi gas of ultracold atoms. *Science*, 325(5947):1521–1524, 2009.

[3] C. J. Pethick and H. Smith. *Bose-Einstein Condensation in Dilute Gases*. Cambridge University Press, first edition, 2002.

[4] L. Pitaevskii and S. Stringari. *Bose-Einstein Condensation*. Oxford University Press, first edition, 2003.

[5] L. D. Landau and E. M. Lifshitz. *Quantum Mechanics, Non-relativisitic Theory.* Butterworth-Heinemann, third edition, 1981.

[6] William H. Wing. On neutral particle trapping in quasistatic electromagnetic fields. *Progress in Quantum Electronics*, 8(3C4):181 – 199, 1984.

[7] Z. Hadzibabic, S. Gupta, C. A. Stan, C. H. Schunck, M. W. Zwierlein, K. Dieckmann, and W. Ketterle. Fiftyfold improvement in the number of quantum degenerate fermionic atoms. *Phys. Rev. Lett.*, 91:160401, Oct 2003.

[8] J. P. D'Incao and B. D. Esry. Scattering length scaling laws for ultracold three-body collisions. *Phys. Rev. Lett.*, 94:213201, Jun 2005.

Chapter 2

Atomic Scattering

2.1 Basic descriptions

Two-body interactions at low energies are characterized by their scattering lengths. A qualitative argument [3] shows that, for polarized alkali atoms, these scattering lengths are typically about two orders of magnitude greater than the size of an atom $\sim a_0 = \hbar^2/(m_e e^2)$. For large atomic separations, there is an attraction due to the van der Waals interaction caused by the electric dipole-dipole interaction $-\alpha/r^6$, where r is the atomic separation. The length scale r_0 in the Schrödinger equation at zero energy, which sets the basic scale for the scattering length, may be estimated by dimensional arguments to be $r_0 = (\alpha m/\hbar^2)^{1/4}$. On the other hand, the coefficient α must be of the form of a typical atomic energy, e^2/a_0, times the sixth power of the atomic length scale a_0^6, that is $\alpha = C_6 e^2 a_0^5$, where the dimensionless coefficient C_6 gives the strength of the van der Waals interaction in atomic units. Thus the length scale r_0 is given by

$$r_0 = \sqrt[4]{\frac{C_6 m}{m_e}} a_0. \tag{2.1}$$

The large scattering lengths for alkali atoms are thus a consequence of two effects: atomic masses are of order $10^3 A$ times the electron mass m_e and van der Waals coefficients for alkali atoms lie between 10^3 and 10^4, so typical scattering lengths are of order $10^2 a_0$. The numerical values of C_6 are given in [3], $C_6 \approx 6.5$ for H-H, $C_6 \approx 1393$ for Li-Li, $C_6 \approx 1556$ for Na-Na, $C_6 \approx 3897$ for K-K, $C_6 \approx 4691$ for Rb-Rb and $C_6 \approx 6851$ for Cs-Cs. A microscopic expression for C_6 can be derived based on the electric dipole-dipole interaction between

atoms

$$C_6 \approx \frac{3}{4\Delta E_{\rm res}^3}. \tag{2.2}$$

Here ΔE is the energy of the resonance line in atomic units. For the heavier alkali atoms, the actual value of C_6 is greater than the estimate Eq(2.2), while for light atoms hydrogen, lithium and sodium, the estimate is larger than the actual value.

Here we outline the basic scattering theory and introduce the scattering length, which characterizes low-energy interactions between a pair of particles. If we neglect the internal degrees of freedom of the atoms due to the nuclear and electronic spins, at large interatomic separations one writes the wavefunction for the relative motion as the sum of an incoming plane wave and a scattered wave

$$\psi = e^{ikz} + f(\mathbf{k})\frac{e^{ikr}}{r}, \tag{2.3}$$

where $f(\mathbf{k})$ is the *scattering amplitude* and $\mathbf{k}$ specifies the wave vector of the scattered wave. At very low energies it is sufficient to consider s-wave scattering. In this limit $k \to 0$ the scattering amplitude $f(\mathbf{k}) = f(\theta)$ in three dimensions approaches a constant $-a$, the wavefunction Eq(2.3) becomes

$$\psi \sim 1 - \frac{a}{r}. \tag{2.4}$$

The constant a is called the *scattering length*. It can be interpreted as the node, or the intercept of the asymptotic wave function Eq(2.4) on the r-axis. In the presence of interatomic interactions that give rise to transitions between internal states, scattering becomes a multichannel problem. The relative motion of two atoms can be described by the Hamiltonian $\hat{H} = \hat{H}_0 + \hat{V}$, where

$$\hat{H}_0 = \frac{\mathbf{p}^2}{2\mu} + \hat{H}_{\rm spin}(1) + \hat{H}_{\rm spin}(2). \tag{2.5}$$

Here the first term in $\hat{H}_0$ is the kinetic energy operator for the relative motion, and $\hat{H}_{\rm spin}$ is the Hamiltonian corresponding to the internal spin-states, the labels 1 and 2 refer to the

two atoms. The eigenstates of $\hat{H}_0$ may be denoted by $|\alpha\beta\mathbf{k}\rangle$ and the eigenenergies are

$$E_{\alpha\beta}(k_{\alpha\beta}) = \frac{\hbar^2 k_{\alpha\beta}^2}{2\mu} + \epsilon_\alpha + \epsilon_\beta. \tag{2.6}$$

Two atoms initially in the state $|\alpha\beta\rangle$ may be scattered by atom-atom interactions to the state $|\alpha'\beta'\rangle$. The scattering amplitude is introduced to allow for transitions between internal states,

$$|\psi\rangle = e^{i\mathbf{k}_{\alpha\beta}\cdot\mathbf{r}}|\alpha\beta\rangle + \sum_{\alpha'\beta'} f_{\alpha\beta}^{\alpha'\beta'}(\mathbf{k}_{\alpha\beta}, \mathbf{k}'_{\alpha'\beta'})\frac{e^{ik'_{\alpha'\beta'}r}}{r}|\alpha'\beta'\rangle. \tag{2.7}$$

The scattered wave has components in different internal states $|\alpha'\beta'\rangle$ which are referred to as the exit *channels*. Because of the coupling of channels, atoms can be scattered between different magnetic substates.

Two types of resonances play a role in scattering processes: shape or potential resonances and Feshbach resonances. The first occur when a potential well creates bound states in the continuum. A Feshbach resonance, of most concern in ultra-cold atomic scattering, results when true bound states belonging to a closed channel subspace match the energy of open channels and a coupling exists between them so that temporary transitions are possible during the collision process. In this chapter, we discuss the shape or potential resonances in Sect.(2.2) and Sect.(2.3) and Feshbach resonances in Sect.(2.5).

The central postulate of the theory of quantum gases is that the short range details of the interaction are unimportant, only the low-momentum scattering amplitude f_k between two atoms is relevant. As a consequence, any simplified model for the interaction, leading to a different scattering amplitude f_k^{model} , is acceptable provided that

$$f_k^{\text{model}} \approx f_k \tag{2.8}$$

for the relevant values of the relative momentum k distributed in the gas. It is desirable to impose similar scattering amplitudes over some momentum range, not just equal scattering lengths a. For spin-1/2 fermions, typical values of k can be the Fermi wave vector k_F, the inverse scattering length a^{-1} or the inverse thermal de Broglie wave-length λ_{dB}^{-1}. The typical

value of k depends on the physical situation. The first choice $k \sim a^{-1}$ is appropriate for the case of a condensate of dimers ($a > 0$) since it is the relative momentum of two atoms forming the dimer. The second choice $k \sim k_F$ is appropriate for a degenerate Fermi gas of atoms (not dimers). The third choice $k \sim \lambda_{\mathrm{dB}}^{-1}$ is relevant for a non-degenerate Fermi gas.

2.2 Short range models

For the interaction potential with a short range, the asymptotic expression of s-wave in the non-interacting region takes the form

$$\psi(\mathbf{r}) \overset{r\to\infty}{\to} \frac{\sin(kr+\eta_0)}{kr} \equiv \frac{\sin[k(r-a_s)]}{kr} \overset{k\to 0}{\to} 1 - \frac{a_s}{r}, \tag{2.9}$$

where we have defined the zero energy s-wave scattering length in terms of zero energy phase shift $a_s = -\lim_{k\to 0} \eta_0(k)/k$. Depending on the details of the potential, a_s may have either sign. In the case of positive a_s one can say that by comparison with the noninteracting case the relative wave function is repelled from the origin, whereas with negative a_s the wave function is attracted; in the repulsive case a_s may be visualized as the radius of the hard-sphere potential, which would give rise to the same relative wave function. However, it should be emphasized that in the original problem $\psi(\mathbf{r})$ does not vanish for $r < a_s$.

Even though a_s has the same dimension as the range of the potential r_c, namely, the dimension of length, a_s and r_c can differ by orders of magnitude and have different physical meanings. We say r_c characterizes the range of the potential while a_s characterizes the strength of the "effective" interaction in the sense of scattering. For a repulsive potential, $a_s > 0$ and is roughly of order of r_c, as illustrated by the hard sphere problem. However, for an attractive potential that may support bound states, it is possible for the magnitude of the scattering length to be far greater than the range of the potential. Furthermore, if we increase the attraction, the scattering length can change sign [1].

2.2.1 Examples

Before describing the general behavior of the zero energy ($k \to 0$) s-wave ($l = 0$) scattering length related to the s-wave bound states occurring in short-ranged potentials, we start with several examples of typical short range two-body interactions. The zero-range limit of short-range models will be discussed in the next section.

Hard sphere

$$\begin{aligned} V(\mathbf{r}) &= 0, \quad r > a, \\ &= \infty, \quad r \leq a. \end{aligned}$$

This is a purely repulsive potential. In this case, the s-wave scattering length equals to the range of the potential and has a simple geometric meaning, namely, the radius of the hard sphere

$$a_s = a = r_c. \tag{2.10}$$

Spherical square potential barrier [2]

$$\begin{aligned} V(\mathbf{r}) &= 0, \quad r > a, \\ &= V_0, \quad r \leq a. \end{aligned}$$

This is a repulsive potential and the scattering property is similar to that of a hard sphere. In this sense, purely repulsive potential is not so interesting for scattering. The s-wave is given by

$$a_s(k) = a - \frac{1}{k} \cot^{-1}\left[\frac{\kappa}{k} \coth(\kappa a)\right], \tag{2.11}$$

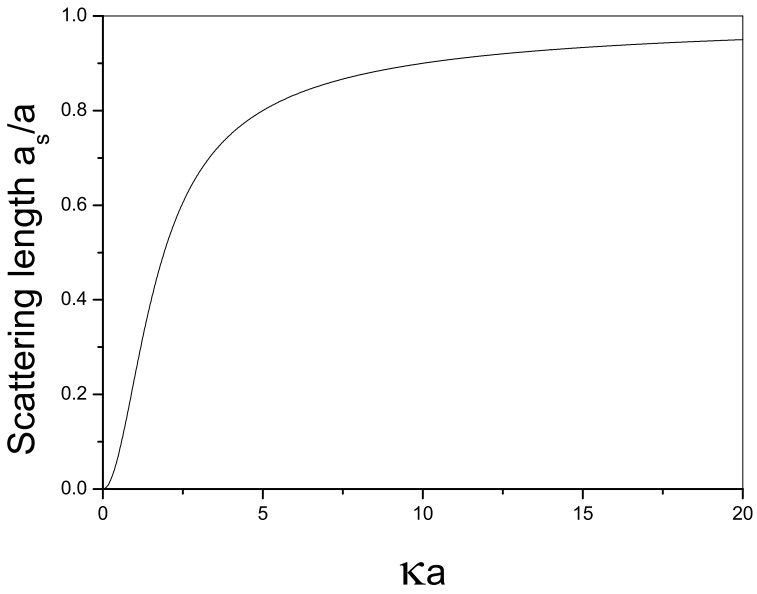

Figure 2.1: Spherical potential barrier.

where $\kappa = \sqrt{\frac{2\mu V_0}{\hbar^2}}$. In low energy limit $k \to 0$, we have

$$a_s = a - \frac{\tanh(\kappa a)}{\kappa}. \tag{2.12}$$

Firstly, in free limit $V_0 \to 0$, we have

$$\frac{\tanh(\kappa a)}{\kappa} \to a, \tag{2.13}$$

thus the scattering length vanishes as expected. We plot the following function in Fig.(2.1)

$$\frac{a_s}{a} = 1 - \frac{\tanh(\kappa a)}{(\kappa a)}. \tag{2.14}$$

As the potential barrier becomes infinitely high, the result agrees with a hard sphere.

Spherical square potential well [2]

$$\begin{aligned} V(\mathbf{r}) &= 0, \quad r > a, \\ &= -V_0, \quad r \leq a. \end{aligned}$$

This is an attractive potential. The s-wave scattering length is given by

$$a_s(k) = a - \frac{1}{k}\cot^{-1}\left[\frac{\kappa}{k}\cot(\kappa a)\right], \tag{2.15}$$

where $\kappa = \sqrt{\frac{2\mu V_0}{\hbar^2}}$. In low energy limit $k \to 0$, we have

$$a_s = a - \frac{\tan(\kappa a)}{\kappa}. \tag{2.16}$$

In the non-interacting limit $V_0 \to 0$, the scattering length vanishes as expected. We plot the following function

$$\frac{a_s}{a} = 1 - \frac{\tan(\kappa a)}{(\kappa a)}. \tag{2.17}$$

in Fig.(2.2) to illustrate the general behavior of low energy s-wave scattering length as a function of the two-body interaction potential. Magnitude divergences and sign changes are observed as the potential well deepens. This is due to the formation of a series of bound states. We consider the emergence of a bound state quantitatively. For $a_s \to +\infty$, the form of the radial wave function $\chi = r\psi = r - a_s$ is approximately e^{-kr} with vanishing k. Note that e^{-kr} with $k \simeq 0$ is the bound state wave function for $r > a$, which is barely bounded with energy E infinitesimally negative. The wave function inside the interacting region ($r < a$) for $E = 0^+$(zero energy scattering state) and $E = 0^-$(bound state with zero binding energy) are essentially the same because

$$\sqrt{\frac{2\mu(0^+ + V_0)}{\hbar^2}} = \sqrt{\frac{2\mu(0^- + V_0)}{\hbar^2}}. \tag{2.18}$$

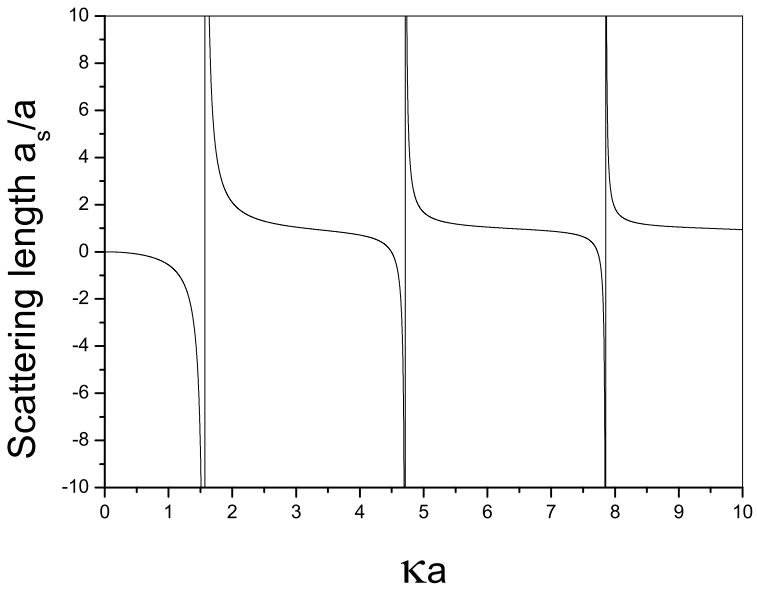

Figure 2.2: Spherical potential well.

Because the wave functions inside the interacting region ($r < a$) are essentially the same for the two situations, we equate the logarithmic derivative of the barely bound state wave function with that of the zero energy scattering solution

$$-\frac{ke^{-kr}}{e^{-kr}}\Big|_{r=a} = \frac{1}{r-a_s}\Big|_{r=a}. \tag{2.19}$$

If the interaction potential is short-ranged, i.e. $a \ll a_s$, we have

$$k = \frac{1}{a_s}, \tag{2.20}$$

thus $a_s \to +\infty$ when a bound state just emerges. The binding energy reads

$$\epsilon \cong -\frac{\hbar^2}{2\mu a_s^2}. \tag{2.21}$$

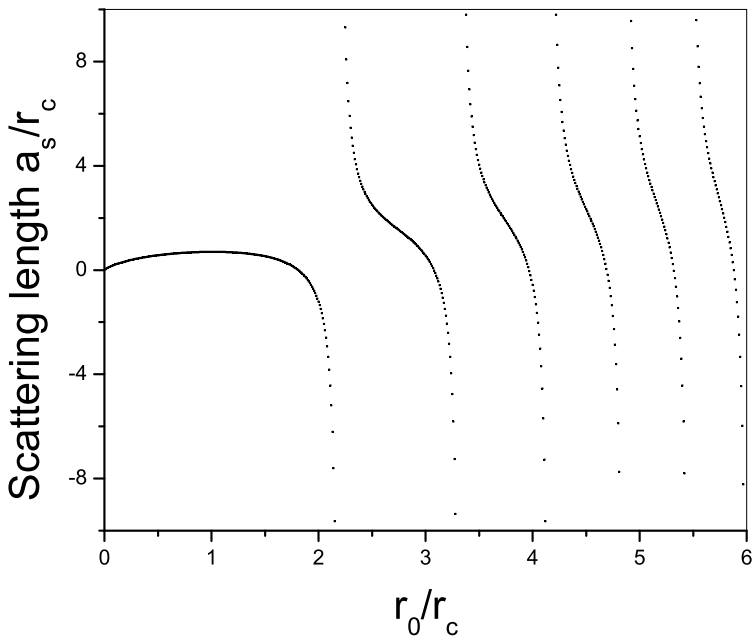

Figure 2.3: van der Waals attraction.

van der Waals attraction with a core [3]

$$\begin{aligned} V(\mathbf{r}) &= -\frac{\alpha}{r^6}, \quad r > r_c, \\ &= \infty, \quad r \leq r_c. \end{aligned}$$

where now r_c characterizes the interaction range and α characterizes the strength. Define the length scale which characterizes the strength $r_0 = \sqrt[4]{\frac{2\mu\alpha}{\hbar^2}}$, the zero energy s-wave scattering length is

$$\frac{a_s}{r_c} = 0.67 \times \left(\frac{r_0}{r_c}\right) \frac{J_{-1/4}\left(r_0^2/2r_c^2\right)}{J_{+1/4}\left(r_0^2/2r_c^2\right)}. \tag{2.22}$$

We plot the scattering length a_s in units of core radius r_c as a function of the potential strength r_0/r_c in Fig.(2.3). This example has almost the same feature as the spherical square potential well, except that as the potential is gradually turned on, the scattering length first becomes positive for a little bit, and then becomes increasingly negative. This illustrates the sentence in Leggett's review [4]: "a_s will initially (or at any rate after a little)

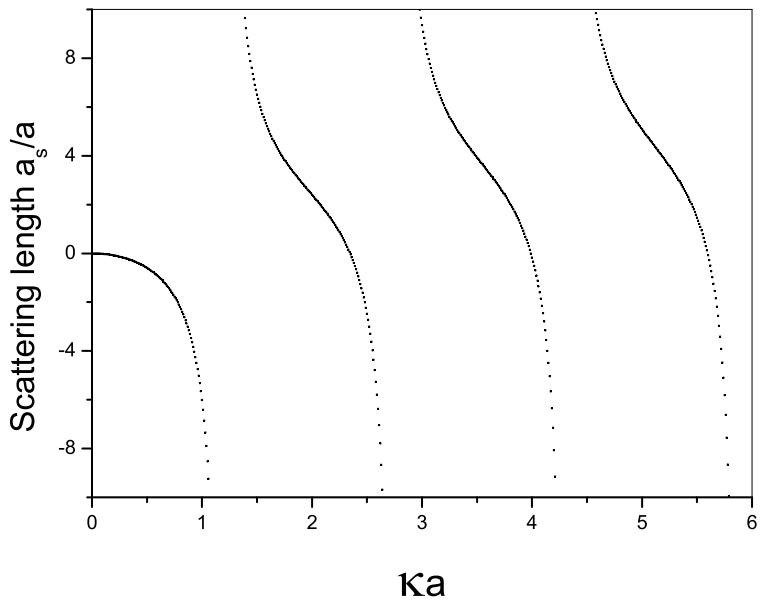

Figure 2.4: Exponential decay attraction.

take increasingly negative values." For a plot of the functional dependence of the scattering length in units of r_0 as a function of the core radius r_c/r_0, see Pethick and Smith [3].

Exponential decay potential [2]

$$V(\mathbf{r}) = -V_0 \exp\left(-\frac{r}{a}\right). \tag{2.23}$$

The asymptotic solution of the scattering wave function at large distance gives

$$\frac{a_s}{a} = 2\log(\gamma\kappa a) - \frac{\pi N_0(2\kappa a)}{J_0(2\kappa a)}, \tag{2.24}$$

where $\kappa = \sqrt{\frac{2\mu V_0}{\hbar^2}}$ and $\gamma = 1.781072381$ is the exponential of Euler's constant. We plot the scattering length in units of the range of the potential in Fig(2.4).

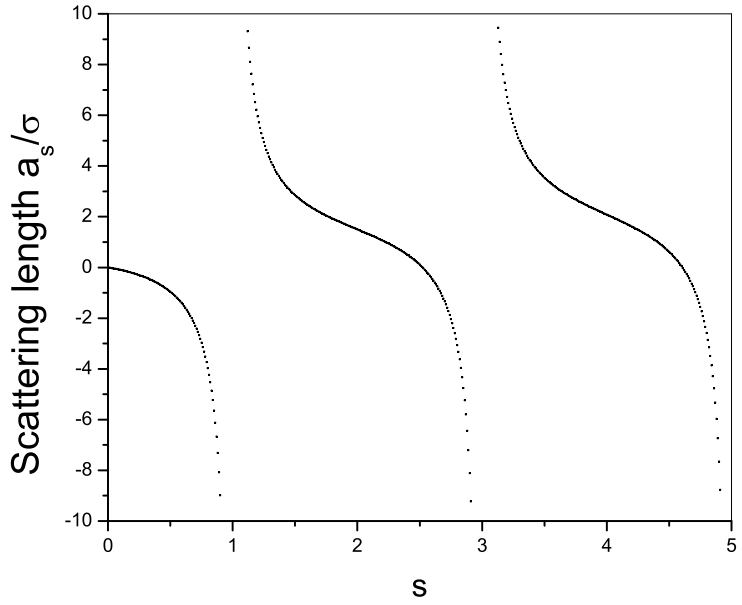

Figure 2.5: Attractive Pöshcl-Teller potential.

Pöschl-Teller potential

$$V(\mathbf{r}) = -\frac{V_0}{\sigma^2 \cosh^2\left(\frac{r}{\sigma}\right)}. \tag{2.25}$$

This $\cosh^{-2}$ potential is particularly useful in quantum Monte Carlo simulations[5, 6]. The asymptotic solution of the scattering wave function at large distance gives

$$\frac{a_s}{\sigma} = \gamma + \psi(s+1) - \frac{\pi}{2}\tan\left(\frac{s\pi}{2}\right), \tag{2.26}$$

where $\gamma = 0.577215665$ is Euler's constant, $s(s+1) = 2\mu V_0/\hbar^2$ and ψ is the logarithmic derivative of the Γ-function. The zero energy s-wave solution is exactly solvable for $V_0 = \hbar^2/\mu$, at which $a_s = \infty$

$$\psi(\mathbf{r}) \propto \frac{\tanh(\lambda r)}{r} \sim \frac{1}{r}. \tag{2.27}$$

We plot the scattering length in units of σ in Fig(2.5).

Separable potential: contact potential on grid

A time-independent separable potential is defined as $\hat{V} = \lambda |S\rangle \langle S|$. This is in general a non-local interaction, where λ is the coupling constant. The Schrödinger equation with a separable potential reads

$$(E - \hat{H}_0)|\psi\rangle = \lambda |S\rangle \langle S|\psi\rangle , \tag{2.28}$$

where $\hat{H}_0 = \mathbf{p}^2/2m$ is the kinetic energy operator. The algebraic equation

$$\langle S|(E - \hat{H}_0)^{-1}|S\rangle = \lambda^{-1} \tag{2.29}$$

determines the bound state solution. It might happen that Eq.(2.29) is not satisfied for any real E which means that a separable potential does not support any bound state. For the scattering problem, we introduce the kinetic energy $E_{\mathbf{k}} = \mathbf{k}^2/2$ of a particle with the momentum $\mathbf{k}$ and rewrite Eq.(2.28) in Lippmann-Schwinger form

$$\left|\psi^+_{\mathbf{k}}\right\rangle = |\mathbf{k}\rangle + \frac{\hat{G}^+_0 (E_{\mathbf{k}}) |S\rangle \langle S|\mathbf{k}\rangle}{\lambda^{-1} - \langle S| \hat{G}^+_0 (E_{\mathbf{k}}) |S\rangle}, \tag{2.30}$$

where $\hat{G}^+_0 (E) = (E + i\epsilon - \hat{H}_0)^{-1}$ corresponds to the incoming and outgoing spherical waves for large distances from the potential center. To perform an analytic calculation we take an explicit form of the separable potential,

$$\hat{V} = -\frac{U}{\Delta^3}|\mathbf{0}\rangle\langle\mathbf{0}| \Rightarrow V(\mathbf{r}) = -\frac{U}{\Delta^3}\delta_{\mathbf{r},\mathbf{0}}. \tag{2.31}$$

This is a contact interaction on grid and Δ is the grid spacing. The zero-energy s-wave scattering length

$$\frac{m}{4\pi\hbar^2 a_s} = \frac{1}{U_\infty} - \frac{1}{U}, \tag{2.32}$$

where the unitarity point $U = U_\infty$ occurs at $a_s \to \infty$,

$$\frac{1}{U_\infty} = \frac{1}{V}\sum_{\mathbf{k}'} \frac{1}{\epsilon_{\mathbf{k}'}} = \int_D \frac{d^3\mathbf{k}'}{(2\pi)^3}\frac{1}{\epsilon_{\mathbf{k}'}} = \gamma\frac{m}{\hbar^2\Delta}. \tag{2.33}$$

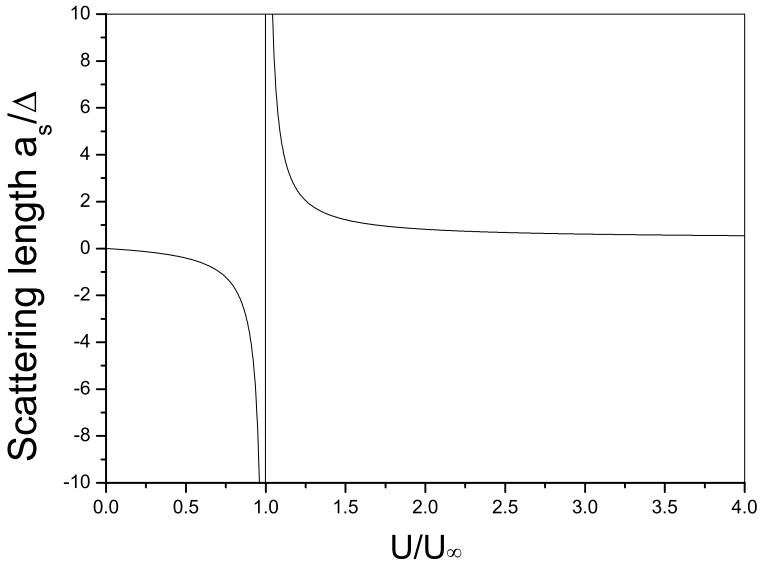

Figure 2.6: Contact interaction on grid.

If we choose the parabolic dispersion relation $\epsilon_{\mathbf{k}} = \hbar^2 k^2/2\mu = \hbar^2 k^2/m$, $\gamma \approx 0.1944$. For a nearest neighbor hopping model, we have the tight-binding dispersion relation and $\gamma \approx 0.2527$; for a long range hopping model including up to the next nearest neighbors, $\gamma \approx 0.2190$. We plot the scattering length in units of the grid spacing Δ in Fig(2.6). The contact potential on grid differs from the short-ranged potentials in one important aspect that there exists a single bound state and hence one unitarity point $a_s = \infty$.

Relation to Hubbard parameters

In nearest neighbor hopping Hubbard model, we have the kinetic energy term $-t\sum_{\langle i,j\rangle}(c_i^\dagger c_j + c_j^\dagger c_i)$ which possesses the eigenvalues $\epsilon_{\mathbf{k}} = -2t\left(\cos k_x\Delta + \cos k_y\Delta + \cos k_z\Delta\right)$. We identify the hopping coefficent

$$t = \frac{\hbar^2}{m\Delta^2}, \tag{2.34}$$

and the scattering length a_s in terms of Hubbard parameters is given by

$$\frac{1}{a_s} = 4\pi t\left(\frac{1}{u_\infty} - \frac{1}{u}\right). \tag{2.35}$$

Here a_s is in units of the grid spacing Δ.

2.2.2 Summary

The general behavior of the scattering length is related to the s-wave bound states occurring in the potential. If we imagine starting from the noninteracting state ($a_s \equiv 0$) and gradually increasing the strength of the potential (whose shape is taken to be typical of a real atomic one), then a_s will initially (or at any rate after a little) take increasingly negative values. As the point at which the potential is just enough to sustain a bound state is approached, a_s will approach $-\infty$, and when the state is just bound, will take a large positive value (which approaches $+\infty$ as the potential is reduced again to the critical value). In this region ($a_s \gg r_c$) the asymptotic form of the bound-state wave function is $r^{-1}\exp(-r/a_s)$ and its energy is $-\hbar^2/2ma_s^2$; (the form of the zero-energy scattering state may be viewed as a consequence of the need to make it orthogonal to the bound state). This general behavior is expected near the points where further bound states appear in the well [4].

In summary, zero energy s-wave scattering length is a characterization of the strength of the "effective" interaction, but not the real potential. Phase shift observations in scattering experiments are made at large distance from the scatterers. We say if the scattered wave is pushed in, this is an attractive interaction; or pulled out, we say this is a repulsive interaction. However, while a repulsive potential can only pull out a scattered wave, an attractive potential can either push it in or pull it out, depending on the formation of bound states. Thus from the scattering experiments, we can only tell the sign of the effective interaction, which is indeed characterized by the sign of the scattering length.

2.3 Zero range model

Based on the examples of short range potentials discussed in the previous section, we introduce the zero-range δ-function pseudopotential and briefly recapitulate the derivation. The Schrödinger equation for the relative motion of two identical particles of mass m which interact via a finite-range potential $V(|\mathbf{r}|)$,

$$\left[-\nabla^2 + V(r)\right]\psi(\mathbf{r}) = E\psi(\mathbf{r})\,. \tag{2.36}$$

Here we choose the units $m = \hbar = 1$. Write $E = k^2$ and denote the finite range of the interaction potential as r_c, and one encounters the Helmholtz equation in the outer range,

$$\left(\nabla^2 + k^2\right)\psi\left(\mathbf{r}\right) = 0, \quad r > r_c. \tag{2.37}$$

This equation is solved by spherical Bessel functions and harmonics

$$\psi\left(\mathbf{r}\right) = \sum_{l=0}^{\infty}\sum_{m=-l}^{l} A_{lm}\left[j_l\left(kr\right) - \tan\left(\eta_l\right) n_l\left(kr\right)\right] Y_{lm}\left(\theta,\phi\right), \tag{2.38}$$

where $\eta_l = \eta_l(k)$ is called the phase shift of the lth partial wave. Restricting oneself to low energies $k \to 0$, so that only s-wave matters, this simplifies to

$$\psi\left(\mathbf{r}\right) = \frac{A_{00}}{\sqrt{4\pi}}\left[\frac{\sin(kr)}{kr} + \tan\left(\eta_0\right)\frac{\cos(kr)}{kr}\right] \propto \frac{\sin\left(kr+\eta_0\right)}{kr}, \quad r \to \infty. \tag{2.39}$$

The decisive step of the pseudopotential method is to extend the validity range of this outer wave function to all r, even though the actual wave function is affected by the potential, and therefore differs from the function for $r < r_c$. When extending the outer function to $r < r_c$, the term proportional to $\tan(\eta_0)$, that is, the term which actually "feels" the potential, becomes singular. It is this singularity which gives rise to the pseudopotential. Since the outer function solves the Helmholtz equation for all $r > 0$, and $r = 0$ is dealt with by the relation $\nabla^2\left(1/r\right) = -4\pi\delta\left(\mathbf{r}\right)$, the extended wave function obeys the operator equation

$$\left(\nabla^2 + k^2\right)\psi\left(\mathbf{r}\right) = -4\pi\frac{A_{00}}{\sqrt{4\pi}}\frac{\tan\left(\eta_0\right)}{k}\delta\left(\mathbf{r}\right). \tag{2.40}$$

By observing that

$$\frac{A_{00}}{\sqrt{4\pi}} = \frac{\partial}{\partial r}\left[r\psi\left(\mathbf{r}\right)\right]\Big|_{r\to 0}, \tag{2.41}$$

we reintroduce the wave function into the differential equation

$$\left(\nabla^2 + k^2\right)\psi\left(\mathbf{r}\right) = -4\pi\frac{\tan\left(\eta_0\right)}{k}\delta\left(\mathbf{r}\right)\frac{\partial}{\partial r}\left[r\psi\left(\mathbf{r}\right)\right]. \tag{2.42}$$

This equation now holds for all r. In effect, the actual interaction potential has thus been replaced, for s-wave scattering, by the pseudopotential operator

$$U(\mathbf{r}) = -\frac{4\pi \tan(\eta_0)}{k}\delta(\mathbf{r})\frac{\partial}{\partial r}r. \tag{2.43}$$

If we insert back the particle mass and Planck constant, we have

$$U(\mathbf{r}) = -\frac{4\pi\hbar^2}{m}\frac{\tan(\eta_0)}{k}\delta(\mathbf{r})\frac{\partial}{\partial r}r = -\frac{2\pi\hbar^2}{\mu}\frac{\tan(\eta_0)}{k}\delta(\mathbf{r})\frac{\partial}{\partial r}r. \tag{2.44}$$

Notice that usually, it is the individual particle mass m instead of the reduced mass μ that is set to unity. In the special case of a hard sphere interaction of radius a, one has $\eta_0 = -ka$ and then the commonly quoted zero range interaction

$$U(\mathbf{r}) = \frac{4\pi\hbar^2 a}{m}\delta(\mathbf{r})\frac{\partial}{\partial r}r = \frac{2\pi\hbar^2 a}{\mu}\delta(\mathbf{r})\frac{\partial}{\partial r}r. \tag{2.45}$$

By substitution we can verify the form of the two-body bound state wave function and the binding energy

$$\epsilon_0 = -\frac{\hbar^2}{ma^2}, \tag{2.46}$$

$$\psi_0(r) = \frac{1}{\sqrt{2\pi a}}\frac{e^{-\frac{r}{a}}}{r}. \tag{2.47}$$

Note that for $a > 0$, the potential is repulsive as long as scattering properties are concerned, but the regularization of the δ-functions gives rise to a single bound state as if an attracitve interaction were at work. The corresponding energy $1/a^2$ tends to ∞ as $a \to 0^+$ and the bound state wave function has a vanishing overlap with any (a-independent) square-integrable wave function, i.e. this limit exhibits an anomaly that the binding energy grows without bound and the scattering cross section vanishes. For the reference of a similar problem but in a trap, see [7]. For attractive case $a < 0$, no anomaly occurs.

On the other hand, the exact outgoing scattering states can also be constructed explicitly

$$\psi_{\mathbf{k}}^{(+)}(\mathbf{r}) = e^{i\mathbf{k}\cdot\mathbf{r}} + f_{\mathbf{k}}\frac{e^{ikr}}{r}, \tag{2.48}$$

where

$$f_{\mathbf{k}} = -\frac{1}{a^{-1} + ik}. \tag{2.49}$$

This result can be verified by substitution into Schrödinger equation in the same way as the bound state

$$\hat{H}\psi_{\mathbf{k}}^{(+)} = k^2\psi_{\mathbf{k}}^{(+)}. \tag{2.50}$$

The incoming scattered wave $\psi_{\mathbf{k}}^{(-)}$ can be obtained by a complex conjugation of the outgoing wave. Together with the single bound state, the scattered waves form a complete basis set of the given Hamiltonian. One of the possible reasons why this pseudopotential is an important result in the physics of ultracold alkali gases is that the zero energy s-wave scattering length is particularly simple in this form,

$$a_s = a. \tag{2.51}$$

Namely, the oefficient in front of the δ-function is identically the scattering length. Historically, δ-function pseudopotential was introduced to facilitate the perturbative calculation of many body problem with hard sphere interactions [8], but has a far wider validity and applications. The regularized δ-function potential actually models attractive potential which would give rise to positive scattering length by forming bound states. We may say that the regularized δ-function potential is a simple parametrization of the short-ranged potentials in terms of the scattering length.

2.4 Bethe-Peierls boundary condition

There are basically two approaches to model the interaction between ultra-cold atoms in a unitary gas or more generally, for the BEC-BCS crossover.

In the first approach, see Sect(2.2) one takes a model interaction with a finite range r_c

and a fixed (e.g. infinite) scattering length a. This model may be in continuous space or on a lattice, with one or several channels. Then one tries to calculate the eigenenergies, the thermodynamic properties from the thermal density operator $e^{-\beta\hat{H}}$, etc, and the zero range limit $r_c \to 0$ should be taken the end of the calculation. Typically, this approach is followed in numerical many-body methods, such as the approximate fixed node Monte Carlo method or unbiased Quantum Monte Carlo methods [5, 6]. A non-trivial question however is whether each eigenstate of the model is universal in the zero range limit, that is if the eigenenergy and the corresponding wavefunction converge for $r_c \to 0$.

In the second approach, see Sect(2.3), one directly considers the zero range limit, and one replaces the interaction by the so-called *Wigner-Bethe-Peierls* contact conditions on the N-body wavefunction. This constitutes what we shall call the zero-range model. The advantage is that only the scattering length appears in the problem, without unnecessary details on the interaction, which simplifies the problem and allows to obtain analytical results. For example the scale invariance of the unitary gas becomes clear. A non-trivial question however is to know whether the zero-range model leads to a self-adjoint Hamiltonian, with a spectrum then necessarily bounded from below for the unitary gas, without having to add extra boundary conditions. For equal mass two-component Fermions, it is hoped in the physics literature that the zero-range model is self-adjoint for an arbitrary number of particles N.

In the Wigner-Bethe-Peierls model, that we also call zero-range model, the Hamiltonian for a system of particles interacting with δ-function pseudopotentials is simply represented by the same partial differential operator as for the ideal gas case:

$$\hat{H} = \sum_{i=1}^{N} \left[-\frac{\hbar^2}{2m} \nabla^2_{\mathbf{r}_i} + U(\mathbf{r}_i) \right], \tag{2.52}$$

where U is the external trapping potential supposed for simplicity to be spin-independent. As is however well emphasized in the mathematics of operators on Hilbert spaces, an operator is defined not only by a partial differential operator, but also by the choice of its so-called domain $\mathcal{D}(\hat{H})$. Here the domain does not coincide with the ideal gas one. It includes the following Wigner-Bethe-Peierls contact conditions: for any pair of particles i, j,when

$r_{ij} = |\mathbf{r}_i - \mathbf{r}_j|$ for a fixed position of their centroid $\mathbf{R}_{ij} = (\mathbf{r}_i + \mathbf{r}_j)/2$ and all the other particles, there exists a function A_{ij} such that

$$\Psi(\mathbf{r}_1, \cdots, \mathbf{r}_i, \cdots, \mathbf{r}_j, \cdots, \mathbf{r}_N) \to A_{ij}(\mathbf{R}_{ij}; \mathbf{r}_{k\neq i,j}) \left(\frac{1}{r_{ij}} - \frac{1}{a} \right) + O(r_{ij}). \tag{2.53}$$

These conditions are imposed for all values of $\mathbf{R}_{ij}$ different from the positions of the other particles $\mathbf{r}_k$, k different from i and j. If the Fermionic particles i and j are in the same spin state, the fermionic symmetry imposes $\Psi(\cdots, r_i = r_j, \cdots) = 0$ and one has simply $A_{ij} = 0$. For i and j in different spin states, the unknown functions A_{ij} have to be determined from Schrödinger equation, e.g. together with the energy E from the eigenvalue problem $\hat{H}\Psi = E\Psi$. Note that in Eq(2.53) we have excluded the configurations where two particle positions coincide. Since $\nabla^2_{\mathbf{r}_i} r_{ij}^{-1} = -4\pi\delta(\mathbf{r}_i - \mathbf{r}_j)$, including these values would require a calculation with distributions rather than with functions, with regularized delta interaction pseudo-potential, which is a compact and sometimes useful reformulation of the Wigner-Bethe-Peierls contact conditions.

An application: two-particle problem in a periodic box

As an application of the Wigner-Bethe-Peierls boundary condition, we construct the explicity form of the two-body bound-state solution in a periodic box

$$\psi_0^{\text{box}}(\mathbf{r}) \;\; = \;\; \sum_{\mathbf{L}} \frac{e^{-\frac{|\mathbf{r}+\mathbf{L}|}{a'}}}{|\mathbf{r}+\mathbf{L}|},$$

where $\mathbf{L}$ denotes the integer multiples of lattice vectors corresponding to the lengths of box. Notice that the above expression is a periodic image summation of solutions in infinite space; however, each term in the summation has a modified parameter a'. To fix this parameter, the Bethe-Peierls boundary condition is invoked:

$$\psi_0^{\text{box}}(\mathbf{r}) \;\; \overset{r\to 0}{\to} \;\; \frac{1}{r} - \frac{1}{a'} + \sum_{\mathbf{L}\neq\mathbf{0}} \frac{e^{-\frac{|\mathbf{L}|}{a'}}}{|\mathbf{L}|} = \frac{1}{r} - \frac{1}{a},$$

Thus, the parameter a' is related to the scattering length a

$$\frac{1}{a} = \frac{1}{a'} - \sum_{\mathbf{L}\neq\mathbf{0}} \frac{e^{-\frac{|\mathbf{L}|}{a'}}}{|\mathbf{L}|}. \tag{2.54}$$

If we write $\mathbf{L}/L = n_1\hat{\mathbf{x}} + n_2\hat{\mathbf{y}} + n_3\hat{\mathbf{z}}$, then

$$\frac{1}{a} = \frac{1}{a'} - \sum_{\mathbf{n}\neq\mathbf{0}} \frac{e^{-\frac{|\mathbf{n}|}{a'}}}{|\mathbf{n}|}, \tag{2.55}$$

where a and a' is written in units of L, $|\mathbf{n}| = \sqrt{n_1^2 + n_2^2 + n_3^2}$. The unitarity limit $a \to \infty$ corresponds to a value of a' that satisfies the following transcendental equation

$$\frac{1}{a'} - \sum_{\mathbf{n}\neq\mathbf{0}} \frac{e^{-\frac{|\mathbf{n}|}{a'}}}{|\mathbf{n}|} = 0. \tag{2.56}$$

This construction can be verified by substitution into Schrödinger equation with the regularized δ-function interaction. The results are summarized in Fig(2.7). The left part shows the functional dependence of the effective parameter a' in the wavefunction on the scattering length a. As expected, in the tight-binding limit $a^{-1} \to \infty$, we have

$$\lim_{a\to 0} a'/a = 1. \tag{2.57}$$

The important feature is that in the unitary limit $a^{-1} \to 0$, the parameter a' approaches a non-zero constant $L/a' \approx 1.95$, which in consequence gives rise to a non-zero binding energy in the box. The right part of Fig(2.7) shows the 2-body binding energy as a function of the scattering length a^{-1}. This expression is useful for the construction of two-body orbitals in the many-body wavefunctions in QMC calculations.

2.5 Feshbach resonances: two-channel model

The short range models or the zero-range model are of course dramatic simplifications of the real interaction between two alkali atoms. At large interatomic distances, much larger

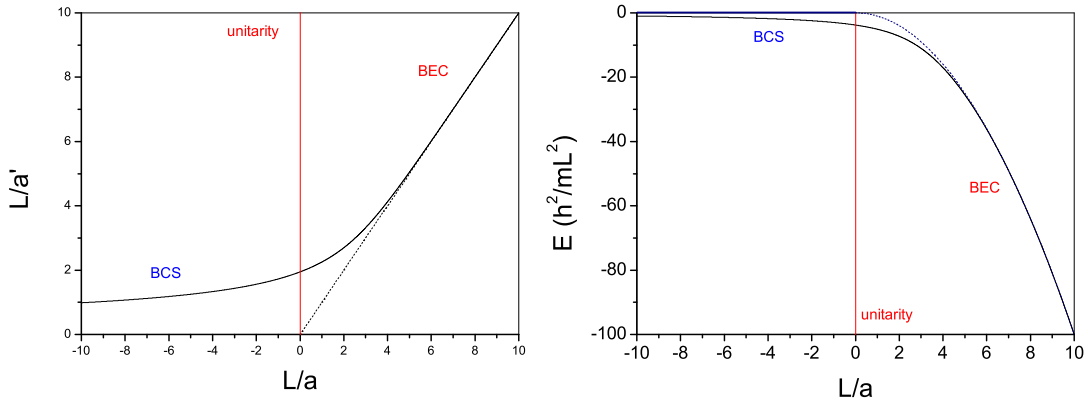

Figure 2.7: Two particles with a regularized δ-function interaction in a periodic box.

than the radius of the electronic orbitals, one may hope to realistically represent this interactionby a function $V(\mathbf{r})$ of the interatomic distance, with a van der Waals attractive tail $V(r) = -C_6/r^6$, a simple formula that actually neglects retardation effects and long-range magnetic dipole-dipole interactions. At short interatomic distances, this simple picture of a scalar interaction potential $V(r)$ has to be abandoned. Following quantum chemistry or molecular physics methods, one has to introduce the various Born-Oppenheimer potential curves obtained from the solution of the electronic eigenvalue problem for fixed atomic nuclei positions. For alkali atoms, restricting to one active electron of spin-1/2 per atom, one immediately gets two ground potential curves, the singlet one corresponding to the total spin $S = 0$, and the triplet one corresponding to the total spin $S = 1$. An external magnetic field B is applied to activate the Feshbach resonance. This magnetic field couples mainly to the total electronic spin and thus induces different Zeeman shifts for the singlet and triplet curves. In reality, the problem is further complicated by the existence of the nuclear spin and the hyperfine coupling, that couples the singlet channel to the triplet channel for nearby atoms, and that induces a hyperfine splitting within the ground electronic state for well separated atoms.

We first take a simplified view depicted in Fig(2.8) the atoms interact via two potential curves, $V_{\text{open}}(r)$ and $V_{\text{closed}}(r)$. At large distances, $V_{\text{open}}(r)$ conventionally tends to zero, whereas $V_{\text{closed}}(r)$ tends to a positive value V_∞, one of the hyperfine energy level spacings

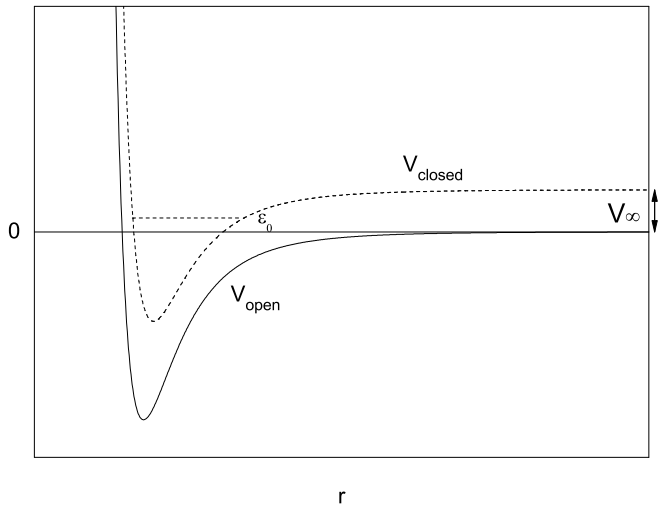

Figure 2.8: A simplified view of a Feshbach resonance.

for a single atom in the applied magnetic field. In the two-body scattering problem, the atoms come from $r = +\infty$ in the internal state corresponding to $V_{\rm open}(r)$, the so-called open channel, with a kinetic energy $E \ll V_\infty$. Due to a coupling between the two channels, the two interacting atoms can have access to the internal state corresponding to the curve $V_{\rm closed}(r)$, but only at short distances; at long distances, the external atomic wavefunction in this so-called closed channel is an evanescent wave that decays exponentially with r since $E < V_\infty$. Assume the closed channel supports a bound state of energy ϵ_0 in the absence of coupling between the channels, called in what follows the *molecular state* or the *closed-channel molecule*. Assume also that, by applying a judicious magnetic field, one sets the energy of this molecular state close to zero, that is to the dissociation limit of the open channel. In this case one may expect that the scattering amplitude of two atoms is strongly affected, by a resonance effect, given the non-zero coupling between the two channels. This is in essence how the Feshbach resonance takes place.

In the following we briefly review the essential steps in the Feshbach theory of resonances to calculate the S-matrix element S_{ji} for the transition from an open channel i to anotehr open channel j in the neighborhodd of a resonance [9]. The total Hilbert space describing the spatial and spin degrees of freedom is subdivided into a closed-channel subspace $\mathcal{Q}$, comprising the closed channels and a complimentary open channel subspace $\mathcal{P}$. Feshbach

resonances occur as a result of transitions from $\mathcal{P}$ to $\mathcal{Q}$ and back to $\mathcal{P}$ during a collision. Introducing operators $\hat{P}$ and $\hat{Q}$, projecting on $\mathcal{P}$ and $\mathcal{Q}$, the total Schrödinger equation of the system is split into two coupled equation

$$(E - \hat{H}_{PP})\Psi_P = \hat{H}_{PQ}\Psi_Q, \tag{2.58}$$

$$(E - \hat{H}_{QQ})\Psi_Q = \hat{H}_{QP}\Psi_Q, \tag{2.59}$$

with $\Psi_P \equiv \hat{P}Psi, \Psi_Q \equiv \hat{Q}\Psi, \hat{H}_{PP} = \hat{P}\hat{H}\hat{P}, \hat{H}_{QQ} = \hat{Q}\hat{H}\hat{Q}$ and $\hat{H}_{PQ} \equiv \hat{P}\hat{H}\hat{Q}$. Equation (2.59) is formally solved by using the Green operator $(E^+ - \hat{H}_{QQ})^{-1}$ with $E^+ = E + i0$:

$$\Psi_Q = \frac{1}{E^+ - \hat{H}_{QQ}}\hat{H}_{QP}\Psi_P. \tag{2.60}$$

Substituting this expression in Eq(2.59) we get

$$(E - \hat{H}_{\text{eff}})\Psi_P = 0, \tag{2.61}$$

where

$$\hat{H}_{\text{eff}} = \hat{H}_{PP} + \hat{H}_{PQ}\frac{1}{E^+ - \hat{H}_{QQ}}\hat{H}_{QP}. \tag{2.62}$$

The second term in this effective Hamiltonian can be interpreted in terms of a temporary transition from $\mathcal{P}$ space to $\mathcal{Q}$ space, propagation in $\mathcal{Q}$ space, and then reemission into $\mathcal{P}$ space. The next step is the spectral decomposition of the Green operator

$$\frac{1}{E^+ - \hat{H}_{QQ}} = \sum_m \frac{|\phi_m\rangle\langle\phi_m|}{E - \epsilon_m} + \int d\epsilon \frac{|\phi(\epsilon)\rangle\langle\phi(\epsilon)|}{E^+ - \epsilon}. \tag{2.63}$$

If the total energy E is close to a discrete bound state energy ϵ_0 we can neglect the remaining terms and Eq(2.61) reduces to

$$(E - \hat{H}_{PP})\Psi_P = \frac{\hat{H}_{PQ}|\phi_B\rangle\langle\phi_B|\hat{H}_{QP}|\Psi_P\rangle}{E - \epsilon_0}, \tag{2.64}$$

with the formal solution

$$|\Psi_P\rangle = |\Psi_i^+\rangle + \frac{1}{E^+ - \hat{H}_{PP}} \frac{\hat{H}_{PQ}|\phi_B\rangle\langle\phi_B|\hat{H}_{QP}|\Psi_P\rangle}{E - \epsilon_0}, \tag{2.65}$$

where $|\Psi_i^+\rangle$ is an eigenstate of $\hat{H}_{PP}$ with an incoming wave in channel i. We can solve for $|\Psi_P\rangle$ by multiplication from the left with $\langle\phi_B|\hat{H}_{QP}$ and find

$$|\Psi_P\rangle = |\Psi_i^+\rangle + \frac{1}{E^+ - \hat{H}_{PP}}\hat{H}_{PQ}|\phi_B\rangle \times \frac{\langle\phi_B|\hat{H}_{QP}|\Psi_i^+\rangle}{E - \epsilon_0 - \langle\phi_B|\hat{H}_{QP}\frac{1}{E^+ - \hat{H}_{PP}}\hat{H}_{PQ}|\phi_B\rangle}. \tag{2.66}$$

Thus the amplitude S_{ji} for the transition to channel j is determined by the asymptotic behavior of Ψ_P

$$S_{ji} = S_{ji}^0 - 2\pi i \frac{\langle\Psi_j^-|\hat{H}_{PQ}|\phi_B\rangle\langle\phi_B|\hat{H}_{QP}|\Psi_i^+\rangle}{E - \epsilon_0 - \langle\phi_B|\hat{H}_{QP}\frac{1}{E^+ - \hat{H}_{PP}}\hat{H}_{PQ}|\phi_B\rangle}. \tag{2.67}$$

We see that apart from the direct term S_{ji}^0 resulting from coupling within $\mathcal{P}$ space alone, the amplitude of an outgoing wave in channel j will include aterm arising from coupling of the incoming wave in channel i to the bound state in $\mathcal{Q}$ space followed by coupling of this state to channel j. If we have only one open channel i we can write teh above expression as

$$S_{ii} = S_{ii}^0 \left(1 - \frac{i\Gamma}{E - \epsilon_0 - \Delta + i\frac{\Gamma}{2}}\right), \tag{2.68}$$

where $\Gamma = 2\pi|\langle\phi_B|\hat{H}_{PQ}|\Psi_i^+\rangle|^2$ represents teh width and Δ the so-called resonance shift. Or in the language of scattering length

$$\frac{4\pi\hbar^2}{m}a = \frac{4\pi\hbar^2}{m}a_{\rm nr} - \frac{|\langle\phi_B|\hat{H}_{PQ}|\Psi_i^+\rangle|^2}{E - \epsilon_0}. \tag{2.69}$$

In the case of ultra-cold collisions of ground state alkali atoms, it is the combination of single-atom hyperfine and Zeeman interactions that determines the threshold of the various channels at the specific magnetic field strength and thus determines the open and closed channel subspaces. Atomic interactions may be tuned by exploiting the fact that the energies of internal states depend on external parameters. We imagine that the energy demoninator

in Eq(2.69) vanishes for a particular value of the magnetic field, $B = b_0$. Expanding the energy denominator about this value of the magnetic field, we find

$$E - \epsilon_0 \approx (\mu_0 - \mu_\alpha - \mu_\beta)(B - B_0), \tag{2.70}$$

where

$$\mu_\alpha = -\frac{\partial \epsilon_\alpha}{\partial B}, \quad \mu_\beta = -\frac{\partial \epsilon_\beta}{\partial B} \tag{2.71}$$

are the magnetic moments of the two atoms in the open channel, and

$$\mu_0 = -\frac{\partial \epsilon_0}{\partial B} \tag{2.72}$$

is the magnetic moment of the molecular bound state in the closed channel. The scattering length is thus given by

$$a = a_{\rm nr}\left(1 + \frac{\Delta B}{B - B_0}\right), \tag{2.73}$$

where the width parameter ΔB is given by

$$\Delta B = \frac{m}{4\pi\hbar^2 a_{\rm nr}} \frac{|\langle \phi_B | \hat{H}_{PQ} | \Psi_i^+ \rangle|^2}{\mu_0 - \mu_\alpha - \mu_\beta}. \tag{2.74}$$

Equation (2.73) shows that in this approximation the scattering length diverges to $\pm\infty$ as B approaches B_0. Because of the dependence $1/(B - B_0)$, large changes in the scattering length can be produced by small changes in the external field. It is especially significant that the sign of the interaction can be changed by a small change in the field.

2.6 Scattering length approximation

As discussed in the previous sections, the shape or potential resonances are accompanied by the formation of lower-lying bound states and Feshbach resonances take place by the coupling between an open channel and a closed channel molecular state. The two-body *scattering length approximation* (SLA) neglects the low-lying molecular states. Recall that

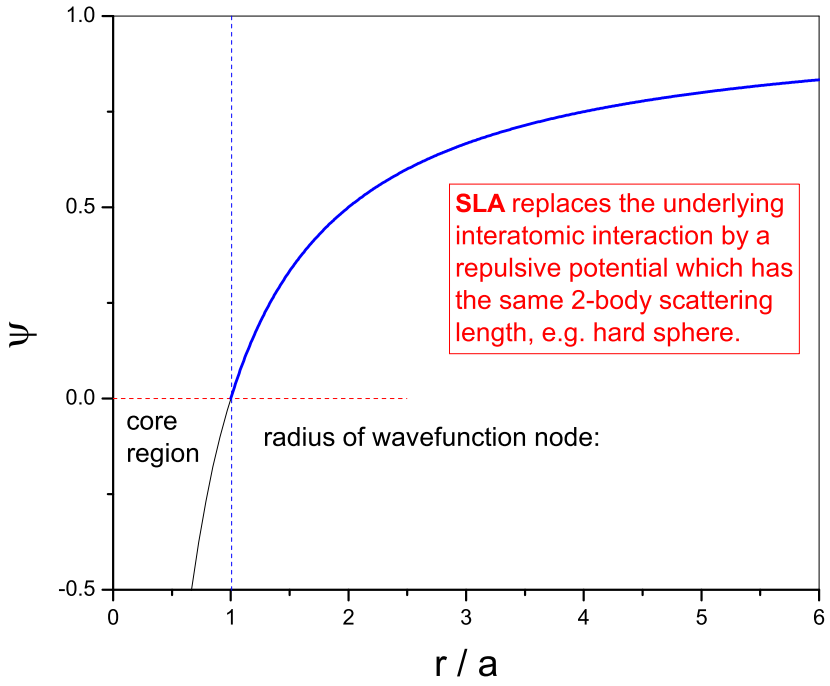

Figure 2.9: Scattering length approximation by replacing the attractive contact interaction with a zero boundary condition

the zero-energy s-wave scattering length a is defined by the long distance form of the outgoing scattering wave

$$\psi\left(r\rightarrow\infty\right)\propto\frac{\sin\left[k(r-a)\right]}{kr}\overset{k\rightarrow0}{\longrightarrow}1-\frac{a}{r}. \tag{2.75}$$

For a contact (zero range) potential, a is the radius of the first wavefunction node: $\psi\left(r=a\right)=0$. The SLA replaces the underlying atomic interaction by a purely repulsive potential which has the same two-body scattering length. This is illustrated in Fig(2.9).

This is analogous to the idea of pseudo-potentials in electronic structure. A pseudopotential can be generated in an atomic calculation to replace the strong Coulomb potential of the nucleus and the effects of the tightly bound core electrons by an effective ionic potential acting on the valence electrons and then used to compute properties of valence electrons in molecules or solids, since the core states remain almost unchanged. The approach is widely used in electronic structure calculations. However, it leads to an inaccuate model if a pseudopotential is used for systems compressed to high density and the electron cores start to overlap.

Many experiments in cold atomic systems are performed near Feshbach resonance where the scattering length is comparable to interatomic separation. In this situation, the lower-lying molecular bound states giving rise to resonance can overlap, causing the scattering states to distort in order to remain orthogonal to the bound states.

References

[1] J. J. Sakurai and Jim J. Napolitano. *Modern Quantum Mechanics*. Addison Wesley, second edition, 2010.

[2] L. D. Landau and E. M. Lifshitz. *Quantum Mechanics, Non-relativisitic Theory*. Butterworth-Heinemann, third edition, 1981.

[3] C. J. Pethick and H. Smith. *Bose-Einstein Condensation in Dilute Gases*. Cambridge University Press, first edition, 2002.

[4] Anthony J. Leggett. Bose-einstein condensation in the alkali gases: Some fundamental concepts. *Rev. Mod. Phys.*, 73:307–356, Apr 2001.

[5] S. Y. Chang, V. R. Pandharipande, J. Carlson, and K. E. Schmidt. Quantum monte carlo studies of superfluid fermi gases. *Phys. Rev. A*, 70:043602, Oct 2004.

[6] J. Carlson, S.-Y. Chang, V. R. Pandharipande, and K. E. Schmidt. Superfluid fermi gases with large scattering length. *Phys. Rev. Lett.*, 91:050401, Jul 2003.

[7] Thomas Busch, Berthold-Georg Englert, Kazimierz Rzazewski, and Martin Wilkens. Two cold atoms in a harmonic trap. *Foundation of Physics*, 28:549–559, Jan 1998.

[8] Kerson Huang and C. N. Yang. Quantum-mechanical many-body problem with hard-sphere interaction. *Phys. Rev.*, 105:767–775, Feb 1957.

[9] A. J. Moerdijk, B. J. Verhaar, and A. Axelsson. Resonances in ultracold collisions of ^{6}Li, ^{7}Li, and ^{23}Na. *Phys. Rev. A*, 51:4852–4861, Jun 1995.

Chapter 3

Bosons in Disordered Optical Lattice

3.1 White *et al.* experiment

Understanding the properties of disordered materials has a fundamental significance in condensed matter physics. Various kinds of disorder exist in real materials, but their disorder is difficult to characterize and control experimentally. The optical lattice techniques [1] developed in recent years have enabled the construction of a nearly perfectly controlled disordered potential and the measurement of properties of strongly correlated atoms in that potential provides an opportunity to compare quantitatively experimental results with parameter-free theoretical calculations.

The White *et al.* experiment consists of ^{87}Rb atoms trapped in a background cubic lattice potential created by red lasers with wave vector $k = \frac{\pi}{a}$. The periodic background potential is:

$$U_L(\mathbf{r}) = -S_L \times \sum_{i=1}^{3} \cos\left(\frac{2\pi \mathbf{n}_i \cdot \mathbf{r}}{a}\right), \tag{3.1}$$

where $\mathbf{n}_i$ are three mutually orthogonal unit vectors. The lattice spacing $a = 406$nm. A disordered speckle field $U_D(\mathbf{r})$ is produced by a laser beam with phases randomized by a diffuser. There is no closed form for the speckle distribution, however, the method of constructing the disordered potential to match the White *et al.* experiment [1] is approximated by

$$U_D(\mathbf{r}) \propto SD \times \left| \mathrm{FT}\left[\Theta\left(d^2 - q_x^2 - q_y^2\right) \exp\left\{ -\frac{q_x^2 + q_y^2}{w^2} + i\gamma z\left(q_x^2 + q_y^2\right) + i\phi\left(q_x, q_y\right) \right\} \right] \right|^2, \tag{3.2}$$

where Θ is an aperture disc with radius $d = 0.66k$ and $w = 2.16k$ is the waist of the Gaussian

beam, $\gamma = 0.1a$ characterizes its radius of curvature, $\phi(q_x, q_y)$ is an uncorrelated random phase uniformly distributed in $[0, 2\pi)$ and the Fourier transform (FT) is performed in the two dimensional (q_x, q_y) space. We normalize the field so that $\langle U_D(\mathbf{r})\rangle = S_D$. If one wishes to make the speckles smaller or larger, one can change the aperture diameter d. Detailed derivations can be found in Goodman [2]. The spatial auto-correlation $\Gamma = \langle U_D(\mathbf{r})U_D(\mathbf{r}')\rangle$ is used to quantify the speckle size. By fitting the spatial auto-correlation function to

$$\Gamma = \frac{1}{2}\left(1 + e^{\frac{2|\mathbf{r}-\mathbf{r}'|^2}{\sigma^2}}\right), \tag{3.3}$$

in the 2D plane $\mathbf{r} = (x, y)$, we obtain a correlation length $\sim 1.29a$, that is slightly larger than the lattice spacing. In addition, the orientation of laser speckles in White et. al.[1] does not coincide with the lattice axes; the z-axis in Eq. (3.2) points along $\frac{1}{2}\mathbf{n_1} + \frac{1}{2}\mathbf{n_2} + \frac{1}{\sqrt{2}}\mathbf{n_3}$ of the optical lattice. The total external potential is a superposition of the periodic lattice potential and the speckle potential $U(\mathbf{r}) = U_L(\mathbf{r}) + U_D(\mathbf{r})$.

The ^{87}Rb scattering length is chosen to be $a_s = 100a_0 = 5.29$ nm, where $a_0 = 0.0529$ nm is the Bohr radius. In units of the lattice spacing, $a_s = 0.013a$.

3.2 Wannier representation and lattice model

In this chapter, we consider the problem of mapping a disordered single body potential to a lattice model. By removing the high energy states associated with the continuum, the Monte Carlo simulation becomes more efficient. In particular, efficient algorithms have been developed [3][4] for lattice models. Consider the continuum Hamiltonian of N atoms with mass m moving in the external potential $U(\mathbf{r})$ and interacting with the pairwise potential energy $V(\mathbf{r}_\alpha - \mathbf{r}_\beta)$

$$\hat{\mathcal{H}}_N = \sum_{\alpha=1}^{N}\left[\frac{\mathbf{p}_\alpha^2}{2m} + U(\mathbf{r}_\alpha)\right] + \sum_{\alpha<\beta} V(\mathbf{r}_\alpha - \mathbf{r}_\beta), \tag{3.4}$$

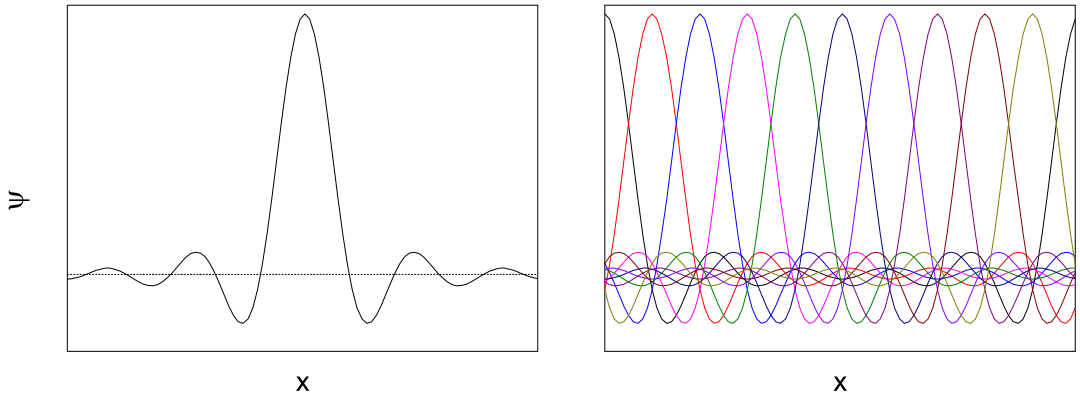

Figure 3.1: A sketch of a set of 10 Wannier states in a one-dimensional periodic lattice. Wiggles around zero can be observed at the tail of a Wannier states, which is essential for the orthogonality condition.

where indices α, β label the atoms. On the other hand, the quantum mechanics of particles moving in a lattice is conveniently described in a basis of localized wave functions, such as the Wannier functions associated with a periodic potential. Using these localized functions, we can define an effective lattice Hubbard Hamiltonian. Written in second quantized notation it has the form:

$$\begin{aligned} \hat{h} &= -\sum_{\langle ij\rangle} t_{ij} a_i^\dagger a_j + \sum_i \epsilon_i n_i + \frac{1}{2}\sum_i u_i n_i (n_i - 1) \\ &\quad -\sum_{\{ij\}} \tilde{t}_{ij} a_i^\dagger a_j + \frac{1}{2}\sum_{\langle ij\rangle} \tilde{u}_{ij} n_i n_j + \cdots\cdots, \end{aligned} \tag{3.5}$$

where i labels the single particle states (lattice sites), $\langle ij\rangle$ denotes a nearest neighbor pair and $\{ij\}$ a next-nearest neighbor pair, t_{ij} and $\tilde{t}_{ij}$ are hopping coefficients, ϵ_i is the on-site energy, u_i is the on-site interaction and $\tilde{u}_{ij}$ is the nearest neighbor off-site interaction. (Terms such as next-nearest neighbor hopping and offsite interaction are often neglected.) Note that $\hat{\mathcal{H}}_N$ refers to the N-body Hamiltonian in continuous space and $\hat{h}$ to its equivalent on a lattice.

In a periodic potential, Wannier functions of a given band are related to the Bloch functions $\psi_{n\mathbf{k}}$ of the same band n by the unitary transformation

$$w_{ni}(\mathbf{r}) = w_n(\mathbf{r} - \mathbf{R}_i) = \frac{1}{\sqrt{N}} \sum_{\mathbf{k}} \psi_{n\mathbf{k}}(\mathbf{r}) e^{-i\mathbf{k}\cdot\mathbf{R}_i}. \tag{3.6}$$

w_{ni} is localized around the lattice site $\mathbf{R}_i$ [5]. A sketch of the Wannier states in a one-dimenional periodic lattice is shown in Fig. (3.1). However, in the absence of periodicity, the concept of Wannier functions needs to be generalized. Two main types of generalizations exist in literature. The perturbative approach [6] assumes the existence of the band structure and thus is applicable to nearly periodic potentials. The variational approach [7][8][9] emphasizes the minimization of the spatial spread with respect to unitary transformations of a starting basis set, for example the Wannier functions of a periodic potential.

In order to be useful, we would like the generalized Wannier functions to have the following properties. First, localization is required by the physical picture of particles hopping in the lattice. Second, a correct description of the low energy density of states is necessary to capture the low temperature physics. Third, for convenience, the orthogonality of the basis set is required to use commutation relations of creation and annihilation operators in the second quantized Hamiltonian. Finally, we would like the lattice Hamiltonian to be free of the sign problem so that quantum Monte Carlo calculations are efficient. This requires the off-diagonal elements to be non-positive(*i.e.* $t_{ij} \geq 0$). Note that the original Hamiltonian $\hat{\mathcal{H}}_N$ has this property.

In section (3.3), we propose a method of constructing localized single particle basis functions based on imaginary time evolution of localized basis functions: $w_i(0)$ where i labels the site.

$$|w_i(\tau)\rangle \equiv e^{-\tau\hat{\mathcal{H}}_1}|w_i(0)\rangle\,, \tag{3.7}$$

where $\hat{\mathcal{H}}_1$ denotes the one particle continuum Hamiltonian. This has the effect of suppressing the high energy components but also spreading out the basis states. In section (3.4), tests of localization and energy convergence are examined for the specific disorder probed experimentally.

3.3 Construction of localized wavefunctions

In constructing a lattice model, our goal is to coarse grain the description of the continuum system, so that instead of recording the precise position of an atom, we only record which lattice site it occupies. We match up the lattice and continuum models using the density matrix; we require that the low temperature single particle density matrix of the lattice model to be identical to that of the continuum system when one integrates over coordinate scales smaller than the lattice spacing. Use of the density matrix is motivated by the fact that the linear response of a system to an external perturbation, either an external field, or particle insertion, or a coupling to another subsystem is determined by its one-body density matrix [10][11]. If we match the density matrices, the lattice system is guaranteed to have not only the same density distribution $n(\mathbf{r})$ and hopping properties, such as diffusion, but also the same response to external perturbations as the continuum system.

The unnormalized single particle density matrix in the continuum system is defined by:

$$\rho\left(\mathbf{r},\mathbf{r}';\tau\right)=\langle\mathbf{r}|e^{-\tau\hat{\mathcal{H}}_1}|\mathbf{r}'\rangle. \tag{3.8}$$

Let $w_i(\mathbf{r};0)$ be a localized basis which assigns atoms to lattice sites, e.g. $w_i(\mathbf{r};0)=$ constant if $|\mathbf{r}-\mathbf{R}_i|$ is minimized with respect to i, i.e. in the i^{th} Wigner-Seitz cell. Then a course-grained density matrix is defined as

$$\begin{aligned} S_{ij}(\tau) &= \langle w_i(0)|e^{-\tau\hat{\mathcal{H}}_1}|w_j(0)\rangle \\ &= \int d\mathbf{r}d\mathbf{r}' w_i^*(\mathbf{r};0)\rho(\mathbf{r},\mathbf{r}';\tau)w_j(\mathbf{r}';0). \end{aligned} \tag{3.9}$$

Note that if $w_i(\mathbf{r};0)$'s are chosen to be everywhere positive, all elements of the lattice density matrix S_{ij} are also positive and can be used directly in a lattice QMC calculation to define the probability of a path on the lattice. We now want to construct a single-particle Hamiltonian, which when solved, gives $S_{ij}(\tau)$ for large τ, or in matrix notation to determine $\hat{h}$ such that

$$\hat{S}(\tau)=e^{-\tau\hat{h}}. \tag{3.10}$$

(S is Hermitian and positive definite, so h exists uniquely.) Formally, the solution $\hat{h} = -\tau^{-1}\log\hat{S}(\tau)$ may have some τ dependance and not necessarily have the other properties mentioned above. Differentiating Eq. (3.10) with respect to τ and multiplying on the right and left by $\hat{S}^{-1/2}$, we find an expression for h in terms of S:

$$\hat{h} = -\hat{S}^{-\frac{1}{2}}\frac{d\hat{S}}{d\tau}\hat{S}^{-\frac{1}{2}} - \int_0^\tau e^{(\frac{\tau}{2}-\lambda)\hat{h}}\left(\frac{d\hat{h}}{d\tau}\right)e^{(\lambda-\frac{\tau}{2})\hat{h}}d\lambda. \tag{3.11}$$

If we assume that h becomes τ-independent as $\tau \to \infty$, we can neglect the second term on the right hand side and find:

$$\hat{h} = -\hat{S}^{-\frac{1}{2}}\frac{d\hat{S}}{d\tau}\hat{S}^{-\frac{1}{2}}. \tag{3.12}$$

Consider the eigenfunction expansion of the continuum density matrix:

$$\rho(\mathbf{r},\mathbf{r}';\tau) = \sum_\alpha \phi_\alpha^*(\mathbf{r})\phi_\alpha(\mathbf{r}')e^{-\tau E_\alpha}, \tag{3.13}$$

where E_α and ϕ_α are the 1-particle eigenvalues and eigenfunctions of the continuum Hamiltonian. For a sufficiently large τ, and for a system with a gap, only states below the gap will survive. If there are N such states, it is clear that we will capture the density of states with exactly N basis functions w_i. Now let us define the orthogonalized basis by splitting up the density operator

$$\exp\left(-\tau\hat{\mathcal{H}}_1\right) = \exp\left(-\frac{1}{2}\tau\hat{\mathcal{H}}_1\right)\exp\left(-\frac{1}{2}\tau\hat{\mathcal{H}}_1\right) \tag{3.14}$$

and having it act partially to the left and right in Eq. (3.9). Combining Eq. (3.9) and Eq.(3.12), we obtain the expression for the model Hamiltonian:

$$\begin{aligned} h_{ij} &= \sum_{kl} S_{ik}^{-\frac{1}{2}}(\tau)\langle w_k(\tau/2)|\hat{\mathcal{H}}_1|w_l(\tau/2)\rangle S_{lj}^{-\frac{1}{2}}(\tau) \\ &= \langle\tilde{w}_i(\tau/2)|\hat{\mathcal{H}}_1|\tilde{w}_j(\tau/2)\rangle, \end{aligned} \tag{3.15}$$

where $w_i(\tau) = e^{-\tau\hat{\mathcal{H}}_1}w_i(0)$ are the non-orthonormalized basis functions at time τ and

$\tilde{w}(\tau/2) = \hat{S}^{-1/2}(\tau)w(\tau/2)$ are the orthonormalized basis functions because

$$S_{ij}(\tau) = \langle w_i(\tau/2)|w_j(\tau/2)\rangle \tag{3.16}$$

is the overlap matrix. This is known as *Löwdin orthogonalization* [12][1].

The imaginary time evolution is equivalent to a diffusion process with sinks or sources determined by the potential $U(\mathbf{r})$. Without a potential present, an initially localized distribution will spread out as $\sqrt{\tau}$ as a function of imaginary time. When the wavepacket (or basis function) $|w_i(\tau)\rangle \equiv e^{-\tau\hat{\mathcal{H}}_1}|w_i(0)\rangle$ encounters the regions of high potential energy separating the lattice sites, its diffusion will stop, until it tunnels through to the next site. If the assumption of temperature-independence

$$\lim_{\tau\to\infty}\left(\frac{d\hat{h}}{d\tau}\right) = 0 \tag{3.17}$$

is correct, according to Eq. (3.15), the orthogonalized basis $\hat{S}^{-1/2}(2\tau)|w_i(\tau)\rangle$ converges at large τ. Instead of taking the logarithm of the reduced density matrix Eq. (3.10), we choose to construct the lattice Hamiltonian from Eq. (3.12) for two reasons. Firstly, numerical tests show that Eq. (3.12) converges faster than $-\frac{1}{\tau}\log\hat{S}$ as τ increases. Secondly, the explicit construction of basis functions enables us to calculate the interaction terms in the second quantized many body Hamiltonian. Finally, use of Eq. (3.12) instead of Eq. (3.10) gives energy levels which lie above their counterparts in the continuum system.

The choice of the initial basis functions $w_i(\mathbf{r};0)$ is to some extent arbitrary, as long as they are non-negative and localized. It is reasonable to suppose that there should be one basis function for each lattice site, at least for weak disorder. In this work, where the disordered potential is an order of magnitude smaller than the lattice potential, we chose to set $w_i(\mathbf{r};0) = \sigma^{-\frac{3}{2}}$ inside a cube of side σ centered on $\mathbf{R}_i$.

When the disordered potential becomes as strong as the lattice potential, the original lattice bands can strongly overlap, and this simple choice may be inadequate. Multi-band

[1]This is mathematically equivalent to the procedure for periodic potentials introduced by Wannier[5].

effects would necessitate the inclusion of more than one basis functions for each lattice site. Also one might want to use the freedom to choose the locations of the basis functions, by concentrating more basis functions in regions of low potential energy. We do not explore these issues further in this paper because the disorder we consider is weak.

3.4 Numerical algorithm and tests

We proposed a method to construct localized single-particle wave functions using imaginary time projection. In this section we outline the numerical implementations and apply the method to a specific disordered potential generated by an optical lattice experiment. Tests of localization and energy convergence are examined to justify the assumpation of temperature-independence Eq (3.17).

3.4.1 Algorithm for imaginary time projection and orthogonalization

To apply the imaginary time evolution to the construction of localized wave functions and thereby to extract microscopic parameters of the corresponding lattice model, we then start with N initial trial wave functions, each of which is well localized in one lattice cell. Each wave function is *independently* evolved over a sufficiently long imaginary time. The set of N wave functions are then transformed into an orthonormal basis.

To perform the imaginary time evolution, consider the Trotter formula[13]

$$e^{-\beta\hat{\mathcal{H}}_1} = \lim_{n\to\infty}\left(e^{-\frac{\beta}{n}\hat{T}}e^{-\frac{\beta}{n}\hat{U}}\right)^n. \tag{3.18}$$

In a coordinate representation, a single step of imaginary time τ can be written as:

$$\begin{aligned} w(\mathbf{r}, t+\tau) &= \int d^3\mathbf{r}'\langle\mathbf{r}|e^{-\tau\hat{\mathcal{H}}_1}|\mathbf{r}'\rangle w(\mathbf{r}', t) \\ &= \left(\frac{m}{2\pi\hbar\tau}\right)^{3/2}\int d^3\mathbf{r}' e^{-\frac{m}{2\hbar\tau}(\mathbf{r}'-\mathbf{r})^2}e^{-\frac{\tau U(\mathbf{r}')}{\hbar}}w(\mathbf{r}', t). \end{aligned} \tag{3.19}$$

This integral is a convolution, and can be efficiently evaluated by Fast Fourier Transform

$$w(\mathbf{r}, t+\tau) = \mathrm{FFT}\left[e^{-\frac{\tau\hbar\mathbf{k}^2}{2m}} f_{\mathbf{k}}\right], \tag{3.20}$$

where $f_{\mathbf{k}}$ is defined as an inverse-Fourier transform

$$f_{\mathbf{k}} = \mathrm{FFT}^{-1}\left[e^{-\frac{\tau U(\mathbf{r})}{\hbar}} w(\mathbf{r}, t)\right]. \tag{3.21}$$

We can also take advantage of the localization of $w(\mathbf{r})$: it is vanishingly small away from its initial site, so that we only store its values in a cube enclosing the region in which the wave function is non-zero. When doing the second FFT, Eq. (3.20), we add a buffer layer outside the cube with thickness chosen so that the localization region of the evolved function over one imaginary time step does not exceed the cube in which FFT is performed; the thickness is proportional to $\sqrt{\tau/m}$. We periodically examine the evolved basis set, to determine if the cube can be made smaller. A common normalization factor is required for all basis functions occassionally to avoid numerical overflow or underflow.

Eq. (3.12) demands orthogonalization of the basis set. Löwdin orthogonalization preserves, as much as possible, the localization and symmetry of the original non-orthogonal basis states. In terms of the overlap matrix, we construct a set of orthogonalized states

$$|\tilde{w}_i\rangle = \sum_j (S^{-1/2})_{ij} |w_j\rangle. \tag{3.22}$$

No other set of orthonormal states generated from the space spanned by the original non-orthogonal set of states resemble the original set more closely, in the least squares sense, than does the Löwdin set[14]. Explicitly, Löwdin orthogonalization minimizes the expression

$$\phi(\hat{T}) \equiv \sum_{i=1}^{N} \|\hat{T} w_i - w_i\|^2 \tag{3.23}$$

over all linear transformations $\hat{T}$ which transform the original non-orthonormal set of states

$|w_i\rangle$ into an orthonormal set of states $|\tilde{w}_i\rangle$

$$\langle \tilde{w}_i, \tilde{w}_j \rangle \equiv \langle \hat{T} w_i, \hat{T} w_j \rangle = \delta_{ij}. \tag{3.24}$$

For efficiency, this procedure can be done in an iterative fashion. Because the original non-orthogonal set of wave functions are localized, the overlap matrix S_{mn} has the form of the identity matrix plus a small off-diagonal part

$$S_{ij} = \delta_{ij} + A_{ij}, \tag{3.25}$$

where the diagonal elements of A are zero and the off-diagonal elements $|A_{mn}| \ll 1$. This enables us to perform Löwdin orthogonalization iteratively by repeated application of the approximate inverse square root of the overlap matrix

$$(\hat{S}^{-1/2})_{ij} \approx \delta_{ij} - \frac{1}{2} A_{ij} \tag{3.26}$$

to the non-orthogonal basis set by updating the overlap matrix at each step [15]. Hence the basis set is iterated as:

$$\tilde{w} \leftarrow \left(\mathbf{1} - \frac{1}{2} \hat{A} \right) \tilde{w} \tag{3.27}$$

until convergence is reached, $|\hat{A}| \sim 0$. The convergence of the overlap matrix to identity matrix is geometric.

The iterative scheme is efficient for large systems because the basis sets are sparse. The computation time of this algorithm is linear in the number of lattice sites, i.e. the complexity is proportional to

$$(\#\,\text{of steps}) \cdot M \cdot n \log n, \tag{3.28}$$

where M is the number of lattice sites and n is the number of mesh points for each basis function.

3.4.2 Hubbard parameters

Once the orthogonalized basis set has been constructed, the effective lattice Hamiltonian is obtained. For convenience we drop the τ dependance. According to Eq. (3.15), the single particle Hubbard parameters are calculated as the on-site energies:

$$\epsilon_i = \int \tilde{w}_i^*(\mathbf{r})\hat{\mathcal{H}}_1\tilde{w}_i(\mathbf{r})d^3\mathbf{r}, \tag{3.29}$$

and the hopping coefficients:

$$t_{ij} = -\int \tilde{w}_i^*(\mathbf{r})\hat{\mathcal{H}}_1\tilde{w}_j(\mathbf{r})d^3\mathbf{r}. \tag{3.30}$$

The interaction term is computed from first-order perturbation theory in V. In the case of a contact interaction with the scattering length a_s we find for u:

$$u_i = \frac{4\pi a_s\hbar^2}{m}\int |\tilde{w}_i(\mathbf{r})|^4\, d^3\mathbf{r}, \tag{3.31}$$

and the off-site interaction

$$\tilde{u}_{ij} = \frac{4\pi a_s\hbar^2}{m}\int |\tilde{w}_i(\mathbf{r})|^2\, |\tilde{w}_j(\mathbf{r})|^2\, d^3\mathbf{r}. \tag{3.32}$$

The problem of a single particle moving in a periodic potential of the form $(\cos x + \cos y + \cos z)$ can be solved analytically [16]. We compared the imaginary time pro- jected states with the results from exact diagonalization; this is shown in Fig. (3.2). We used a spatial grid with 8^3 mesh points per lattice cell and an imaginary time step $\Delta\tau = 10^{-4}E_R^{-1}$. We find the error vanishes linearly as the time step goes to zero.

3.4.3 Measures of localization and energy

Several quantities can be used to characterize the localization and accuracy of the basis set. The spatial spread $\Omega_w \equiv \langle r^2\rangle_w - \langle \mathbf{r}\rangle_w^2$ quantifies the localization of a wave function.

The off-site integral $\tilde{u}_{ij}$ measures the spatial overlap between a pair of basis states. If it

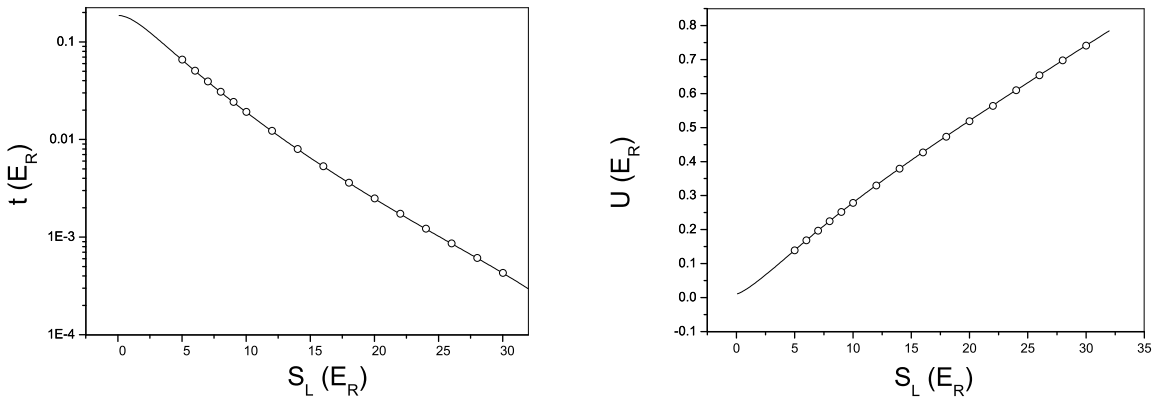

Figure 3.2: Hubbard parameters for a periodic lattice potential $S_L(\cos x + \cos y + \cos z)$ as a function of the lattice depth S_L. The open circles are results obtained from the method of imaginary time projection proposed in this work and the solid lines correspond to exact solutions. **Left**: Nearest neighbor hopping coefficients. **Right**: Hubbard-U interaction parameter.

is small relative to t_{ij} and the Hubbard U, the approximation of keeping only the on-site interaction in the lattice model is appropriate. Its rms value over all nearest neighbor pairs measures the whole basis set.

The convergence rate of the $N \times N$ matrix of the single particle lattice Hamiltonian is measured by the time derivatives of its N eigenvalues $E^{(i)}_{\text{lattice}}$'s,

$$\Gamma = \frac{1}{N} \sum_i \left| \frac{d}{d\tau} E^{(i)}_{\text{lattice}} \right|. \tag{3.33}$$

To determine the accuracy of the basis set we compare $E^{(i)}_{\text{lattice}}$'s with the lowest N eigenvalues $E^{(i)}_{\text{exact}}$ of the original continuum Hamiltonian $\hat{\mathcal{H}}_1$ estimated from

$$E^{(i)}_{\text{exact}} = E^{(i)}_{\text{lattice}}(\tau \to \infty). \tag{3.34}$$

The *worst case error* is defined as

$$e_{\text{lattice}} \equiv \max_i \left| E^{(i)}_{\text{lattice}} - E^{(i)}_{\text{exact}} \right|. \tag{3.35}$$

We did the same estimate for the lattice Hamiltonian that has only nearest neighbor hopping

terms.

3.4.4 Test for a disordered lattice

We now test the numerical method on a disordered lattice potential created in the White et. al. experiment [1]. In the following we express all energies in terms of the recoil energy $E_R = \frac{\hbar^2 k^2}{2m} = \frac{\hbar^2 \pi^2}{2ma^2}$ and all lengths in terms of the lattice spacing $a = 406$ nm. In these units the single particle Hamiltonian is:

$$\mathcal{H}_1 = -\frac{\nabla^2}{\pi^2} + \frac{U(\mathbf{r})}{E_R}, \tag{3.36}$$

where the total external potential is a superposition of the periodic lattice potential and the disordered speckle potential $U(\mathbf{r}) = U_L(\mathbf{r}) + U_D(\mathbf{r})$. The problem of a single particle moving in $U(\mathbf{r}) = U_L(\mathbf{r})$ in the absence of disorder can be solved analytically [16]. We compared the imaginary time projected states with the results from exact diagonalization using the same spatial grid of 8^3 mesh points per lattice cell. We find perfect agreement in the limit of zero time step. We constructed a disordered potential to match the experiment[1] as closely as possible. In the following, S_L and S_D are given in units of E_R.

To investigate the evolution of lattice Hamiltonian Eq. (3.12), at every step of the imaginary time, the basis set is orthonormalized before constructing the Hamiltonian matrix and calculating the energies $E^{(i)}_{\text{lattice}}$. Then the basis set is evolved using the previous basis set before orthonormalization; each basis function is evolved independently.

To illustrate the convergence of the matrix elements of the lattice Hamiltonian, the evolution diagram of an on-site energy on one particular site and a nearest neighbor hopping coefficient on one particular bond for $S_L = 14$ and $S_D = 1$ are shown in the right panel of Fig. (3.3). We characterize the localization of the basis functions by the average nearest neighbor off-site integral $\tilde{u}_{ij}$, which measures the spatial overlap between a pair of nearest neighbor basis functions. The right panel of Fig. (3.3) shows the evolution diagrams of the average on-site interaction u_i and the average off-site interaction $\tilde{u}_{ij}$, which are also converging at large imaginary time. The limiting value of the off-site interaction is $4 \sim 5$

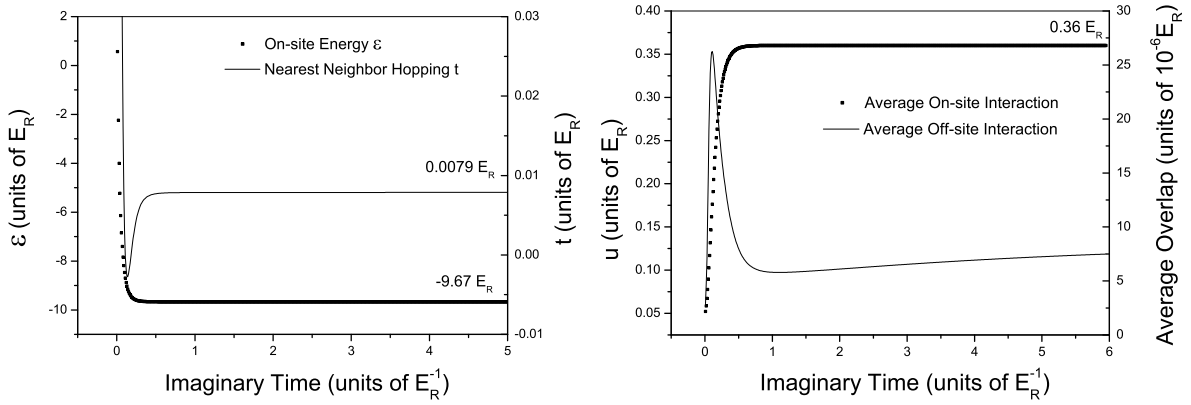

Figure 3.3: **Left**: Evolution diagram of an on-site energy(left scale) and a nearest neighbor hopping coefficient(right scale) in a lattice for $S_L = 14$ and $S_D = 1$. At large imaginary time τ, these two matrix elements approach constant values. **Right**: Evolution diagram of the average on-site interaction u(left scale) and the average nearest neighbor off-site interaction $\tilde{u}$(right scale) for $S_L = 14$ and $S_D = 1$. Note that $\tilde{u}$ measures the localization of a pair of basis functions. The diagram shows that limiting value of $\tilde{u}$ is $4 \sim 5$ orders of magnitude smaller than that of u, which indicates that the basis functions at large imaginary time are still localized.

orders of magnitude smaller than that of the on-site interaction, which means that the basis functions are still localized at large imaginary time. Note that although the imaginary time projection operator $e^{-\tau\hat{\mathcal{H}}_1}$ spreads out the basis states, Löwdin orthogonalization operator $\hat{S}^{-1/2}$ restores their localization.

To illustrate the effect of Lowdin orthogonalization on localization, the evolution diagram for $S_L = 14$ and $S_D = 1$ is shown in the left panel of Fig. (3.4) by including the off-site integral of the set before orthogonalization. It can be seen from the graph that Lowdin procedure helps to localize the basis functions $w(\tau)$.

The localization characterized by the spatial spread Ω_w and drift D_w is shown in the right panel of Fig. (3.4). The maximum value among all basis functions is chosen to measure the whole basis set. As shown in the graph, the values that these two quantities asymptotes to at large time are small compared to the lattice constant, which signifies that the basis functions are localized. This result indicates that for weak disorder, the basis set of wave functions produced by imaginary time evolution which span the lowest-energy manifold are indeed sufficiently localized around the original lattice sites of the simple cubic lattice.

The convergence rate Γ of eigen-energies of the lattice Hamiltonian is shown in the left

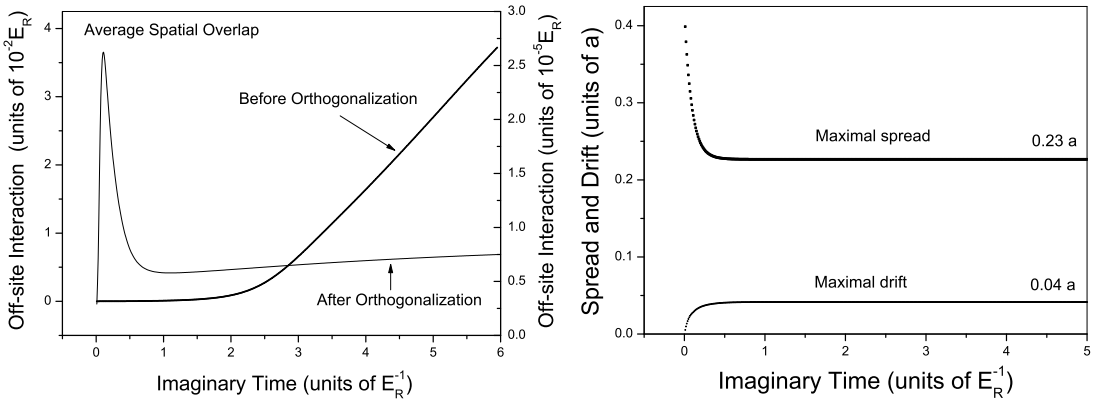

Figure 3.4: **Left**: Evolution diagram of the average nearest neighbor off-site interaction $\tilde{u}$ before orthogonalization(left scale) and after orthogonalization(right scale) for $S_L = 14$ and $S_D = 1$. **Right**: Evolution diagram of the maximum spatial spread and drift(average deviation from the initial position) in units of the lattice constant for $S_L = 14$ and $S_D = 1$. The values that these two quantities approach at large imaginary time are small compared to the lattice constant a, which means that the localization the basis functions is preserved.

panel of Fig. (3.5). It can be seen from the graph that the effective lattice Hamiltonian becomes temperature-independent at low temperature. It is also illuminating to look at the evolution diagram of the worst case error Eq. (3.35), as shown in the right panel of Figs. 3.5 where the exact eigen-energies are estimated by

$$E_{\text{exact}}^{(i)} = E_{\text{lattice}}^{(i)}\left(\tau = 8E_R^{-1}\right). \tag{3.37}$$

We compared the worst case error in energy for the nearest neighbor model ($\tilde{t} = 0$) versus the full lattice model. The spatial overlap between basis functions remain negligible at the early stage so that the nearest neighbor model has almost the same spectrum as the full lattice model; the error in energy is reduced as imaginary time evolves. The error in the eigen-energy of the full lattice model decreases as the time step goes to zero, while a finite error persists in the nearest neighbor model because the next nearest neighbor hopping terms are neglected. Note that this error is less than $10^{-4}E_R$, which is the same order of magnitude of the next nearest neighbor hopping coefficients.

To explain how it is possible to suppress the energy of the original localized basis set before causing significant delocalization, it is useful to look at the single particle density

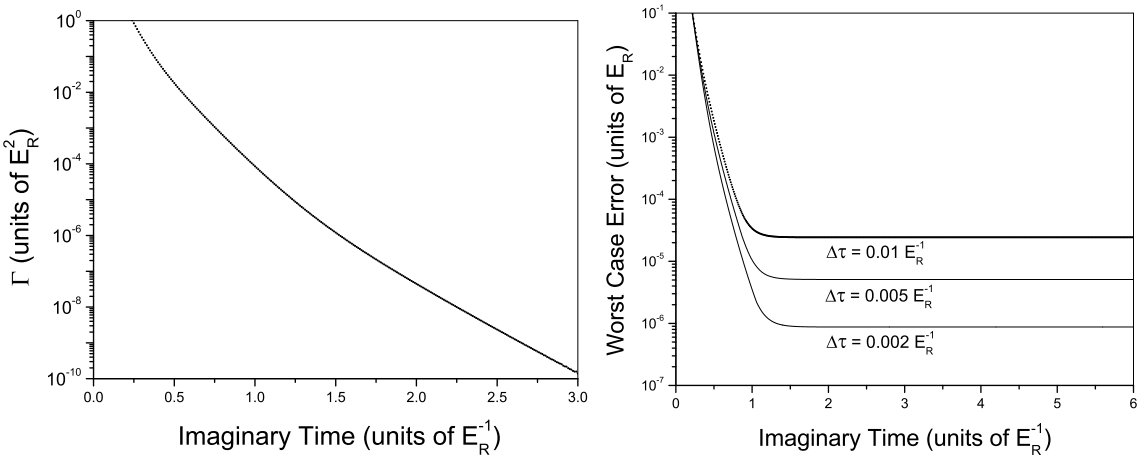

Figure 3.5: **Left**: Convergence rate Γ of eigen-energies for $S_L = 14$ and $S_D = 1$ shown in log-scale. **Right**: Imaginary time evolution of the worst case error in energy for $S_L = 14$ and $S_D = 1$, shown in log-scale. Three different imaginary time steps $\Delta\tau = 0.01E_R^{-1}$, $0.005E_R^{-1}$ and $0.002E_R^{-1}$ are chosen to demonstrate the finite time step error.

of states(DOS). In particular, we are interested in whether the gap between bands persists in the presence of disorder. Fig. (3.6) shows the DOS in the disordered lattice. Fifteen samples each from a 5^3 lattice for each disorder strength were used to determine the DOS. It can been seen from the plot that the lowest band is broadened and skewed by the disorder; there remains a minimum in the density of states between the first band and the second band(pseudo-gap). It is the existence of such a gap that enables us to project out the high energy components in the initial set of trial states before delocalization sets in.

For values of $S_D \geq 2$ ($S_L = 14$), we found rare cases where the highest eigen-energy does not converge to the lowest possible exact solution. Because each wave function is evolved independently before the orthogonalization is performed, the basis set becomes numerically singular at large imaginary time. This problem is more severe for strongly disordered potential where the highest several lattice eigen-states may fail to converge into the lowest energy manifold before the instability sets in.

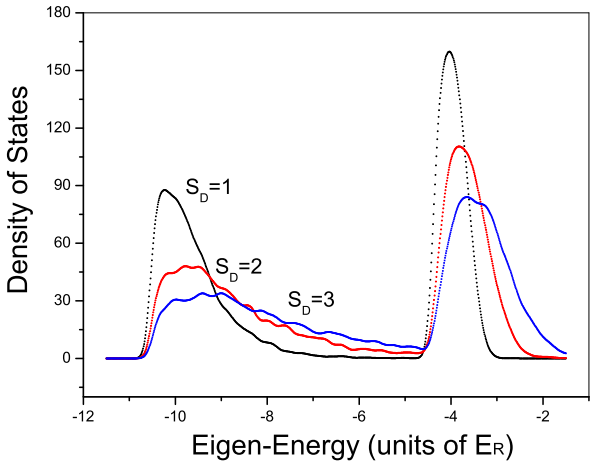

Figure 3.6: Density of states for a single particle in a disordered lattice with $S_L = 14$ and varying amounts of disorder: $S_D = 1, 2, 3$.

3.5 Statistics analysis of Hubbard model parameters

We now discuss the statistical properties of the calculated Hubbard parameters. These are shown in Figs. (3.7) - (3.9) for $S_L = 14$ and $S_D = 1$. About 1000 samples of 6^3 sites are used to construct the probability distributions of Hubbard parameters.

Fig. 3.7 shows the probability distribution of the on-site energy ϵ_i for $S_D = 1$ and $S_L = 14$. The distribution is skewed with a steep onset at low energy and a tail at high energy. We fit the distribution to an exponential decay function

$$P(\varepsilon) \sim \exp\left(-\varepsilon/\Gamma\right) \tag{3.38}$$

for $\varepsilon > -10.5E_R$ finding $\Gamma \approx 0.97E_R$ for $S_D = 1$ and $S_L = 14$. Note that the disorder potential is always positive, so that the on site energy is greater than its value for the periodic lattice which is $-10.58E_R$ for this value of S_L.

Hopping coefficients t_{ij} characterize the mobility of the atoms. Recall that negative values of t will cause difficulty in quantum Monte Carlo calculations. The left panel of Fig. (3.8) shows the probability distribution of nearest neighbor hopping coefficients. This distribution is asymmetrically centered around its value $8 \times 10^{-3} E_R$ for the periodic potential

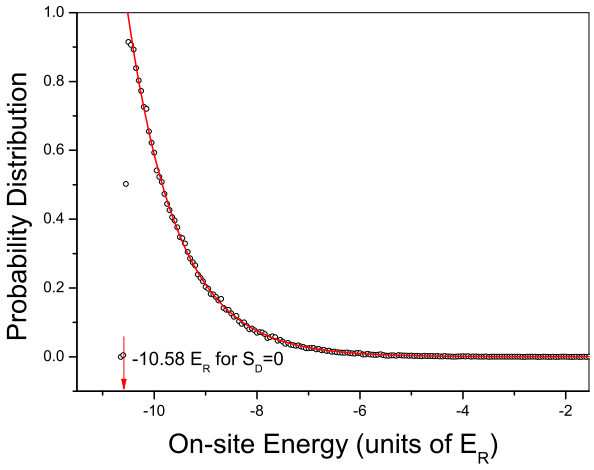

Figure 3.7: Probability distribution of the on-site energy for $S_L = 14$ and $S_D = 1$. The line is a fit to an exponential function.

with a width

$$\frac{\delta t}{\langle t \rangle} = 0.15. \tag{3.39}$$

In 10^6 sampled bonds, only positive $t_{\langle ij \rangle}$ were found. For $S_L = 14$ and for $0.05 \leq S_D \leq 1$, $\delta t / \langle t \rangle$ ranges from 10^{-2} to 10^{-1}.

The right panel of Fig. (3.8) shows the probability distribution of next-nearest neighbor hopping coefficients. This distribution is symmetrically centered around zero with a width $w = 1.25 \times 10^{-5} E_R$ and about 2 orders of magnitude smaller than nearest neighbor hopping. Note that in the clean limit, the next nearest neighbor hopping coefficient is exactly zero for the simple cubic lattice by symmetry. Setting $\tilde{t} = 0$ changes the resulting single particle energies by a maximum of $2 \times 10^{-5} E_R$.

The left panel of Fig. (3.9) shows the probability distribution of the Hubbard U, which is characterized by its narrow peak roughly centered around the value of u in the periodic limit ($0.36 E_R$) with a 1% relative width. We fit this distribution to Laplace function

$$P(u) = \frac{1}{2\Delta} \exp\left(-\frac{|u - u_0|}{\Delta}\right) \tag{3.40}$$

with $u_0 \approx 0.36 E_R$ and $\Delta = 2 \times 10^{-3} E_R$. For $S_L = 14$ and for $10^{-2} \leq S_D \leq 1$, $\delta u / \langle u \rangle$ ranges from 10^{-4} to 10^{-2}. Hence one can assume that the on-site interaction is roughly constant even

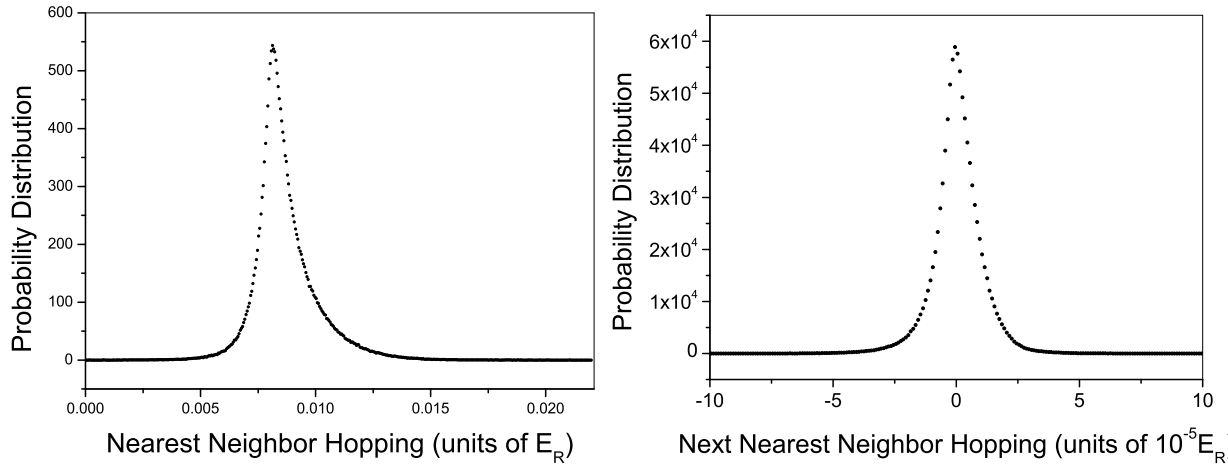

Figure 3.8: **Left**: Probability distribution of the nearest neighbor hopping with $S_L = 14$ and $S_D = 1$. This is a predominantly positive asymmetric distribution. **Right**: Probability distribution of the next nearest neighbor hopping for $S_L = 14$ and $S_D = 1$. This distribution is symmetrically centered around zero.

in the presence of disorder. The right panel of Fig. (3.9) shows the probability distribution of nearest neighbor overlap u. We observe that the magnitude of off-site interactions is almost 4 orders of magnitude smaller than the on-site interaction; evidently negligible in the many-body interacting Hamiltonian.

On-site energies are usually assumed to be almost uncorrelated between different sites. We calculated the nearest neighbor covariance function. For $S_L = 14$ and $S_D = 1$, with $\langle ij \rangle$ nearest neighbor pairs:

$$\frac{\langle \varepsilon_i \varepsilon_j \rangle - \langle \varepsilon_i \rangle \langle \varepsilon_j \rangle}{\langle \varepsilon^2 \rangle - \langle \varepsilon \rangle^2} \approx 0.49. \tag{3.41}$$

The ε_i's are correlated between nearest neighboring sites for this disordered potential.

Fig. (3.10) shows the correlation pattern between the on-site energy difference of nearest neighboring sites and the hopping coefficient. Fit to this joint distribution gives $\left\langle t_{\langle ij \rangle} \right\rangle - t_0 \sim \langle |\epsilon_i - \epsilon_j| \rangle^{\delta}$ with $\delta = 1.05$. Note that in White et. al.[1], the orientation of laser speckles points along $\frac{1}{2}\mathbf{n_1} + \frac{1}{2}\mathbf{n_2} + \frac{1}{\sqrt{2}}\mathbf{n_3}$. The insert of Fig. 3.10 displays the correlation pattern for bonds in $\mathbf{n_3}$-direction if the longitudinal direction of the speckles is aligned with the $\mathbf{n_3}$-axis of the lattice. This illustrates the anisotropy of laser speckles.

The characteristics of the speckle field is reflected in other aspects of the parameters. According to the orientation of laser speckles with respect to the lattice axes, we should

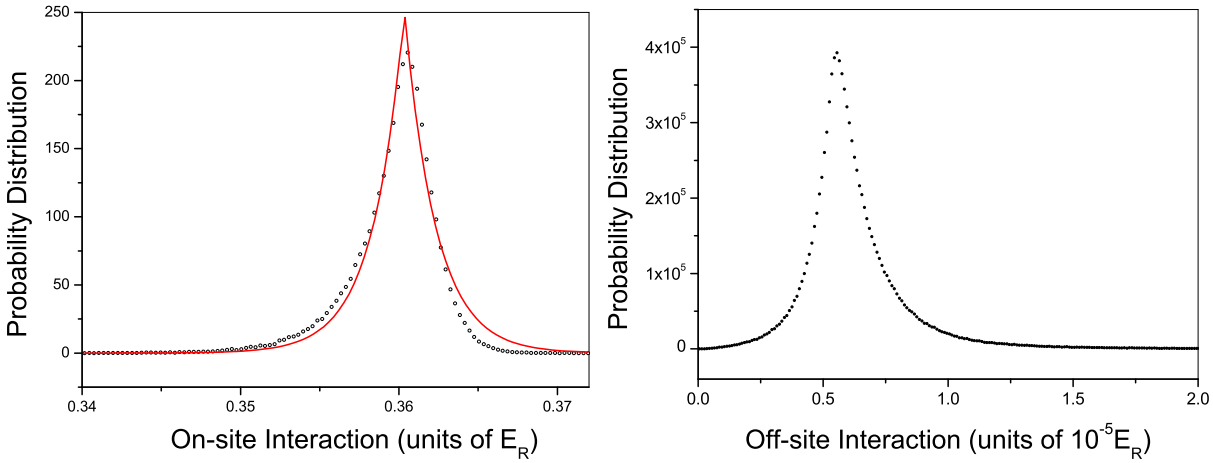

Figure 3.9: **Left**: Probability distribution of the on-site interaction, i.e. Hubbard U, for $S_L = 14$ and $S_D = 1$. The line is a fit to a Laplace function. **Right**: Probability distribution of the nearest neighbor off-site interaction for $S_L = 14$ and $S_D = 1$.

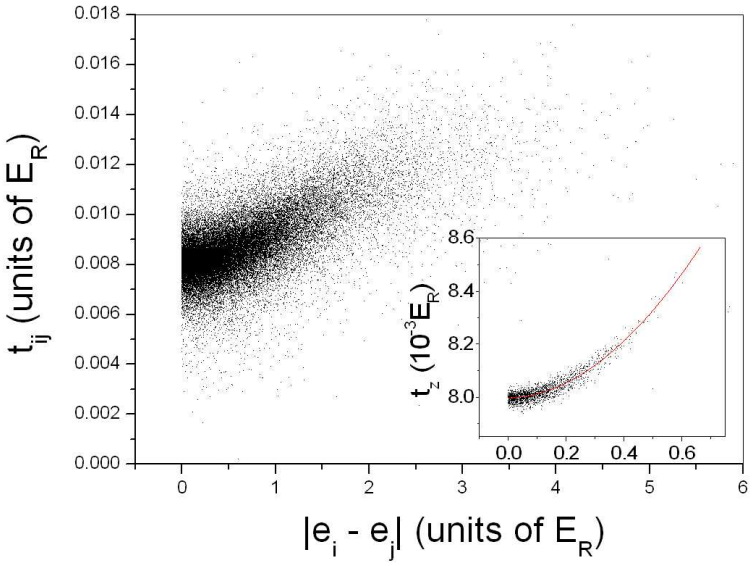

Figure 3.10: Correlation between the on-site energy difference and hopping coefficient between nearest neighbor sites for $S_L = 14$ and $S_D = 1$. The insert displays the correlation pattern for bonds in $\mathbf{n_3}$-direction if the longitudinal direction of the speckles is aligned with the $\mathbf{n_3}$-axis of the lattice. The line in the insert is a fit to a power function.

expect that the average hopping coefficient along $\mathbf{n_1}$ and $\mathbf{n_2}$ to be equal and the hopping along $\mathbf{n_3}$ to be different. As shown in Table 3.1, $\langle t_z \rangle$ differs from those of $\langle t_{x,y} \rangle$ because of the cylindrical symmetry of the speckle. However, the difference is small because the correlation length of the speckle is only slightly larger than the lattice spacing, such that the nearest neighbor hopping is not sensitive to the anisotropy induced by the speckle.

Table 3.1: Anisotropy of speckles for $S_L = 14$. The speckle strength S_D is in units of E_R and the hopping coefficients in units of $10^{-3}E_R$. Statistical errors are smaller than the number of digits shown.

S_D	$\langle t_x \rangle$	$\langle t_y \rangle$	$\langle t_z \rangle$
0.050	8.00	8.00	8.00
0.100	8.02	8.02	8.01
0.250	8.10	8.10	8.07
0.375	8.20	8.20	8.16
0.500	8.32	8.33	8.26
0.750	8.59	8.60	8.48
1.000	8.72	8.73	8.57

In Fig. (3.11) the variation of the distribution widths of all 4 Hubbard parameters versus speckle intensity is shown for $S_L = 14$. Fig. (3.11)-(a) shows the dependence of the width

$$\sigma_\epsilon = \langle \sqrt{(\epsilon_i - \langle \epsilon_i \rangle)^2} \rangle \tag{3.42}$$

for the onsite energy on the disorder strength S_D for $S_L = 14$. It can be seen from the graph that σ increases linearly with the disorder strength, approximately equal to the speckle potential shift. Hence, the width is an appropriate measure of the disorder strength. The linear fit of this functional dependence gives $\sigma_\epsilon = 0.95 \times S_D$. The distribution width of nearest neighbor hopping coefficients and Hubbard U are shown in Fig. (3.11)-(b) and Fig. (3.11)-(c) respectively. In Fig. (3.11)-(d), we show the disorder dependence of the mean value of Hubbard U. It can be seen from the graph that $\langle u \rangle$ is not sensitive to the disorder strength.

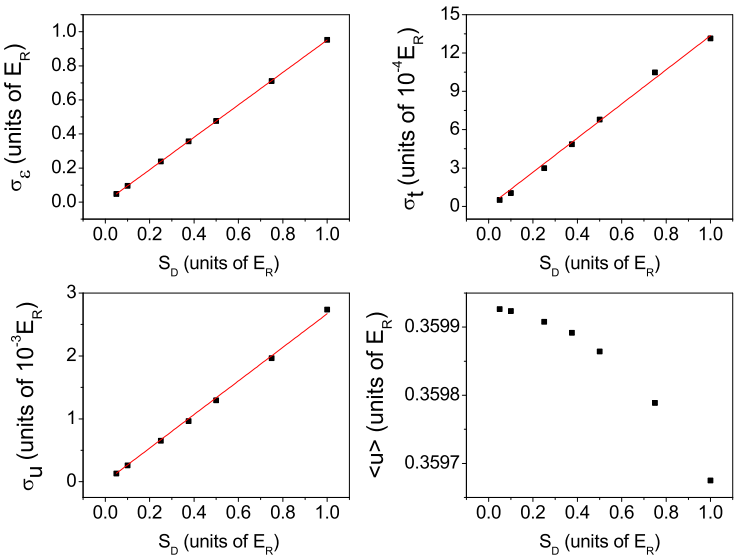

Figure 3.11: The width of the probability distribution for ϵ, t_{ij}, u_i and $\langle u \rangle$ for $S_L = 14$.

3.6 Summary

In this chapter, we developed a method to construct low energy basis states and applied the method to calculate the probability distributions of Hubbard model parameters in a disordered lattice created by an optical speckle field. The imaginary time projection method introduced in this work generates a type of Wannier-like localized basis that satisfies several conditions imposed by a reasonable coarse-grained, effective lattice Hamiltonian.

We compared the single particle energy levels of the effective Hamiltonian with the exact Hamiltonian and found very good agreement, at least for weak disorder. Because we matched the single particle density matrix in the continuum and lattice system, we expect that many-body properties will also be well reproduced. Detailed quantum Monte Carlo calculations using the parameterized Hubbard model is needed to compare with experimental measurements.

The method can be extended in several directions. When the disorder becomes strong enough, at some point, the assumption of one basis function per lattice site will be inadequate. For example, suppose that the potential in the region around one particular site gets sufficiently deep that its first excited state has a lower energy than the ground state

energy of another site so that the bands overlap. Clearly the attractive site needs to be represented with two basis functions. Of course, if the atom-atom potential is repulsive, double occupation of the low energy site will not be energetically favored. In this work, we have not explored the freedom of choosing the number of basis functions, their locations and their detailed form.

A second extension of the method addresses strongly correlated many-body systems. In this chapter we calculated the Hubbard U, using perturbation theory, e.g. Eq. (3.31). However, this will be inadequate when the pair interaction distorts the single particle orbitals. The formalism based on the thermal density matrix still applies, however, one has to work in the two-particle space, instead of in the single particle space. This extension allows one to calculate the Hubbard parameters even when perturbation theory is inaccurate.

References

[1] M. White, M. Pasienski, D. McKay, S. Q. Zhou, D. Ceperley, and B. DeMarco. Strongly interacting bosons in a disordered optical lattice. *Phys. Rev. Lett.*, 102:055301, Feb 2009.

[2] J. W. Goodman. *Speckle Phenomena in Optics*. Roberts and Company Publishers, first edition, 2006.

[3] Olav F. Syljuåsen. Directed loop updates for quantum lattice models. *Phys. Rev. E*, 67:046701, Apr 2003.

[4] N. Prokofev, B. Svistunov, and I. Tupitsyn. Exact, complete, and universal continuous-time worldline monte carlo approach to the statistics of discrete quantum systems. *Journal of Experimental and Theoretical Physics*, 87:310–321, 1998. 10.1134/1.558661.

[5] Gregory H. Wannier. The structure of electronic excitation levels in insulating crystals. *Phys. Rev.*, 52:191–197, Aug 1937.

[6] Michael R. Geller and Walter Kohn. Theory of generalized wannier functions for nearly periodic potentials. *Phys. Rev. B*, 48:14085–14088, Nov 1993.

[7] Nicola Marzari and David Vanderbilt. Maximally localized generalized wannier functions for composite energy bands. *Phys. Rev. B*, 56:12847–12865, Nov 1997.

[8] Ivo Souza, Nicola Marzari, and David Vanderbilt. Maximally localized wannier functions for entangled energy bands. *Phys. Rev. B*, 65:035109, Dec 2001.

[9] Pier Luigi Silvestrelli, Nicola Marzari, David Vanderbilt, and Michele Parrinello. Maximally-localized wannier functions for disordered systems: Application to amorphous silicon. *Solid State Communications*, 107(1):7 – 11, 1998.

[10] Paulo H. Acioli and David M. Ceperley. Generation of pseudopotentials from correlated wave functions. *The Journal of Chemical Physics*, 100(11):8169–8177, 1994.

[11] R. P. Feynman. *Statistical Mechanics*. Westview Press, second edition, 1998.

[12] Per-Olov Lowdin. On the non-orthogonality problem connected with the use of atomic wave functions in the theory of molecules and crystals. *The Journal of Chemical Physics*, 18(3):365–375, 1950.

[13] H. F. Trotter. On the product of semi-groups of operators. *Proc. Amer. Math. Soc.*, 10:545–551, 1959.

[14] John G. Aiken, John A. Erdos, and Jerome A. Goldstein. On löwdin orthogonalization. *International Journal of Quantum Chemistry*, 18(4):1101–1108, 1980.

[15] Uwe Stephan and David A. Drabold. Order-n projection method for first-principles computations of electronic quantities and wannier functions. *Phys. Rev. B*, 57:6391–6407, Mar 1998.

[16] J. C. Slater. A soluble problem in energy bands. *Phys. Rev.*, 87:807–835, Sep 1952.

Chapter 4

Exact Diagonalization Techniques

In this chapter we outline the methods of calculating a few eigenstates of the full Hamiltonian matrix of an interacting quantum system. The numerical implementation of this class of methods naturally implies that the Hilbert space of the problem has to be truncated. Most quantum many-particle problems lead to a sparse matrix representation of the Hamiltonian, where only a small fraction of the matrix elements is non-zero.

4.1 Typical Quantum Many-Particle Model

The Hamiltonian for a system of N interacting particles moving in an external potential has the form

$$\hat{H}_N = \sum_{i=1}^{N} \left[\frac{\mathbf{p}_i^2}{2m} + U(\mathbf{r}_i) \right] + \sum_{i<j=1}^{N} V(\mathbf{r}_{ij}). \tag{4.1}$$

Typical lattice models in solid state physics are derived from the Hamiltonian in continuum Eq.(4.1) written in Wannier reprensentation or discretized on a grid. The resulting lattice Hamiltonian can be expressed in a real space grid basis (1^{st} quantization) or in a particle-number basis (2^{nd} quantization).

4.2 Symmetries and Classification of States

The solutions of the Schrödinger equation can possess at most as many symmetries as the equation (the Hamiltonian operator, the domain and the boundary conditions) itself has. Although the various space symmetries and particle permutations commute with the Hamiltonian, they don't necessarily commute with each other in general.

4.2.1 Notations

To deal with space symmetries, it is convenient to group the x-coordinates of all particles together as $\mathbf{x} = \{x_1, \cdots x_N\}$ and similar for y and z coordinates. Later, when dealing with exchange symmetries, it is convenient to group all coordinates of each particle together as $\mathbf{r}_1 = \{x_1, y_1, z_1\}$; similar for $\mathbf{r}_2, \cdots, \mathbf{r}_N$.

4.2.2 Translations

If we put the system in a finite box with periodic boundary conditions in each direction, the discrete translations $\{\hat{T}_x, \hat{T}_y, \hat{T}_z\}$ by the amount of a grid spacing keep the Hamiltonian invariant. The total momentum operator can always be brought into diagonal form simultaneously with the Hamiltonian operator. For a state $\psi(\mathbf{x}, \mathbf{y}, \mathbf{z})$ with fixed total momentum $\mathbf{K} = (K_x, K_y, K_z)$, the transformation rules under translations are scalar multiplications by phase factors

$$\begin{aligned} \hat{T}_x\psi(\mathbf{x},\mathbf{y},\mathbf{z}) &= \psi(\mathbf{x}+\Delta_x,\mathbf{y},\mathbf{z}) = e^{iK_x\Delta_x}\psi(\mathbf{x},\mathbf{y},\mathbf{z}), \\ \hat{T}_y\psi(\mathbf{x},\mathbf{y},\mathbf{z}) &= \psi(\mathbf{x},\mathbf{y}+\Delta_y,\mathbf{z}) = e^{iK_y\Delta_y}\psi(\mathbf{x},\mathbf{y},\mathbf{z}), \\ \hat{T}_z\psi(\mathbf{x},\mathbf{y},\mathbf{z}) &= \psi(\mathbf{x},\mathbf{y},\mathbf{z}+\Delta_z) = e^{iK_z\Delta_z}\psi(\mathbf{x},\mathbf{y},\mathbf{z}). \end{aligned} \tag{4.2}$$

Note that an eigenstate of Schrödinger equation can always be constructed to be real. If ψ is an eigenstate with energy E: $\hat{H}\psi = E\psi$, the complex conjugate ψ^* is also an eigenstate with energy E, thus the purely real linear combination $\psi + \psi^*$ is an eigenstate with energy E. However, if we insist on the simultaneous diagonalization of total momentum operator $\hat{\mathbf{P}}$ and Hamiltonian operator $\hat{H}$, the eigenstates of $\{\hat{H}, \hat{\mathbf{P}}\}$ are not generally real since the linear combination $\psi + \psi^*$ usually breaks the translational invariance. The special case where both the reality condition and the translational invariance are satisfied is the zero-momentum mode, i.e. $\mathbf{P} = \mathbf{0}$. Thus even though a set of non-commutative operators cannot be brought into diagonal form simultaneously, the zero-mode states can still be formed to be eigenstates of all the non-commutative operators. For example, the three components of

angular momentum $\{\hat{l}_x, \hat{l}_y, \hat{l}_z\}$ do not commute and cannot be simultaneously diagonalized, but the s-state with $l_x = l_y = l_z = 0$ is an eigenstate of $\{\hat{l}_x, \hat{l}_y, \hat{l}_z\}$. This property is frequently utilized in the symmetrization of states in the following sections.

4.2.3 Reflections

The simplest complete set of observables may be chosen as $\{\hat{H}, \hat{R}_x, \hat{R}_y, \hat{R}_z\}$, where $\hat{R}_x$ is the reflection with respect to the plane $x = 0$; similarly for R_y and R_z. By definition,

$$\begin{aligned} \hat{R}_x\psi(\mathbf{x},\mathbf{y},\mathbf{z}) &= \psi(-\mathbf{x},\mathbf{y},\mathbf{z}), \\ \hat{R}_y\psi(\mathbf{x},\mathbf{y},\mathbf{z}) &= \psi(\mathbf{x},-\mathbf{y},\mathbf{z}), \\ \hat{R}_z\psi(\mathbf{x},\mathbf{y},\mathbf{z}) &= \psi(\mathbf{x},\mathbf{y},-\mathbf{z}). \end{aligned} \tag{4.3}$$

Note $[\hat{R}_x, \hat{R}_y] = [\hat{R}_y, \hat{R}_z] = [\hat{R}_z, \hat{R}_x] = 0$. The above three reflections reduce a cubic box to an octant. Another three reflections $\{\hat{R}_{xy}, \hat{R}_{yz}, \hat{R}_{zx}\}$ also commute with the Hamiltonian, $\hat{R}_{xy}$ is the reflection with respect to the plane $x = y$ and in effect interchanges the x and y coordinates; similarly for $\hat{R}_{yz}$ and $\hat{R}_{zx}$. By definition,

$$\begin{aligned} \hat{R}_{xy}\psi(\mathbf{x},\mathbf{y},\mathbf{z}) &= \psi(\mathbf{y},\mathbf{x},\mathbf{z}), \\ \hat{R}_{yz}\psi(\mathbf{x},\mathbf{y},\mathbf{z}) &= \psi(\mathbf{x},\mathbf{z},\mathbf{y}), \\ \hat{R}_{zx}\psi(\mathbf{x},\mathbf{y},\mathbf{z}) &= \psi(\mathbf{z},\mathbf{y},\mathbf{x}). \end{aligned}$$

Notice that $\hat{R}_{xy}$, $\hat{R}_{yz}$ and $\hat{R}_{zx}$ do not commute with each other. Although we can construct a state that is invariant with respect to the above reflections (states with even parity), they cannot simultaneously diagonalized in general. For example, we cannot assume every eigenstate of $\{\hat{H}, \hat{R}_{xy}\}$ to be the eigenstate of $\hat{R}_{yz}$ and $\hat{R}_{zx}$ also.

In one dimension, the only reflection symmetry $\hat{R}$ implies that if ψ is an eigenstate, $R\psi$ is also an eigenstate with the *same* energy. The argument follows that if ψ and $R\psi$ are nondegenerate,

$$\hat{R}\psi = C \times \psi \;\Rightarrow\; \psi = \hat{R}^2\psi = C^2\psi \;\Rightarrow\; C = \pm 1. \tag{4.4}$$

Thus ψ is an eigenstate of reflection operator with eigenvalue $+1$ or -1. In other words, ψ has an even or odd parity. If ψ and $\hat{R}\psi$ are degenerate with energy E, we can always construct

$$\psi_1 = \psi + \hat{R}\psi, \quad \psi_2 = \psi - \hat{R}\psi. \tag{4.5}$$

Then ψ_1 is even under reflection and ψ_2 is odd under reflection. One dimensional case is particularly simple because $\hat{R}$ is the only reflection symmetry and we don't have the issue of noncommutative symmetries.

In two dimensions, we have two commutative reflections $\hat{R}_x$ and $\hat{R}_y$. The fact that they are symmetries means that, if ψ is an eigenstate with energy E, then $\hat{R}_x\psi$, $\hat{R}_y\psi$ and $\hat{R}_x\hat{R}_y\psi$ are also eigenstates with the same energy. Note that the set $\{\mathbf{1}, \hat{R}_x, \hat{R}_y, \hat{R}_x\hat{R}_y\}$ forms a group. In general, suppose ψ, $\hat{R}_x\psi$, $\hat{R}_y\psi$ and $\hat{R}_x\hat{R}_y\psi$ are degenerate, we can then form the proper linear combinations that are either even or odd under reflections $\hat{R}_x$ and $\hat{R}_y$:

$$\begin{aligned}
\psi_0 &= (\mathbf{1} + \hat{R}_x)(\mathbf{1} + \hat{R}_y)\psi \quad \to \quad s : (+1, +1), \quad \text{e.g.} \quad 1 \\
\psi_1 &= (\mathbf{1} + \hat{R}_x)(\mathbf{1} - \hat{R}_y)\psi \quad \to \quad p : (+1, -1), \quad \text{e.g.} \quad \sin y \\
\psi_2 &= (\mathbf{1} - \hat{R}_x)(\mathbf{1} + \hat{R}_y)\psi \quad \to \quad p : (-1, +1), \quad \text{e.g.} \quad \sin x \\
\psi_3 &= (\mathbf{1} - \hat{R}_x)(\mathbf{1} - \hat{R}_y)\psi \quad \to \quad d : (-1, -1); \quad \text{e.g.} \quad \sin x \sin y,
\end{aligned} \tag{4.6}$$

where $(\pm 1, \pm 1)$ indicates the even or odd symmetry under the reflections $\hat{R}_x$ and $\hat{R}_y$ respectively. Free particle solutions in a box are also shown above. This construction enables every eigenstate to be written in the form

$$\hat{R}_x\psi = \sigma_x\psi, \quad \hat{R}_y\psi = \sigma_y\psi, \tag{4.7}$$

where $\sigma_x, \sigma_y = \pm 1$. The square domain can thus be reduced to an quadrant. Note that $\hat{R}_x$ and $\hat{R}_y$ are Hermitian and $\{\psi_i : i = 0, 1, 2, 3\}$ is an orthogonal set.

Now consider the reflection $\hat{R}_{xy}$ which is noncommutative with $\hat{R}_x$ and $\hat{R}_y$. In general, the application of $\hat{R}_{xy}$ on $\{\psi_i : i = 0, 1, 2, 3\}$ produces a linear combination of them. To

exploit the additional noncommutative symmetries, we need to find out the transformation rules. This is related to the group representation theory, but in two dimensions this is fairly simple.

s-state $\psi_0 : (+1, +1)$

To analyze $\hat{R}_{xy}\psi_0$, we simply evaluate the $\hat{R}_x\hat{R}_{xy}\psi_0$ and $\hat{R}_y\hat{R}_{xy}\psi_0$,

$$\hat{R}_x\hat{R}_{xy}\psi_0(\mathbf{x},\mathbf{y}) = \hat{R}_x\psi_0(\mathbf{y},\mathbf{x}) = \psi_0(\mathbf{y},-\mathbf{x}) = \psi_0(\mathbf{y},\mathbf{x}) = \hat{R}_{xy}\psi_0(\mathbf{x},\mathbf{y}). \tag{4.8}$$

Thus $\hat{R}_{xy}\psi_0$ has an even parity $\sigma_x = +1$, and similarly $\sigma_y = +1$. Hence

$$\hat{R}_{xy}\psi_0(\mathbf{x},\mathbf{y}) \equiv \psi_0(\mathbf{y},\mathbf{x}) = \pm\psi_0(\mathbf{x},\mathbf{y}) = \sigma_{xy}\psi_0(\mathbf{x},\mathbf{y}). \tag{4.9}$$

Here $\sigma_{xy} = \pm 1$ is obtained by a repeated application of $\hat{R}_{xy}$. We conclude that ψ_0 is even or odd under the reflection $\hat{R}_{xy}$. For example, $\psi_0(x,y) = 1$ is even under $\hat{R}_{xy}$ and $\psi_0(x,y) = \sin(x^2 - y^2)$ is odd under $\hat{R}_{xy}$, but both of them are even under $\hat{R}_x$ and $\hat{R}_y$. This fact means that the domain of this function can be reduced to a triangle in two dimensions. The odd symmetry under $\hat{R}_{xy}$ introduces nodes, so we take $\sigma_{xy} = +1$ for low-lying eigenstates. We can call ψ_0 an s-state in analogous to the classification by angular momentum.

p-states $\psi_1(+1,-1), \quad \psi_2 : (-1,+1)$

$$\begin{aligned}
\hat{R}_x\hat{R}_{xy}\psi_1(\mathbf{x},\mathbf{y}) &= \hat{R}_x\psi_1(\mathbf{y},\mathbf{x}) = \psi_1(\mathbf{y},-\mathbf{x}) = -\psi_1(\mathbf{y},\mathbf{x}) = -\hat{R}_{xy}\psi_1(\mathbf{x},\mathbf{y}),\\
\hat{R}_y\hat{R}_{xy}\psi_1(\mathbf{x},\mathbf{y}) &= \hat{R}_y\psi_1(\mathbf{y},\mathbf{x}) = \psi_1(-\mathbf{y},\mathbf{x}) = \psi_1(\mathbf{y},\mathbf{x}) = \hat{R}_{xy}\psi_1(\mathbf{x},\mathbf{y}),\\
\hat{R}_x\hat{R}_{xy}\psi_2(\mathbf{x},\mathbf{y}) &= \hat{R}_x\psi_2(\mathbf{y},\mathbf{x}) = \psi_2(\mathbf{y},-\mathbf{x}) = \psi_2(\mathbf{y},\mathbf{x}) = \hat{R}_{xy}\psi_2(\mathbf{x},\mathbf{y}),\\
\hat{R}_y\hat{R}_{xy}\psi_2(\mathbf{x},\mathbf{y}) &= \hat{R}_y\psi_2(\mathbf{y},\mathbf{x}) = \psi_2(-\mathbf{y},\mathbf{x}) = -\psi_2(\mathbf{y},\mathbf{x}) = -\hat{R}_{xy}\psi_2(\mathbf{x},\mathbf{y}).
\end{aligned}$$

Thus we have $(\sigma_x = -1, \sigma_y = +1)$ for $\hat{R}_{xy}\psi_1$ and $(\sigma_x = -1, \sigma_y = +1)$ for $\hat{R}_{xy}\psi_2$. Hence

$$\hat{R}_{xy}\psi_1(\mathbf{x},\mathbf{y}) \equiv \psi_1(\mathbf{y},\mathbf{x}) = C\psi_2(\mathbf{x},\mathbf{y}) = \psi_2(\mathbf{x},\mathbf{y}),$$
$$\hat{R}_{xy}\psi_2(\mathbf{x},\mathbf{y}) \equiv \psi_2(\mathbf{y},\mathbf{x}) = C'\psi_1(\mathbf{x},\mathbf{y}) = \psi_1(\mathbf{x},\mathbf{y}).$$

Here $CC' = 1$ by a repeated application of $\hat{R}_{xy}$ and we have taken the convention $C = C' = 1$. We observe that the p-states ψ_1 and ψ_2 transform to each other upon the reflection $\hat{R}_{xy}$, which means the subspace spanned by $\{\psi_1, \psi_2\}$ is invariant under $\hat{R}_{xy}$.

***d*-state** $\psi_3(-1,-1)$

$$\hat{R}_x\hat{R}_{xy}\psi_3(\mathbf{x},\mathbf{y}) = \hat{R}_x\psi_3(\mathbf{y},\mathbf{x}) = \psi_3(\mathbf{y},-\mathbf{x}) = -\psi_3(\mathbf{y},\mathbf{x}) = -\hat{R}_{xy}\psi_3(\mathbf{x},\mathbf{y}),$$
$$\hat{R}_y\hat{R}_{xy}\psi_3(\mathbf{x},\mathbf{y}) = \hat{R}_y\psi_3(\mathbf{y},\mathbf{x}) = \psi_3(-\mathbf{y},\mathbf{x}) = -\psi_3(\mathbf{y},\mathbf{x}) = -\hat{R}_{xy}\psi_3(\mathbf{x},\mathbf{y}).$$

Thus we have $(\sigma_x = -1, \sigma_y = -1)$ for $\hat{R}_{xy}\psi_3$. Hence,

$$R_{xy}\psi_3(\mathbf{x},\mathbf{y}) \equiv \psi_3(\mathbf{y},\mathbf{x}) = \pm\psi_3(\mathbf{x},\mathbf{y}). \tag{4.10}$$

In three dimensions, we have three commutative reflections $\hat{R}_x$, $\hat{R}_y$ and $\hat{R}_z$. The collection

$$\{\mathbf{1}, \hat{R}_x, \hat{R}_y, \hat{R}_z, \hat{R}_x\hat{R}_y, \hat{R}_y\hat{R}_z, \hat{R}_z\hat{R}_x, \hat{R}_x\hat{R}_y\hat{R}_z\} \tag{4.11}$$

form a closed group. If ψ is an eigenstate with energy E, suppose ψ, $R_x\psi$, $R_y\psi$, $R_z\psi$, $R_xR_y\psi$, $R_yR_z\psi$, $R_zR_x\psi$ and $R_xR_yR_z\psi$ are degenerate. We can then form the proper linear combinations that are either even or odd under reflections $\{\hat{R}_x, \hat{R}_y, \hat{R}_z\}$:

$$\begin{aligned}
\psi_0 &= (\mathbf{1}+\hat{R}_x)(\mathbf{1}+\hat{R}_y)(\mathbf{1}+\hat{R}_z)\psi \quad \rightarrow \quad s:(+1,+1,+1):1,\\
\psi_1 &= (\mathbf{1}-\hat{R}_x)(\mathbf{1}+\hat{R}_y)(\mathbf{1}-\hat{R}_z)\psi \quad \rightarrow \quad p:(-1,+1,+1):\sin x,\\
\psi_2 &= (\mathbf{1}+\hat{R}_x)(\mathbf{1}-\hat{R}_y)(\mathbf{1}+\hat{R}_z)\psi \quad \rightarrow \quad p:(+1,-1,+1):\sin y,
\end{aligned}$$

$$
\begin{aligned}
\psi_3 &= (\mathbf{1}+\hat{R}_x)(\mathbf{1}+\hat{R}_y)(\mathbf{1}-\hat{R}_z)\psi \quad \rightarrow \quad p:(+1,+1,-1):\sin z, \\
\psi_4 &= (\mathbf{1}+\hat{R}_x)(\mathbf{1}-\hat{R}_y)(\mathbf{1}-\hat{R}_z)\psi \quad \rightarrow \quad d:(+1,-1,-1):\sin y \sin z, \\
\psi_5 &= (\mathbf{1}-\hat{R}_x)(\mathbf{1}+\hat{R}_y)(\mathbf{1}-\hat{R}_z)\psi \quad \rightarrow \quad d:(-1,+1,-1):\sin x \sin z, \\
\psi_6 &= (\mathbf{1}-\hat{R}_x)(\mathbf{1}-\hat{R}_y)(\mathbf{1}+\hat{R}_z)\psi \quad \rightarrow \quad d:(-1,-1,+1):\sin x \sin y, \\
\psi_7 &= (\mathbf{1}-\hat{R}_x)(\mathbf{1}-\hat{R}_y)(\mathbf{1}-\hat{R}_z)\psi \quad \rightarrow \quad f:(-1,-1,-1):\sin x \sin y \sin z,
\end{aligned}
\tag{4.12}
$$

where $(\pm 1, \pm 1, \pm 1)$ indicates the even or odd symmetry under the reflections $\hat{R}_x$, $\hat{R}_y$ and $\hat{R}z$ respectively. Free particle solutions in a box are also shown above. This construction enables every eigenstate to be written in the form

$$
\hat{R}_x\psi = \sigma_x\psi, \quad \hat{R}_y\psi = \sigma_y\psi, \quad \hat{R}_z\psi = \sigma_z\psi, \tag{4.13}
$$

where $\sigma_x, \sigma_y, \sigma_z = \pm 1$. The cubic domain can thus be reduced to an octant. Note that $\{\hat{R}_x, \hat{R}_y, \hat{R}_z\}$ are Hermitian and $\{\psi_i : i = 0, 1, \cdots, 7\}$ is an orthogonal set.

The other set of reflections $\{\hat{R}_{xy}, \hat{R}_{xz}, \hat{R}_{yz}\}$ are noncommutative so that we cannot assume each eigenstate of $\{\hat{H}, \hat{R}_x, \hat{R}_y, \hat{R}_z\}$ to be even or odd under the reflections $\{\hat{R}_{xy}, \hat{R}_{xz}, \hat{R}_{yz}\}$. In general, the application of $\hat{R}_{xy}$ on $\{\psi_i : i = 0, 1, \cdots, 7\}$ produces a linear combination of them. To exploit the additional noncommutative symmetries, we need to find out the transformation rules.

s-**state** $\psi_0 : (+1, +1, +1)$

To analyze $\hat{R}_{xy}\psi_0$, we evaluate the $\hat{R}_x\hat{R}_{xy}\psi_0$, $\hat{R}_y\hat{R}_{xy}\psi_0$ and $\hat{R}_z\hat{R}_{xy}\psi_0$:

$$
\hat{R}_x\hat{R}_{xy}\psi_0(\mathbf{x},\mathbf{y},\mathbf{z}) = \hat{R}_x\psi_0(\mathbf{y},\mathbf{x},\mathbf{z}) = \psi_0(\mathbf{y},-\mathbf{x},\mathbf{z}) = \psi_0(\mathbf{y},\mathbf{x},\mathbf{z}) = \hat{R}_{xy}\psi_0(\mathbf{x},\mathbf{y},\mathbf{z}). \tag{4.14}
$$

Thus we have $\hat{R}_x\hat{R}_{xy}\psi_0 = \hat{R}_{xy}\psi_0$, which means $\sigma_x = +1$, and similarly $\sigma_y = \sigma_z = +1$, for $\hat{R}_{xy}\psi_0$. Hence

$$
\hat{R}_{xy}\psi_0(\mathbf{x},\mathbf{y},\mathbf{z}) \equiv \psi_0(\mathbf{y},\mathbf{x},\mathbf{z}) = \pm\psi_0(\mathbf{x},\mathbf{y},\mathbf{z}). \tag{4.15}
$$

So we conclude that ψ_0 is even or odd under the reflection $\hat{R}_{xy}$. This fact means that the domain of ψ_0 can be reduced to a wedge in three dimensions without a loss of information. The odd symmetry under $\hat{R}_{xy}$ introduces nodes, so we usually consider only even symmetry under $\hat{R}_{xy}$ for low-lying eigenstates. Carry through the similar procedure for $\hat{R}_{zx}$ and $\hat{R}_{yz}$, we have

$$\begin{aligned}
\hat{R}_{xy}\psi_0(\mathbf{x},\mathbf{y},\mathbf{z}) &\equiv \psi_0(\mathbf{y},\mathbf{x},\mathbf{z}) = \psi_0(\mathbf{x},\mathbf{y},\mathbf{z}),\\
\hat{R}_{xy}\psi_0(\mathbf{x},\mathbf{y},\mathbf{z}) &\equiv \psi_0(\mathbf{z},\mathbf{y},\mathbf{x}) = \psi_0(\mathbf{x},\mathbf{y},\mathbf{z}),\\
\hat{R}_{xy}\psi_0(\mathbf{x},\mathbf{y},\mathbf{z}) &\equiv \psi_0(\mathbf{x},\mathbf{z},\mathbf{y}) = \psi_0(\mathbf{x},\mathbf{y},\mathbf{z}).
\end{aligned} \tag{4.16}$$

We call ψ_0 an s-state in analogous to the the classification by angular momentum.

p-states $\psi_1(-1,+1,+1)$**,** $\psi_2(+1,-1,+1)$**,** $\psi_3(+1,+1,-1)$

Take ψ_3 for example,

$$\begin{aligned}
&\hat{R}_x\hat{R}_{xy}\psi_3(\mathbf{x},\mathbf{y},\mathbf{z}) = \hat{R}_x\psi_3(\mathbf{y},\mathbf{x},\mathbf{z}) = \psi_3(\mathbf{y},-\mathbf{x},\mathbf{z}) = \psi_3(\mathbf{y},\mathbf{x},\mathbf{z}) = \hat{R}_{xy}\psi_3(\mathbf{x},\mathbf{y},\mathbf{z}),\\
&\hat{R}_y\hat{R}_{xy}\psi_3(\mathbf{x},\mathbf{y},\mathbf{z}) = \hat{R}_y\psi_3(\mathbf{y},\mathbf{x},\mathbf{z}) = \psi_3(-\mathbf{y},\mathbf{x},\mathbf{z}) = \psi_3(\mathbf{y},\mathbf{x},\mathbf{z}) = \hat{R}_{xy}\psi_3(\mathbf{x},\mathbf{y},\mathbf{z}),\\
&\hat{R}_z\hat{R}_{xy}\psi_3(\mathbf{x},\mathbf{y},\mathbf{z}) = \hat{R}_z\psi_3(\mathbf{y},\mathbf{x},\mathbf{z}) = \psi_3(\mathbf{y},\mathbf{x},-\mathbf{z}) = -\psi_3(\mathbf{y},\mathbf{x},\mathbf{z}) = -\hat{R}_{xy}\psi_3(\mathbf{x},\mathbf{y},\mathbf{z}),\\
&\hat{R}_x\hat{R}_{zx}\psi_3(\mathbf{x},\mathbf{y},\mathbf{z}) = \hat{R}_x\psi_3(\mathbf{z},\mathbf{y},\mathbf{x}) = \psi_3(\mathbf{z},\mathbf{y},-\mathbf{x}) = -\psi_3(\mathbf{z},\mathbf{y},\mathbf{x}) = -\hat{R}_{zx}\psi_3(\mathbf{x},\mathbf{y},\mathbf{z}),\\
&\hat{R}_y\hat{R}_{zx}\psi_3(\mathbf{x},\mathbf{y},\mathbf{z}) = \hat{R}_y\psi_3(\mathbf{z},\mathbf{y},\mathbf{x}) = \psi_3(\mathbf{z},-\mathbf{y},\mathbf{x}) = \psi_3(\mathbf{z},\mathbf{y},\mathbf{x}) = \hat{R}_{zx}\psi_3(\mathbf{x},\mathbf{y},\mathbf{z}),\\
&\hat{R}_z\hat{R}_{zx}\psi_3(\mathbf{x},\mathbf{y},\mathbf{z}) = \hat{R}_z\psi_3(\mathbf{z},\mathbf{y},\mathbf{x}) = \psi_3(-\mathbf{z},\mathbf{y},\mathbf{x}) = \psi_3(\mathbf{z},\mathbf{y},\mathbf{x}) = \hat{R}_{zx}\psi_3(\mathbf{x},\mathbf{y},\mathbf{z}),\\
&\hat{R}_x\hat{R}_{yz}\psi_3(\mathbf{x},\mathbf{y},\mathbf{z}) = \hat{R}_x\psi_3(\mathbf{x},\mathbf{z},\mathbf{y}) = \psi_3(-\mathbf{x},\mathbf{z},\mathbf{y}) = \psi_3(\mathbf{x},\mathbf{z},\mathbf{y}) = \hat{R}_{yz}\psi_3(\mathbf{x},\mathbf{y},\mathbf{z}),\\
&\hat{R}_y\hat{R}_{yz}\psi_3(\mathbf{x},\mathbf{y},\mathbf{z}) = \hat{R}_y\psi_3(\mathbf{x},\mathbf{z},\mathbf{y}) = \psi_3(\mathbf{x},\mathbf{z},-\mathbf{y}) = -\psi_3(\mathbf{x},\mathbf{z},\mathbf{y}) = -\hat{R}_{yz}\psi_3(\mathbf{x},\mathbf{y},\mathbf{z}),\\
&\hat{R}_z\hat{R}_{yz}\psi_3(\mathbf{x},\mathbf{y},\mathbf{z}) = \hat{R}_z\psi_3(\mathbf{x},\mathbf{z},\mathbf{y}) = \psi_3(\mathbf{x},-\mathbf{z},\mathbf{y}) = \psi_3(\mathbf{x},\mathbf{z},\mathbf{y}) = \hat{R}_{yz}\psi_3(\mathbf{x},\mathbf{y},\mathbf{z}).
\end{aligned}$$

Thus we have $(+1,+1,-1)$ for $\hat{R}_{xy}\psi_3$, $(-1,+1,+1)$ for $\hat{R}_{zx}\psi_3$ and $(+1,-1,+1)$ for $\hat{R}_{yz}\psi_3$. Hence

$$\begin{aligned}
\hat{R}_{xy}\psi_3(\mathbf{x},\mathbf{y},\mathbf{z}) &\equiv \psi_3(\mathbf{y},\mathbf{x},\mathbf{z}) = \psi_3(\mathbf{x},\mathbf{y},\mathbf{z}),\\
\hat{R}_{zx}\psi_3(\mathbf{x},\mathbf{y},\mathbf{z}) &\equiv \psi_3(\mathbf{z},\mathbf{y},\mathbf{x}) = \psi_1(\mathbf{x},\mathbf{y},\mathbf{z}),\\
\hat{R}_{yz}\psi_3(\mathbf{x},\mathbf{y},\mathbf{z}) &\equiv \psi_3(\mathbf{x},\mathbf{z},\mathbf{y}) = \psi_2(\mathbf{x},\mathbf{y},\mathbf{z}).
\end{aligned} \tag{4.17}$$

Here we have taken all possibly appeared constant coefficients to be unity by suitable normalization convention. The above transformation rules can be understood intuitively. Similar relations can be derived for ψ_1 with $(-1,+1,+1)$:

$$\begin{aligned}
\hat{R}_{xy}\psi_1(\mathbf{x},\mathbf{y},\mathbf{z}) &\equiv \psi_1(\mathbf{y},\mathbf{x},\mathbf{z}) = \psi_2(\mathbf{x},\mathbf{y},\mathbf{z}),\\
\hat{R}_{zx}\psi_1(\mathbf{x},\mathbf{y},\mathbf{z}) &\equiv \psi_1(\mathbf{z},\mathbf{y},\mathbf{x}) = \psi_3(\mathbf{x},\mathbf{y},\mathbf{z}),\\
\hat{R}_{yz}\psi_1(\mathbf{x},\mathbf{y},\mathbf{z}) &\equiv \psi_1(\mathbf{x},\mathbf{z},\mathbf{y}) = \psi_1(\mathbf{x},\mathbf{y},\mathbf{z})
\end{aligned} \tag{4.18}$$

and for ψ_2 with $(+1,-1,+1)$:

$$\begin{aligned}
\hat{R}_{xy}\psi_2(\mathbf{x},\mathbf{y},\mathbf{z}) &\equiv \psi_2(\mathbf{y},\mathbf{x},\mathbf{z}) = \psi_1(\mathbf{x},\mathbf{y},\mathbf{z}),\\
\hat{R}_{zx}\psi_2(\mathbf{x},\mathbf{y},\mathbf{z}) &\equiv \psi_2(\mathbf{z},\mathbf{y},\mathbf{x}) = \psi_2(\mathbf{x},\mathbf{y},\mathbf{z}),\\
\hat{R}_{yz}\psi_2(\mathbf{x},\mathbf{y},\mathbf{z}) &\equiv \psi_2(\mathbf{x},\mathbf{z},\mathbf{y}) = \psi_3(\mathbf{x},\mathbf{y},\mathbf{z}).
\end{aligned} \tag{4.19}$$

The transformation rules in three dimensions are slightly more complicated than in two dimensions. The p-states ψ_1, ψ_2 and ψ_3 transform to each other upon the reflections $\{\hat{R}_{xy}, \hat{R}_{zx}, \hat{R}_{yz}\}$. The subspace spanned by $\{\psi_1, \psi_2, \psi_3\}$ is invariant under $\{\hat{R}_{xy}, \hat{R}_{zx}, \hat{R}_{yz}\}$.

Three d-states and one f-state are usually higher excitations. The similar procedure to derive transformation rules is straightforward.

4.2.4 Particle Permutations

Particle permutations can always be decomposed into successive interchanges of particle pairs, and is often called *exchange symmetries*. Exchange symmetries commute with space symmetries. The invariance of the Hamiltonian of the system with respect to the interchange of particles leads to the fact that, if some function is a solution of Schrödinger equation, the functions obtained from it by various interchanges of the variables will also be solutions. In the general case, the solutions of Schrödinger equation need not necessarily be either symmetric or antisymmetric with respect to the interchange of any pair of particles. It is the principle of indistinguishability of identical particles that dictates the symmetry or antisymmetry of the complete wavefunction (which include the spin factor) when the particles are interchanged.

By considering a system of only two particles, the coordinate wavefunction $\psi(\mathbf{r}_1, \mathbf{r}_2)$ must be either symmetric or antisymmetric, i.e. $\hat{P}_{12}\psi(\mathbf{r}_1, \mathbf{r}_2) = \pm\psi(\mathbf{r}_1, \mathbf{r}_2)$. For a system of two spinless bosons, $\psi(\mathbf{r}_1, \mathbf{r}_2)$ is symmetric. For a system of two spin-1/2 fermions, $\psi(\mathbf{r}_1, \mathbf{r}_2)$ is symmetric if the spin state is a singlet and antisymmetric if the spin state is a triplet. The fact that the Hamiltonian $\hat{H}$ of the system is symmetric with respect to all the particles means, mathematically, that $\hat{H}$ commutes with all the permutation operators $\hat{P}$. These permutation operators, however, do not commute with one another, and so they cannot be simultaneously brought into diagonal form. In the general case of a system of N particles, the wavefunction cannot be chosen that each of them is either symmetric or antisymmetric with respect to all interchanges separately, which is called *mixed-symmetry* (except for a system of two particles, where there is only a single interchange operator, which can be brought into diagonal form simultaneously with the Hamiltonian). Interchanging a pair of particles generally leads to a linear combination of a subspace of degenerate states. For a system of a few particles, the transformation rules under interchanging any pair of particles can be derived without an explicit use of the irreducible representations of the permutation group [1].

For a system of three spin-1/2 fermions, the quantum number of the total spin $S =$

$1/2, 3/2$. There exist two sets of spin-1/2 states and one set of spin-3/2 state. The fully spin-polarized state $\psi(123) = \psi_A(123) \otimes |\uparrow\uparrow\uparrow\rangle$ are totally symmetric under the interchange of any pair of spins, and the spatial wave function must be totally-antisymmetric with respect to the interchange of any pair of cooridnates, i.e.

$$\psi(\mathbf{r}_1, \mathbf{r}_2, \mathbf{r}_3) = -\psi(\mathbf{r}_2, \mathbf{r}_1, \mathbf{r}_3) = \psi(\mathbf{r}_2, \mathbf{r}_3, \mathbf{r}_1) = -\psi(\mathbf{r}_3, \mathbf{r}_2, \mathbf{r}_1) = \psi(\mathbf{r}_3, \mathbf{r}_1, \mathbf{r}_2) = -\psi(\mathbf{r}_1, \mathbf{r}_3, \mathbf{r}_2). \tag{4.20}$$

There are two sets of spin states with $S = 1/2$ (up to const normalization factors),

$$|1/2, +1/2\rangle_A \propto |\uparrow\downarrow\uparrow\rangle - |\downarrow\uparrow\uparrow\rangle,\ |1/2, -1/2\rangle_A \propto |\uparrow\downarrow\downarrow\rangle - |\downarrow\uparrow\downarrow\rangle \tag{4.21}$$

are called *mixed antisymmetric* and

$$|1/2, +1/2\rangle_S \propto |\uparrow\downarrow\uparrow\rangle + |\downarrow\uparrow\uparrow\rangle - 2|\uparrow\uparrow\downarrow\rangle,\ |1/2, -1/2\rangle_S \propto |\uparrow\downarrow\downarrow\rangle + |\downarrow\uparrow\downarrow\rangle - 2|\downarrow\downarrow\uparrow\rangle \tag{4.22}$$

are called *mixed symmetric*. Neither of these two sets of states is totally symmetric or anti-symmetric, the complete wavefunction (including the spin part and the coordinate part) with $S = 1/2$ and $S_z = +1/2$ must be written as $\psi_A(\mathbf{r}_1, \mathbf{r}_2, \mathbf{r}_3)\,|1/2, +1/2\rangle_S + \psi_S(\mathbf{r}_1, \mathbf{r}_2, \mathbf{r}_3)\,|1/2, +1/2\rangle_A$ such that the linear combination is totally antisymmetric with respect to the simultaneous interchanges of the coordinates and spins. The resulting transformation rules are

$$\psi_{MA}(\mathbf{r}_1, \mathbf{r}_2, \mathbf{r}_3) = -\psi_{MA}(\mathbf{r}_2, \mathbf{r}_1, \mathbf{r}_3) = \frac{1}{2}\psi_{MA}(\mathbf{r}_3, \mathbf{r}_2, \mathbf{r}_1) - \frac{\sqrt{3}}{2}\psi_{MS}(\mathbf{r}_3, \mathbf{r}_2, \mathbf{r}_1) = \frac{1}{2}\psi_{MA}(\mathbf{r}_1, \mathbf{r}_3, \mathbf{r}_2) + \frac{\sqrt{3}}{2}\psi_{MS}(\mathbf{r}_1, \mathbf{r}_3, \mathbf{r}_2),$$
$$\psi_{MS}(\mathbf{r}_1, \mathbf{r}_2, \mathbf{r}_3) = \psi_{MS}(\mathbf{r}_2, \mathbf{r}_1, \mathbf{r}_3) = -\frac{\sqrt{3}}{2}\psi_{MA}(\mathbf{r}_3, \mathbf{r}_2, \mathbf{r}_1) - \frac{1}{2}\psi_{MS}(\mathbf{r}_3, \mathbf{r}_2, \mathbf{r}_1) = \frac{\sqrt{3}}{2}\psi_{MA}(\mathbf{r}_1, \mathbf{r}_3, \mathbf{r}_2) - \frac{1}{2}\psi_{MS}(\mathbf{r}_1, \mathbf{r}_3, \mathbf{r}_2).$$

Note that ψ_A is anti-symmetric under interchanging the first two variables and ψ_S is symmetric. These two states are orthogonal and degenerate. Neither ψ_A nor ψ_S is completely symmetric or anti-symmetric under interchanging particles, only the *degenerate subspace* spanned by $\{\psi_A, \psi_S\}$ is invariant. When solving for the eigenstates of a three-particle system, it is necessary to maintain the subspace spanned by $\{\psi_A, \psi_S\}$ in order to fully exploit the permutation symmetries.

For a system of four spin-1/2 fermions, the quantum number of the total spin $S = 0, 1, 2$. We consider in the following the fully polarized state $S = 2$ and the unpolarized state $S = 0$

only. The spin polarized state $\psi(1234) = \psi_A(1234) \otimes |\uparrow\uparrow\uparrow\uparrow\rangle$ has a totally symmetric spin part and a antisymmetric spatial part $\psi_A(1234)$. On the other hand, there are two linearly independent spin states with zero total spin $S = 0$ corresponding to unpolarized states:

$$\chi_{MS} \propto |\uparrow\uparrow\downarrow\downarrow\rangle + |\downarrow\downarrow\uparrow\uparrow\rangle - \frac{1}{2}[|\uparrow\downarrow\rangle + |\downarrow\uparrow\rangle] \otimes [|\uparrow\downarrow\rangle + |\downarrow\uparrow\rangle],$$
$$\chi_{MA} \propto [|\uparrow\downarrow\rangle - |\downarrow\uparrow\rangle] \otimes [|\uparrow\downarrow\rangle - |\downarrow\uparrow\rangle].$$

The wave function is a linear combination of the above two states $\psi(1234) = \psi_{MA} \otimes \chi_{MS} + \psi_{MS} \otimes \chi_{MA}$. The symmetries of ψ_{MS} and ψ_{MS} in coordinate-space are determined by the total antisymmetry of the completewave function including spins and coordinates:

$$\begin{pmatrix} \psi_S \\ \psi_A \end{pmatrix} \to \hat{U}(P) \begin{pmatrix} \psi_S \\ \psi_A \end{pmatrix}, \tag{4.23}$$

where the 2×2 matrix U for each permutation P are given by

$$U(1234) = U(2143) = U(3412) = U(4321) = \begin{pmatrix} 1 & 0 \\ 0 & 1 \end{pmatrix},$$
$$U(2134) = U(1243) = U(3421) = U(4312) = \begin{pmatrix} 1 & 0 \\ 0 & -1 \end{pmatrix},$$
$$U(3214) = U(2341) = U(1432) = U(4123) = \begin{pmatrix} -\frac{1}{2} & \frac{\sqrt{3}}{2} \\ \frac{\sqrt{3}}{2} & \frac{1}{2} \end{pmatrix},$$
$$U(2314) = U(3241) = U(1423) = U(4132) = \begin{pmatrix} -\frac{1}{2} & -\frac{\sqrt{3}}{2} \\ \frac{\sqrt{3}}{2} & -\frac{1}{2} \end{pmatrix},$$
$$U(4231) = U(2413) = U(3142) = U(1324) = \begin{pmatrix} -\frac{1}{2} & -\frac{\sqrt{3}}{2} \\ -\frac{\sqrt{3}}{2} & \frac{1}{2} \end{pmatrix},$$
$$U(2431) = U(4213) = U(3124) = U(1342) = \begin{pmatrix} -\frac{1}{2} & \frac{\sqrt{3}}{2} \\ -\frac{\sqrt{3}}{2} & -\frac{1}{2} \end{pmatrix}.$$

The above rules reduce to, in the special case of any pair of particles occupying the same

position, the following relations (including the expected nodes of ψ_A)

$$\begin{aligned}
&\psi_A = 0, \text{ if } \mathbf{r}_1 = \mathbf{r}_2 \text{ or } \mathbf{r}_3 = \mathbf{r}_4, \\
&\psi_A = \sqrt{3}\psi_S, \text{ if } \mathbf{r}_1 = \mathbf{r}_3 \text{ or } \mathbf{r}_2 = \mathbf{r}_4, \\
&\psi_A = -\sqrt{3}\psi_S, \text{ if } \mathbf{r}_1 = \mathbf{r}_4 \text{ or } \mathbf{r}_2 = \mathbf{r}_3.
\end{aligned} \tag{4.24}$$

In general, for a system of $N = N_\uparrow + N_\downarrow$ spin-1/2 fermions in an $S_z = (N_\uparrow - N_\downarrow)/2$ state, the wavefunction can be decomposed in terms of its spin components as

$$\Psi = \sum_{i=1}^{\frac{N!}{N_\uparrow! N_\downarrow!}} F_i(\mathbf{r}_1, \cdots, \mathbf{r}_N)|\xi_i\rangle = \mathcal{A}\{F_1(\mathbf{r}_1, \cdots, \mathbf{r}_N)|\xi_1\rangle\}, \tag{4.25}$$

where

$$|\xi_1\rangle = |\underbrace{\uparrow \cdots \uparrow}_{N_\uparrow}\underbrace{\downarrow \cdots \downarrow}_{N_\downarrow}\rangle. \tag{4.26}$$

It follows from the antisymmetry of Ψ under the interchange of particles that each spatial part F_i is antisymmetric under the interchange of like-spin particles and that the F_i are all the same except for a relabeling of the particle indices and a change in sign for odd permutations. The full set of permutation symmetries require that the wavefunction Ψ to be an eigenstate of $\hat{S}^2$ and $\hat{S}_z$. In Eq.(4.25), we employed $N_\uparrow$ spin-up functions and $N_\downarrow$ spin-down functions in construction of the spin functions, and consequently Ψ is an eigenfunction of S_z . It is also an eigenstate of S^2 if the functions F_i satisfy certain linear relations. The total spin opterator $\hat{S}^2$ can be written in terms of lowering and raising operators of single-particle spin operators

$$\hat{S}^2 = \hat{S}_z^2 - \hat{S}_z + \hat{S}^+\hat{S}^- = \hat{S}_z^2 - \hat{S}_z + \sum_{i=1}^{N} \hat{s}_i^+ \hat{s}_i^- + \sum_{i \neq j=1}^{N} \hat{s}_i^+ \hat{s}_j^-. \tag{4.27}$$

Hence the matrix elements of $\hat{S}^2$ in the basis of $\{\xi_i\}$ are[2]

$$\langle\xi_i|\hat{S}^2|\xi_j\rangle = \begin{cases} S_z^2 - S_z + N_\uparrow, & i = j; \\ 1, & \text{if } \xi_i \text{ and } \xi_j \text{ are related by a single exchange of a } \uparrow\downarrow \text{ pair;} \\ 0, & \text{otherwise.} \end{cases} \tag{4.28}$$

The eigenvalue equation $\hat{S}^2\Psi = S(S+1)\Psi$ gives the linear dependencies among F_i

$$S(S+1)F_i = \sum_j \langle\xi_i|\hat{S}^2|\xi_j\rangle F_j, \quad \forall i. \tag{4.29}$$

In particular, for example, $N_\uparrow = N_\downarrow = 2$, we write

$$\Psi = F_1|\uparrow\uparrow\downarrow\downarrow\rangle + F_2|\uparrow\downarrow\uparrow\downarrow\rangle + F_3|\uparrow\downarrow\downarrow\uparrow\rangle + F_4|\downarrow\uparrow\uparrow\downarrow\rangle + F_5|\downarrow\uparrow\downarrow\uparrow\rangle + F_6|\downarrow\downarrow\uparrow\uparrow\rangle \tag{4.30}$$

and $\hat{S}^2\Psi = S(S+1)\Psi$ gives $\sum_{i=1}^{6} F_i = 0$.

4.3 Real Space Grid Basis

Mapping the hyperdimensional coordinates of a many-particle system on grid into an integer variable is useful for the numerical implementation of exact diagonalization techniques. By putting the system on a cubic lattice with n points in each direction, we label each Cartesian coordinate by an integer. For example, $x = i\Delta$ where Δ denotes the grid spacing in the x-direction. In a D-dimensional space, the position of a single particle $\mathbf{r} \equiv (x_1, \cdots, x_D)$ can be labeled by a set of integers $(i_1, \cdots, i_D)$ and then mapped onto an integer, for example,

$$I = i_1 + i_2 n + i_3 n^2 + \cdots + i_D n^{D-1}. \tag{4.31}$$

If the space domain is restricted to a D-dimensional wedge $\{\mathbf{r} \mid x_1 \leq x_2 \leq \cdots \leq x_D\}$, the position of a single particle in the reduced domain can be labeled by a set of integers

$(i_1 \leq i_2 \leq \cdots \leq i_D)$ and mapped onto an integer in the following way

$$I = i_1 + \frac{i_2(i_2+1)}{2!} + \frac{i_3(i_3+1)(i_3+2)}{3!} + \cdots + \frac{i_D(i_D+1)\cdots(i_D+D-1)}{D!}. \tag{4.32}$$

The configuration of an N-particle system can then be labeled by a set of intergers $(I_1, \cdots, I_N)$ and then mapped onto a single integer

$$\mathcal{I} = I_1 + I_2 n^D + I_3 n^{2D} + \cdots + I_N n^{(N-1)D}. \tag{4.33}$$

The collection of $\mathcal{I}$ forms the *complete domain* of the configuration space. The many-particle wavefunction $\Psi(\mathbf{r}_1, \cdots, \mathbf{r}_N)$ can be expressed and stored as an array $\Psi_{\mathcal{I}}$. The external potential and interaction potential $\sum_i U(\mathbf{r}_i) + \sum_{i<j} V(\mathbf{r}_{ij})$ are also directly expressed and stored as an array $U_{\mathcal{I}} + V_{\mathcal{I}}$. The kinetic energy, on the other hand, can be approximated by discrete Laplacian operators. A finite-difference expression for the Laplacian operator in one dimension is

$$-\nabla^2 \psi_i = \frac{1}{\Delta^2} \sum_{j=-n/2}^{n/2} c_j \psi_{i+j}, \tag{4.34}$$

where the coefficients c_j are obtained through the Fourier expansion of the eigenvalues of the Laplacian

$$k^2 = c_0 + 2 \sum_{j=1}^{n/2} c_j \cos(kj) \tag{4.35}$$

and are given in Table I of Ref.[3]. This expression also gives the single particle dispersion relation ϵ_k in one dimension. In general, the kinetic energy operator acting on the many-particle wavefunction at a particular grid point produces a weighted linear combination of the wavefunction values on the neighboring grid points

$$-\nabla^2 \Psi_{\mathcal{I}} = \frac{1}{\Delta^2} \sum_{\mathcal{J}} c_{\mathcal{I}\mathcal{J}} \Psi_{\mathcal{J}}, \tag{4.36}$$

where the summation is taken over the set of neighboring grid points of $\mathcal{I}$. Commonly used discrete Laplacian operators are the Hubbard model with nearest neighbor hopping and

long range hopping models including up to the next nearest neighbors. In grid basis, the Hamiltonian operator acting on a wavefunction can be written as

$$\hat{H}\Psi_{\mathcal{I}} = (U_{\mathcal{I}} + V_{\mathcal{I}})\Psi_{\mathcal{I}} + \frac{\hbar^2}{2m\Delta^2}\sum_{\mathcal{J}} c_{\mathcal{I}\mathcal{J}}\Psi_{\mathcal{J}}. \tag{4.37}$$

In real space grid basis, the $\mathcal{I}$'th basis function is chosen to be $\Psi_{\mathcal{J}}^{(\mathcal{I})} = \delta_{\mathcal{I}\mathcal{J}}$. In matrix notation,

$$H_{\mathcal{I}\mathcal{J}} = (U_{\mathcal{I}} + V_{\mathcal{I}})\delta_{\mathcal{I}\mathcal{J}} + \frac{\hbar^2}{2m\Delta^2}c_{\mathcal{I}\mathcal{J}}. \tag{4.38}$$

The external and interaction potential part is diagonal and the kinetic energy part has off-diagonal elements.

4.4 Symmetry Reduction of Grid and Wavefunctions

Given a group of g symmetry transformations $\mathbf{G} \equiv \{G_1, \cdots G_g\}$ (including identity $\mathbf{1}$) which leaves the Hamiltonian operator invariant, the application of all the symmetry transformations in group $\mathbf{G}$ on a particular hyperdimensional configuration grid point $\mathcal{I}$ produces a class of configuration grid points

$$\mathbf{G}\mathcal{I} \equiv \{G_1\mathcal{I}, \cdots, G_g\mathcal{I}\}. \tag{4.39}$$

which we call an *equivalent class* of point $\mathcal{I}$. According to the closure property of group $\mathbf{G}$, the equivalent class is invariant with respect to the symmetry group $\mathbf{G}$, namely, the application of $\mathbf{G}$ on any member of $\mathbf{G}\mathcal{I}$ yields the same set of grid points. By repeating the above procedure for every configuration grid point in the complete domain, the complete domain is decomposed into a series of subdomains $\{\mathcal{D}_1, \cdots, \mathcal{D}_m\}$, each consisting of grid points in the same equivalent class. The number of members M_i (called *multiplicity*) in a certain equivalent class (or subdomain) $\mathcal{D}_i$ is less than or equal to g because two different symmetry transformations G_1 and G_2 may map $\mathcal{I}$ onto the same point $G_1\mathcal{I} = G_2\mathcal{I}$. The total number of grid points in the complete domain is natually $\sum_{i=1}^{m} M_i$, where $M_i \leq g$, $\forall i$.

Depending on how the many-particle coordinates are encoded into integers, we are able to select one grid point, for example the one with the minimum integer label $\mathcal{I}'$, in each equivalent class as a *representative* grid point for the whole class. The collection of representative grid points forms the *reduced domain* and in principle, the Schrödinger equation can be solved in the reduced domain only. For example, The Schrödinger equation in the complete configuration grid reads

$$\hat{H}\Psi^{\alpha}_{\mathcal{I}} = E\psi^{\alpha}_{\mathcal{I}}, \quad \forall \mathcal{I} \in \text{Complete Domain}, \tag{4.40}$$

and the orthonormality takes the form $\sum_{\mathcal{I}} \Psi^{\alpha}_{\mathcal{I}}\Psi^{\beta}_{\mathcal{I}} = \delta_{\alpha\beta}$. If the wavefuction evaluation is restricted to the reduced domain

$$\hat{H}\Psi^{\alpha}_{i} = E\psi^{\alpha}_{i}, \quad \forall \mathcal{I} \in \text{Reduced Domain}, \tag{4.41}$$

whenever the value of the wavefunctions on a grid point outside the reduced domain is needed in the off-diagonal part of the Hamiltonian matrix, the exterior point is mapped back into the reduced domain by symmetry transformations. The orthonormality condition in the reduced domain is more complicated. In the simplest case where the wavefunctions flip signs upon symmetry transformations, the orthonormality condition can be written as

$$\sum_{i}{}' M_i \Psi^{\alpha}_{i}\Psi^{\beta}_{i} = \delta_{\alpha\beta}, \tag{4.42}$$

where the summation is taken over the reduced domain and the weight factor M_i is the multiplicity of the class. In the general case of an invariant subspace of degenerate wavefunctions, the form of the orthonormality condition in the reduced domain is prescribed the specific transformation rules of the wavefunctions in the given symmetry sector. For example, suppose $\{\psi^{\alpha}_{S}, \psi^{\alpha}_{A}\}$ are unpolarized states of a system of $N = 4$ spin-1/2 fermions with translational invariance and reflectional even-parity discussed in the previous section,

the orthonormality condition in the complete domain takes the form

$$\sum_i (\Psi_S^\alpha)_i (\Psi_S^\beta)_i = \sum_i (\Psi_A^\alpha)_i (\Psi_A^\beta)_i = \delta_{\alpha\beta}, \tag{4.43}$$

$$\sum_i (\Psi_S^\alpha)_i (\Psi_A^\beta)_i = \sum_i (\Psi_A^\alpha)_i (\Psi_S^\beta)_i = 0. \tag{4.44}$$

Note that there are two sets of orthogonal relations, within the invariant subspace $\{\Psi_S, \Psi_A\}$ and betweent he subspaces. In the reduced domain, the orthonormality relations are given by

$$\sum_i{}' \frac{M_i}{2} [(\Psi_S^\alpha)_i (\Psi_S^\beta)_i + (\Psi_A^\alpha)_i (\Psi_A^\beta)_i] = \delta_{\alpha\beta}. \tag{4.45}$$

In particular, within the invariant subspace the orthogonal relations are automatically satisfied by the transformation rules Eq.(4.23).

4.5 Iterative Diagonalization Methods

To determine the lowest several eigenvalues and the corresponding eigenstates, we start from a set of random trial states $|\psi_\alpha^0\rangle$ where $1 \le \alpha \le M$, and evolve the states $|\psi^{i+1}\rangle = G(\hat{H}, \tau)|\psi^i\rangle$, where the projection operator $G(\hat{H}, \tau)$ can take different forms. For example, the imaginary time evolution is

$$|\psi^{i+1}\rangle = e^{-\tau \hat{H}} |\psi^i\rangle. \tag{4.46}$$

This has the effect of suppressing the high-energy components. To perform the imaginary time evolution, consider the Trotter formula

$$e^{-\beta \hat{\mathcal{H}}_1} = \lim_{n\to\infty} \left(e^{-\frac{\beta}{n}\hat{T}} e^{-\frac{\beta}{n}\hat{U}} \right)^n. \tag{4.47}$$

In a coordinate representation, a single step of imaginary time τ can be written as:

$$\begin{aligned} \psi^{i+1}(\mathbf{R}) &= \int d^3\mathbf{R}' \langle \mathbf{R}| e^{-\tau \hat{\mathcal{H}}} |\mathbf{R}'\rangle \psi^i(\mathbf{R}') \\ &= \left(\frac{m}{2\pi\hbar\tau}\right)^{\frac{D}{2}} \times \int d^D\mathbf{R}' e^{-\frac{m}{2\hbar\tau}(\mathbf{R}'-\mathbf{R})^2} e^{-\frac{\tau U(\mathbf{R}')}{\hbar}} \psi^i(\mathbf{R}'), \end{aligned} \tag{4.48}$$

where $\mathbf{R} = \{\mathbf{r}_1, \cdots, \mathbf{r}_N\}$ denotes the hyperdimensional many-particle configuration. This integral is a convolution, and can be efficiently evaluated by Fast Fourier Transform

$$\psi^{i+1}(\mathbf{R}) = \mathrm{FFT}\left[e^{-\frac{\tau\hbar\mathbf{K}^2}{2m}} f_{\mathbf{K}}\right], \tag{4.49}$$

where $f_{\mathbf{K}}$ is defined as an inverse-Fourier transform

$$f_{\mathbf{K}} = \mathrm{FFT}^{-1}\left[e^{-\frac{\tau U(\mathbf{R})}{\hbar}} \psi^i(\mathbf{r})\right]. \tag{4.50}$$

For a lattice system with a high energy cut-off $E_{\max}$, another form of $G(\hat{H}, \tau) = \mathbf{1} - \tau\hat{H}$ for short time step τ is more convenient to calculate projections in a reduced domain

$$|\psi^{i+1}\rangle = (\mathbf{1} - \tau\hat{H})|\psi^i\rangle, \tag{4.51}$$

where only successive applications of the Hamiltonian operator to the trial-states are needed to evaluate the projection. To suppress the higher energy components, the time step τ must be sufficiently small $\tau < 2\hbar/E_{\max}$.

At each step of the evolution, the state vectors are properly symmetrized and orthogonalized. As $i \to \infty$, the states converge to the lowest M eigenstates of the Hamiltonian $\hat{H}$ within a given symmetry sector. The errors are controlled and can be reduced arbitrarily with increasing the number of grid points or number of iterations. As discussed below, the computational cost grows rapidly with system size, but significant reduction can be achieved by invoking symmetries.

4.6 Comments on Particle-Number Basis

The second quantized form of a many-particle Hamiltonian operator is written in the particle-number basis. For example, the spin-1/2 Fermion Hubbard model

$$\hat{H} = -t \sum_{\langle ij\rangle,\sigma} \left(c^\dagger_{i\sigma} c_{j\sigma} + c^\dagger_{j\sigma} c_{i\sigma}\right) + U \sum_i n_{i\uparrow} n_{i\downarrow}, \tag{4.52}$$

describes a single band of electrons $n_{i\sigma} = c^{\dagger}_{i\sigma} c_{i\sigma}$ with on-site interaction U. In the language of second quantization, one needs to translate the many-particle Hamiltonian into a sparse Hermitian matrix. If we want to take into account symmetries of the problem, the construction of symmetric basis set is usually intellectually and technically challenging. Given a symmetry of the system, i.e. an operator that commutes with $\hat{H}$, the Hamiltonian will not mix states from different eigenspaces of the symmetry operator. Therefore, the matrix representation of $\hat{H}$ will acquire a block structure, and each block can be handled separately. The Hubbard Hamiltonian Eq.(4.52) has the following symmetries: translational invariance, inversion symmetries, conservation of the total number of particles, all components of the total spin and the particle-hole symmetry for a bipartite lattice[4]. For the task of basis construction the most important of these symmetries are the translational invariance, the particle number conservation and the spin-S^z conservation. As in real space grid basis, the total spin S^2 can also be fixsed in addition to S^z, but the construction of the corresponding eigenstates is too complicated for most practical computations.

In comparison with the real space grid basis described in the previous section, the second quantized form in the particle-number basis has the advantage that the permutation symmetries are incorporated into the basis construction and no explicit antisymmetrization is needed. The challenging part of the project is to construct the basis states satisfying the given symmetries. On the other hand, if the problem is formulated in the real space grid basis, each grid point in the reduced domain is a basis function and the explicit construction of symmetric basis states is no longer required. The mapping rules from the complete domain to the reduced doman and the construction of a neighbor list is the challenging part.

References

[1] I. G. Kaplan. *Symmetry of Many-electron Systems.* Academic Press Inc, first edition, 1975.

[2] Chien-Jung Huang, Claudia Filippi, and C. J. Umrigar. Spin contamination in quantum monte carlo wave functions. *The Journal of Chemical Physics*, 108(21):8838–8847, 1998.

[3] James R. Chelikowsky, N. Troullier, K. Wu, and Y. Saad. Higher-order finite-difference

pseudopotential method: An application to diatomic molecules. *Phys. Rev. B*, 50:11355–11364, Oct 1994.

[4] Alexander Weiβe (Editor) Holger Fehske (Editor), Ralf Schneider (Editor). *Computational Many-Particle Physics (Lecture Notes in Physics)*. Springer, first edition, 2010.

Chapter 5

Pairing and Ferromagnetic Instabilities of Spin-1/2 Fermions

5.1 BCS-BEC crossover and unitarity limit

Consider a two-component atomic Fermion gas occupying two different spin states, for simplicity, called spin up ($\sigma =\uparrow$) and spin down ($\sigma =\downarrow$). The many-body Hamiltonian for a system of N interacting particles moving in an external potential has the form Eq. (4.1) in Chapter 4:

$$\hat{H}_N = \sum_{i=1}^{N} \left[\frac{\mathbf{p}_i^2}{2m} + U(\mathbf{r}_i) \right] + \sum_{i<j=1}^{N} V(\mathbf{r}_i, \mathbf{r}_j), \tag{5.1}$$

where the interatomic potential can be modeled as a regularized δ-function:

$$V(\mathbf{r}, \mathbf{r}') = \frac{4\pi\hbar^2 a}{m} \delta(\mathbf{r} - \mathbf{r}') \frac{\partial}{\partial |\mathbf{r} - \mathbf{r}'|} |\mathbf{r} - \mathbf{r}'|, \tag{5.2}$$

where a is the zero-energy scattering length and m is the mass. As already discussed in Chapter 2, the effect of the zero-range pseudopotential Eq. (5.2) is accounted for by the Bethe-Peierls boundary condition Eq. (2.53). There are several important cases in which the many-body probem for the interacting spin-1/2 Fermion gases are particularly interesting [1]: (1) the BCS limit; (2) the BEC limit; (3) the unitary limit; (4) the weakly repulsive gas with no molecules forming; (5) the instability toward a ferromagnetic phase, as shown in Fig. (5.1) where two energy branches are plotted as functions of the inverse scattering length $(k_F a)^{-1}$. In this section, we will be considering the homogeneous system in the absence of an external potential $U(\mathbf{r}) = 0$.

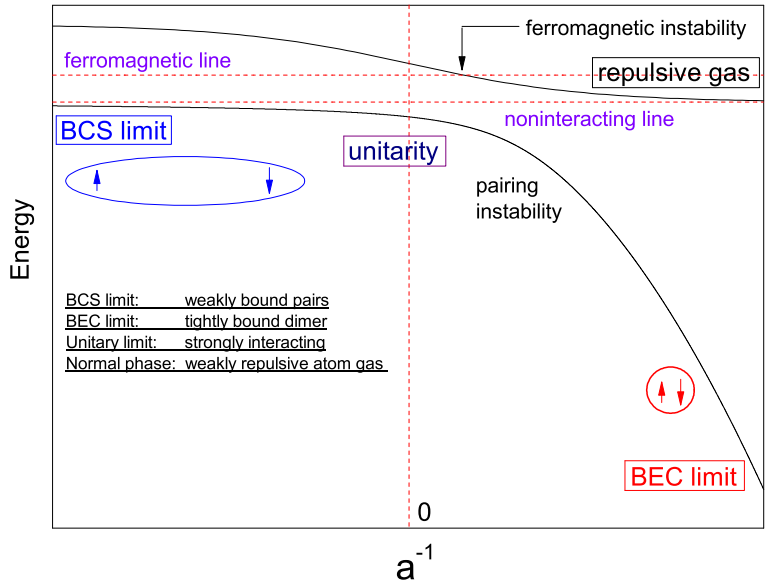

Figure 5.1: A sketch of the two interesting energy branches of the spin-1/2 fermion gas as functions of the inverse scattering length $(k_F a)^{-1}$: the ground state energy and the upper-branch scattering state with no molecules forming.

5.1.1 Gas in normal state

A first example is the dilute gas in its *normal state*, for which standard perturbation theory can be applied with the small parameter $k_F|a| \ll 1$ expressing the diluteness condition of the gas. At zero temperature, the expansion of the energy per particle up to quadratic terms in the dimensionless parameter $k_F a$ yields the following expression [2][3]

$$\frac{E_{\text{normal}}}{N} = \frac{3}{5}\epsilon_F \left[1 + \frac{10}{9\pi}k_F a + \frac{4(11-2\ln 2)}{21\pi^2}(k_F a)^2 + \cdots\right] \tag{5.3}$$

in terms of the Fermi energy $\epsilon_F = k_B T_F = \hbar^2(2\pi^2 n)^{2/3}/(2m)$ of the non-interacting gas. Although the above result was first derived with the aid of the δ-function pseudopotential [2][3], it is universal as it holds for any interatomic potential with a sufficiently small effective range. Higher-order terms in Eq. (5.3) will depend not only on the scattering length a, but also on the details of the potential. The above result is the true ground state energy only in the case of purely repulsive potentials, such as the hard-sphere model. For more realistic potentials with an attractive tail or the regularized-δ function potential, the above result

describes the metastable gas-like state of repulsive atoms.

5.1.2 Weakly attractive gas

The dilute Fermion gas interacting with negative scattering length $k_F|a| \ll 1$ corresponds to the famous BCS picture first introduced to describe the phenomenon of superconductivity [4]. In this limit, the many-body problem can be solved both at zero temperature and non-zero temperature. The main physical feature is the instability of the system in the presence of even an infinitesimally weak attraction and the formation of bound states, the Cooper pairs. Exact results are available for the critical temperature [5]

$$T_c = \left(\frac{2}{e}\right)^{7/3} \left(\frac{\gamma}{\pi}\right) T_F e^{\frac{\pi}{2k_F a}} \approx 0.28 T_F e^{\frac{\pi}{2k_F a}}, \tag{5.4}$$

where $\gamma = 1.781072381$ is the exponential of Euler's constant. The energy gap Δ_{gap} at zero temperature in the spectrum of single-particle excitations $\epsilon_k = \sqrt{\Delta_{\text{gap}}^2 + [\hbar^2 k_F(k - k_F)]^2/m^2}$ close to the Fermi surface $|k - k_F| \ll k_F$ is related to T_c through $\Delta_{\text{gap}} = (\pi/\gamma) k_B T_c \approx 1.76 k_B T_c$. Furthermore, the ground-state energy per particle takes the form

$$\frac{E_{\text{BCS}}}{N} = \frac{E_{\text{normal}}}{N} - \frac{3\Delta_{\text{gap}}^2}{8\epsilon_F}, \tag{5.5}$$

where E_{normal} is the perturbation expansion with $a < 0$ and the second term corresponds to the exponentially small energy gain of the superfluid compared to the normal state.

5.1.3 Gas of composite bosons

The positive value of the scattering length is associated with the emergence of a two-body bound state and the formation of dimers as discussed in Sect. (2.3) in Chapter 2. The size of the dimer is on the order of the scattering length a and their binding energy is $\epsilon_b = -\hbar^2/ma^2$. These dimers composed of two fermions are bosonic in nature, and if the gas is sufficiently dilute and cold, can give rise to Bose-Einstein condensation (BEC). Petrov *et al.* [6] solved the four-body problem of collisions between two dimers. Using the zero-range δ-function

pseudopotential, they calculated the dimer-dimer scattering length

$$a_{\rm dd} \cong 0.6a. \tag{5.6}$$

Including the interactions between molecules, the behavior of the dilute ($k_F a \ll 1$) gas of dimers, called the BEC limit, is described by the equation of state

$$\frac{E_{\rm BEC}}{N} = \frac{\epsilon_b}{2} + \frac{k_F a_{\rm dd}}{6\pi}\left[1 + \frac{128}{15\sqrt{6\pi^3}}(k_F a_{\rm dd})^{3/2} + \cdots\right]\epsilon_F. \tag{5.7}$$

The gas of dimers and the repulsive gas of atoms represent two different branches of the many-body problem, both corresponding to positive scattering length. If one stays sufficiently away from the resonance $a = \pm\infty$, losses are not dramatic and the many-body state is a repulsive Fermion gas. Conversely, the gas of dimers is realized by crossing adiabatically the resonance starting from negative values of a.

5.1.4 Gas at unitarity

The results for the three phases considered above are established in the limiting cases $k_F|a| \to 0$. A more difficult problem concerns with the behavior when $k_F|a| \gtrsim 1$, i.e. when the scattering length becomes larger than the interparticle spacing. This corresponds to a gas that is dilute and strongly interacting at the same time. An exact solution of the many-body problem for $k_F|a| \gtrsim 1$ is not available. However, approximate schemes and numerical methods indicate that the gas is stable. The limit $k_F|a| \to \infty$ is called the *unitary* regime because it is characterized by the universal behavior of the scattering amplitude $f(k) = i/k$, the maximum magnitude allowed by the unitarity of the scattering S-matrix. As the scattering length disappears from the problem, the only remaining relevant length scale is the Fermi wave vector (and the de broglie thermal wavelength at non-zero temperature). An important example of this universal behavior is given by the energy ratio

$$\xi_{N_\uparrow N_\downarrow} \equiv \frac{E^{\rm unitary}_{N_\uparrow N_\downarrow}}{E^0_{N_\uparrow N_\downarrow}}, \tag{5.8}$$

where E^0 is the energy for the non-interacting system. The universal parameter ξ is defined as the thermodynamic limit for the spin-unpolarized system

$$\xi = \lim_{N\to\infty} \xi_{N,N}. \tag{5.9}$$

A recent QMC calculation [7] found that the energy of the Fermi gas at unitarity and zero effective range is $\xi = 0.372(0.005)$ using a variety of interactions tuned to unitarity.

There is not at present an exact analytic solution of the many-body problem along the whole BCS-BEC crossover. A useful approximation is provided by the standard BCS mean-field theory of superconductivity. This approach, first introduced by Eagles(1969) [8] and Leggett(1980) [9], provides a comprehensive and qualitatively correct picture of BCS-BEC crossover at zero temperature.

5.2 Itinerant ferromagnetism: Heisenberg, Bloch and Stoner

Itinerant ferromagnetism refers to the magnetic state created by the same electrons with aligned spins as the ones responsible for conduction. Heisenberg [10] first recognized *exchange interactions* between electrons residing in atomic orbitals that overlap spatially could favor a spin-aligned state. Exchange interactions appear indirectly as a result of spin-independent Coulomb interactions combined with Pauli exclusion principle. Consider, for example, a simplified model of hydrogen molecule by taking the nuclei fixed and their spins ignored. The two electrons may be described by their positions $\mathbf{r}_1$ and $\mathbf{r}_2$ and some components of their spins $\mathbf{S}_1$ and $\mathbf{S}_2$. If ψ_a and ψ_b are eigenstates for a single electron with energies E_a and E_b, then

$$\psi_{ab}(\mathbf{r}_1, \mathbf{r}_2) = \psi_a(\mathbf{r}_1)\psi_b(\mathbf{r}_2) \tag{5.10}$$

has energy $E_a + E_b$, neglecting mutual interactions between the electrons. The state

$$\psi_{ba}(\mathbf{r}_1, \mathbf{r}_2) = \psi_b(\mathbf{r}_1)\psi_a(\mathbf{r}_2) \tag{5.11}$$

has the same energy. If we add a mutual interaction $V(\mathbf{r}_1, \mathbf{r}_2) = V(\mathbf{r}_2, \mathbf{r}_1)$ which is spin-independent between the electrons, then the two-electron eigenstates become

$$\psi_S = \frac{1}{\sqrt{2}}(\psi_{ab} + \psi_{ba}), \quad \psi_A = \frac{1}{\sqrt{2}}(\psi_{ab} - \psi_{ba}) \tag{5.12}$$

with their respective energies

$$E_S = E_a + E_b + I - J, \quad E_A = E_a + E_b + I + J, \tag{5.13}$$

where

$$I = \int \psi^*_{ab} V \psi_{ab} d^3\mathbf{r}_1 d^3\mathbf{r}_2, \quad J = \int \psi^*_{ab} V \psi_{ba} d^3\mathbf{r}_1 d^3\mathbf{r}_2. \tag{5.14}$$

The spatial wave functions must be multiplied by spinors to describe the spins of electrons, and the total wave function must be antisymmetric under the simultaneous exchanges of coordinates and spins. For two spin-$\frac{1}{2}$ particles, the symmetric spin states have total spin-1, and the anti-symmetric states have spin-0. Thus total wave functions have the form

$$\Psi_S = \psi_S \chi^{(0)}, \quad \Psi_A = \psi_A \chi^{(1)}, \tag{5.15}$$

where $\chi^{(S)}$ is any two-electron spin state with total spin S. Note that the interaction potential V is spin-independent so that the energy eigenstates are also eigenstates of the total spin, we can then write the energy in terms of the spin as follows. If $\mathbf{S}$ is the total spin, $\mathbf{S} \cdot \mathbf{S}$ has eigenvalues $S(S+1) = 0$ and 2. The energy of a state with total spin S can be written in the form

$$E = E_S + (E_A - E_S) \cdot \frac{S(S+1)}{2}. \tag{5.16}$$

Therefore we can write the mutual interaction Hamiltonian for the system in the form

$$\mathcal{H} = E_S + (E_A - E_S)\frac{\mathbf{S} \cdot \mathbf{S}}{2} = E_a + E_b + I + \frac{1}{2}J + 2J\mathbf{S}_1 \cdot \mathbf{S}_2. \tag{5.17}$$

The splitting term, described by $\Delta\mathcal{H} = 2J\mathbf{S}_1 \cdot \mathbf{S}_2$ is proportional to the exchange integral J which depends on how much the wave functions ψ_a and ψ_b overlap. We have thus taken a spin-independent Hamiltonian of two interacting electrons and made it look like a spin-spin interaction. Note that for higher spins we would get a polynomial in $\mathbf{S}_1 \cdot \mathbf{S}_2$ if we went through a similar procedure.

Bloch [11] extended Heisenberg's idea to delocalized electrons in what is now known as itinerant exchange, and showed that at high density the electron system would be paramagnetic in order to optimize the kinetic energy cost whereas at low density the system should spontaneously spin-polarize itself into a ferromagnetic ground state in order to optimize the exchange energy. In Bloch's analysis, one writes the total Hartree-Fock energy per-particle as a sum of the noninteracting kinetic energy and the Fock exchange energy due to unscreened Coulomb interaction (e^2/r) as

$$\begin{aligned} \frac{E}{N} &= \frac{3}{10}\epsilon_F\left[(1+\eta)^{\frac{5}{3}} + (1-\eta)^{\frac{5}{3}}\right] - \frac{3e^2}{8\pi}k_F\left[(1+\eta)^{\frac{4}{3}} + (1-\eta)^{\frac{4}{3}}\right] \\ \left(\text{in units of } \frac{e^2}{2a_B}\right) &= \frac{1.1}{r_s^2}\left[(1+\eta)^{\frac{5}{3}} + (1-\eta)^{\frac{5}{3}}\right] - \frac{0.46}{r_s}\left[(1+\eta)^{\frac{4}{3}} + (1-\eta)^{\frac{4}{3}}\right], \quad (5.18) \end{aligned}$$

where $N = N_\uparrow + N_\downarrow$ is the total number of particles, $n = n_\uparrow + n_\downarrow$ is the total number density, $k_F = \sqrt[3]{3\pi^2 n}$ is the Fermi momentum when $N_\uparrow = N_\downarrow$ and ϵ_F is the corresponding Fermi energy, $\eta = \frac{n_\uparrow - n_\downarrow}{n_\uparrow + n_\downarrow}$ characterizes the magnetization, and r_s is the dimensionless average interparticle distance

$$\frac{4\pi}{3}\pi r_s^3 = \frac{1}{a_B^3 n}, \quad (5.19)$$

where $a_B = \hbar^2/m_e e^2$ is Bohr radius. The above Hartree-Fock energy expression leads to a first-order ferromagnetic transition at $r_s \cong 5.45\,(k_F a_B \cong 0.35)$, i.e. $E(\eta = 1)$ ferromagnetic state is lower in energy than $E(\eta = 0)$ paramagnetic state for $r_s > 5.45$. This is called Bloch ferromagnetism. However, the few systems that exhibit such low densities are not ferromagnetic. In real electron liquids, the exchange-only Hartree-Fock approximation considered above for Bloch instability is inadequate because correlation effects are known to be important and must be included in the energetic considerations. In fact, precise

Monte Carlo calculations suggest [12] that the transition to a ferromagnetic state appears at $r_s \cong 50\,(k_F a_B \cong 0.04)$, about one order of magnitude lower than the simple Hartree-Fock estimate that Bloch used.

Stoner [13] introduced the concept of exchange field that can be viewed as a fluctuating spin environment acting on a single electron. The simplest version of the model is to consider a zero-range δ-function-like, spin-independent potential between electrons, leading to

$$\frac{E}{N} = \epsilon_F \left\{ \frac{3}{10} \left[(1+\eta)^{\frac{5}{3}} + (1-\eta)^{\frac{5}{3}} \right] + \frac{2}{3\pi} k_F a (1+\eta)(1-\eta) \right\}, \tag{5.20}$$

where a is the scattering length characterizing short-range interactions between two spin components. The Stoner instability is characterized by the divergence of the spin susceptibility and hence a second order continuous ferromagnetic phase transition. Note that for short range interaction, the s-wave scattering between fermions in the same spin(hyperfine) states is inhibited due to Pauli principle. It follows that at low temperature the dilute Fermi gas, in a fixed hyperfine state, is practically ideal. Nevertheless, the effect of interaction could be very effective for a Fermi gas with two or more components(hyperfine states). This model predicts itinerant ferromagnetism for sufficiently strong repulsion or high density. The phase transition is continuous and occurs when the minimum in energy is at nonzero magnetization at $k_F a = \pi/2$.

5.3 Jo *et al.* experiment

Although a few early experiments conducted on the repulsive side of the resonance hinted at a ferromagnetic behavior, these investigations were hindered by the challenges posed by the cold atomic gas setup, with fixed relative populations of particles, trap confinement, atom loss through three-body interactions, and nonequilibrium physics, rendering the conclusive identification of ferromagnetism impossible. The control afforded by Feshbach resonance phenomena in ultracold atomic gases has enabled the exploration of strongly correlated degenerate Fermi systems. In a recent study of the possibility of itinerant ferromagnetism

[11, 13, 12, 14], Jo *et al.* [15] attempted to observe the physics behind the Stoner model in an atomic gas of ^{6}Li atoms. Evidence for ferromagnetic ordering was seen. To overcome the obstacle of atom loss through three body interactions, the experiment was carried out under marginally adiabatic conditions, with the atoms prepared in the disordered nonferromagnetic state and the magnetic field ramped to the repulsive side of the resonance in 4.5 ms and then held fixed for a further 2 ms. In this section, we briefly describe the preparation of the experiment.

5.3.1 Preparation of the ultracold ^{6}Li cloud

(1) The first step is the production of a spin-polarized Fermi gas prepared in the $|F, m_F\rangle = |3/2, 3/2\rangle$ hyperfine state by *sympathetic cooling* [16] with bosonic ^{23}Na atoms in a magnetic trap.

(2) The ^{6}Li cloud was then loaded into a deep optical dipole trap with a maximum power of 3W and radial trap frequency of ~ 3.0 kHz, followed by an RF transfer into the lowest hyperfine state $|F, m_F\rangle = |1/2, 1/2\rangle$, as shown in Fig. (1.1) in . Additional axial confinement was provided by magnetic fields. Note that the state $|F, m_F\rangle = |1/2, 1/2\rangle$ is a high-field seeker, thus cannot be magnetically trapped. That's why the ^{6}Li cloud has to be loaded into an optical trap before being transfered to the lowest hyperfine state.

(3) An *equal* mixture of $|1\rangle$ and $|2\rangle$ spin states (corresponding to the $|F, m_F\rangle = |1/2, +1/2\rangle$ and $|1/2, -1/2\rangle$ states at low magnetic field) was prepared by a Landau-Zener RF sweep at a magnetic field of 590 G, followed by 1 s for decoherence and further evaporative cooling at 300 G. Note that transitions between hyperfine states can be induced by radio frequency radiation, whose frequency ($\sim 10^9$ Hz) is of order the hyperfine splitting. The optical dipole trap is constructed from lasers with much higher frequency ($\sim 10^{14}$ Hz) which would not cause the pseudospin to flip.

(4) Finally, the optical trapping potential was adiabatically reduced over 600 ms, and the field increased back to 590 G. The trap had a depth of 7.1 μK and was nearly cigar shaped with frequencies $\nu_x = \nu_y \simeq 300$ Hz and $\nu_z \simeq 70$ Hz.

5.3.2 Temperature and effective temperature

Jo *et al.* experiment thus starts with an atom cloud consisting of an equal mixture of ^{6}Li atoms in the lowest two hyperfine states, held at 590 G in an optical dipole trap with additional magnetic confinement. The number of atoms per spin state is approximately 6.5×10^5, which corresponds to a Fermi temperature $T_F \sim 1.4\,\mu$K.

Unlike the situation in condensed matter systems, for ultracold gases, thermometry is less straightforward. Experimentally, temperature is determined from the spatial profiles of the cold gas, either in the trap, or following expansion. For weakly interacting Bose and Fermi gases, where the theoretical density is well understood, this procedure is straightforward. However, for a strongly interacting gas, the spatial profile has not been understood until recently [17][18]. For this reason, the temperature is often measured on either side far away from the Feshbach resonance, where the scattering length is small. A strongly interacting sample in the unitary regime is then prepared by an adiabatic change of the magnetic field.

The *effective temperature* T was determined immediately after the field ramp by fitting the spatial distribution of the cloud with a finite temperature Thomas-Fermi profile and could be varied between $T/T_F = 0.1$ and $T/T_F = 0.6$. Applying the procedure discussed in [19] to repulsive interactions, one can estimate that the real temperature $\tilde{T}$ is approximately 20% larger than the effective one. Denote k_F^0 as the Fermi wave vector of the noninteracting gas calculated at the trap center. The effective temperature did not depend on $k_F^0 a$ for $k_F^0 a < 6$. At higher temperatures, additional shot-to-shot noise was caused by large fluctuations in the atom number.

5.3.3 Tuning the repulsive interaction

From the starting point at 590 G, the magnetic field was increased toward the Feshbach resonance at 834 G, thus providing adjustable repulsive interactions. Because of the limited lifetime of the strongly interacting gas, it was necessary apply the fastest possible field ramp, limited to 4.5 ms by eddy currents. The ramp time is approximately equal to the inverse of the axial trap frequency ($\sim \nu_{xy}^{-1}$) and therefore only marginally adiabatic. Depending on the magnetic field during observation, either atoms or molecules were detected by absorption imaging [20].

5.3.4 Measurement of physical quantities

Several physical quantities are measured during observation to make comparison with the simple mean-field model of Stoner Hamiltonian as indirect evidences of a ferromagnetic phase transition. As we mentioned earlier, in contrast to electrons in solids, the number of atoms in each hyperfine states is conserved. As a result, the total magnetization always vanishes. In fact, ferromagnetic phase transition cannot occur in a uniform system. However, since the atomic gas is confined in a trap, the signature of ferromagnetism is the formation of domains that contain only atoms in one of the hyperfine states.

The emergence of local *spin polarization* is observed by the suppression of collisions, because the Pauli exclusion principle forbids collisions in a fully polarized cloud. The inelastic three-body collisions which convert atoms into molecules are monitored and the atom loss rate is derived in inelastic scattering theory

$$\Gamma = \Gamma_0(T)(k_F a)^6 \int d^3\mathbf{r} n_\uparrow(\mathbf{r}) n_\downarrow(\mathbf{r})[n_\uparrow(\mathbf{r}) + n_\downarrow(\mathbf{r})]. \tag{5.21}$$

The annihilation rate per atom is proportional to $\Gamma_0(T)(k_F a)^6 n_\uparrow n_\downarrow$ or $\Gamma_0(T)(k_F a)^6 n^2(1-\eta^2)$, where $\eta = (n_\uparrow - n_\downarrow)/(n_\uparrow + n_\downarrow)$. This rate can be observed by monitoring the initial drop in the number of atoms during the first 2 ms after the field ramp. The authors avoided longer observation times, because the increasing molecule fraction could modify the properties of the

sample. A sharp peak was observed in the atom loss rate around $k_F^0 a \cong 2.5$ at $T/T_F = 0.12$, which is the lowest temperature achieved in this experiment, indicating a transition in the sample to a state with local magnetization.

The *kinetic energy* of the cloud was determined by suddenly switching off the optical trap and the Feshbach fields immediately after the field ramp and then imaging state $|\uparrow\rangle$ atoms at zero field using the cycling transition after a ballistic expansion time of $\Delta t = 4.6$ ms. The kinetic energy was obtained from Gaussian radial width σ as $E_{\rm kin} = 3m\sigma^2/2\Delta t^2$, where m is the mass of the ^{6}Li atom. A minimum of the kinetic energy was observed at $k_F^0 a \cong 2.2$ for the coldest temperature $T/T_F = 0.12$, nearly coincide with the onset of local polarization. The peak in the atom loss rate occurs slightly later than the minimum of kinetic energy, probably because the factor a^6 in Eq.(5.21) increases with a.

The *cloud size* can be measured by imaging and a maximum was observed at the phase transition. The cloud size may not have fully equilibrated because the ramp time was only marginally adiabatic.

The suppression of the atom loss rate, the minimum in kinetic energy, and the maximum in cloud size show a strong temperature dependence between $T/T_F = 0.12$ and 0.22. The properties of a normal Fermi gas approaching the unitarity limit with $k_F^0 a \gg 1$ should be insensitive to temperature variations in this range; therefore, the observed temperature dependence provides further evidence for a transition to a new phase. At higher temperatures (e.g. $T/T_F = 0.39$), the observed nonmonotonic behavior becomes less pronounced and shifts to larger values of $k_F^0 a$ for $3 < k_F^0 a < 6$. For all three observed properties, a nonmonotonic behavior is no longer observed at $T/T_F = 0.55$. One interpretation is that at this temperature and above, there is no longer a phase transition. In a mean-field approximation, a ferromagnetic phase transition would appear at all temperatures but for increasing values of $k_F^0 a$. The experiment may imply that the interaction energy saturates around $k_F^0 a \approx 5$.

5.3.5 Molecular admixture

The authors claim that the only difference between the experiment and the ideal Stoner model is a molecular admixture of 25%. The molecular fraction was constant for $k_F^0 a > 1.8$ for all temperatures and therefore cannot be responsible for the sudden change of behavior of the gas at $k_F^0 a = 2.2$ at the coldest temperature $T/T_F = 0.12$. The measurements were repeated with molecular admixture of 60% and the minimum in the kinetic energy occurred at the same value of $k_F^0 a$ within experimental accuracy.

5.3.6 Ferromagnetic domain

The experiment was *unsuccessful* in imaging ferromagnetic domains using differential in situ phase contrast imaging. The signal-to-noise level is about 10 and there were at least 100 domains in a volume given by the spatial resolution of $\sim 3\,\mu$m and by the radial size of the cloud. This is a cylinder shaped region containing $\sim$ 50 spin-polarized atoms. The author suspect that the short lifetime prevented the domains from growing to a large size and eventually adopting the equilibrium texture of the ground state predicted to have spins pointing radially outward [21][22]. All measurements in this experiment are sensitive only to local spin polarization and are independent of domain structure and texture.

5.3.7 Lifetime of the atomic gas

The atomic Fermi gas in the spin-polarized ferromagnetic state should be ideally noninteracting and should not suffer from inelastic collisions. However, the typical lifetime were 10 to 20 ms, which were probably related to a small domain size and three body recombination at domain walls because atoms on different sides of the domain wall occupy different hyperfine states.

5.4 Review of Existing Calculations

Little attention has been given to the regime on the repulsive side of the Feshbach resonance, one possible reason is that this region is an excited branch which is unstable against near-resonant three body recombination into weakly bound molecules. Nevertheless, many efforts have been made to improve the simple mean-field model of Stoner before Jo *et al.* experiment [15]. Fermi quantum degeneracy first realized experimentally in late 1999 [23][24] renewed the theoretical study to identify a two-component Fermi gas near a Feshbach resonance as a model system for itinerant ferromagnetism, assuming that the decay into molecules can be sufficiently suppressed.

5.4.1 Early considerations in 1997

Houbiers *et al.* work [25] investigated the superfluid state of spin-polarized aotmic ^{6}Li confined in a magnetic trap. This work put its emphasis on the critical temperature of the superfluid phase transition, which is on the BCS (attractive) side of Feshbach resonance. The authors considered the mechanical stability of both negative and positive scattering length, which represents one of the earliest attempts to deal with both attractive and repulsive interatomic interactions in a two-component Fermi gas.

5.4.2 Mean field theory and LDA

Soon after the first experiment that achieved Fermi quantum degeneracy, theorists started to consider density profiles and spin textures for Fermi vapors in trap. One of the major approaches is to take into account the interatomic repulsion in the framework of mean field theory and to use *local density approximation* (LDA) to deal with inhomogeneity in trap. The energy functional in LDA is typically written as

$$E\left\{[\rho_\sigma(\mathbf{R})]\right\} = \int d^3\mathbf{R}\left[\frac{3}{5}\alpha\sum_\sigma \rho_\sigma^{5/3}(\mathbf{R}) + \sum_{\sigma,\sigma'} g_{\sigma\sigma'}\rho_\uparrow(\mathbf{R})\rho_\downarrow(\mathbf{R}) + U(\mathbf{R})\sum_\sigma \rho_\sigma(\mathbf{R}) - \sum_\sigma \mu_\sigma\rho_\sigma(\mathbf{R})\right], \tag{5.22}$$

where $U(\mathbf{R})$ denotes the external trap potential, ρ_σ denotes the density profile of spin species σ, $\alpha = (6\pi^2)^{2/3}\hbar^2/2m$ and $g = 4\pi a_s^{\sigma\sigma'}\hbar^2/m$.

Salasnich *et al.* [26] studied the thermodynamical properties of a M-component Fermi vapors confined in a harmonic external potentials, paying particular attentions to the *density profiles* within semiclassical approximation in the conditions of experiments [23][24] with ^{40}K at that time. It is shown that in calculating density profiles the semiclassical approximation is good for $k_BT/\hbar\omega \gg 1$ where ω is the trap frequency, or at a fixed temperature, for a large number of N of trapped particles. The authors considered a dilute Fermi vapor with M hyperfine states within the mean field approach and semiclassical approximation. The spatial density profile $n_i(r)$ of the ith component of a Fermi vapor is written as $n_\sigma = \lambda^{-3/2} f_{3/2}\left(e^{\beta\left[\mu_\sigma - U(r) - \sum_{\sigma'}^{M} g_{\sigma\sigma'} n_{\sigma'}(r)\right]}\right)$ where $i = 1, 2, \cdots, M$, λ is de Broglie wavelength and $f_{3/2}(x)$ is the Sommerfeld function. Thus, the effect of the other $M-1$ Fermi components on the ith component is the appearance of a mean field effective potential. At zero temperature the kinetic energy assumes the familiar Thomas-Fermi form. Equations (5.22) was then solved numerically with a self-consistent iterative procedure. If the components of the Fermi vapor are non-interacting, they can occupy the same spatial region. Instead, if the repulsive interaction is strong enough or for particle number N very large one finds a phase separation, i.e. the Fermi components stay in different spatial regions. The authors did not try to locate the ferromagnetic transition point in this work.

Sogo and Yabu [27] first explicitly analyzed the collective ferromagnetism in a trapped two-component Fermi-degenerate gas $\rho_\sigma = [\rho_\uparrow, \rho_\downarrow]$ in the framework of local density approximation at zero temperature. Because zero-range interactions can be neglected between Fermions with unlike spins, we have a single interaction parameter $g = 4\pi\hbar^2 a_{\uparrow\downarrow}/m$. The Thomas-Fermi equations for the densities ρ_σ are derived from the variations of the total energy E on ρ_σ with a constraint on the total particle number N: $\delta/\delta\rho_\sigma(E - \mu N) = 0$. The lagrange multiplier μ is determined from by the total fermion number N, so that N is the only parameter that determines the ground state properties of the system. The authors thus reached the conclusion that there exists a critical value μ_c such that the system ground state

is *Paramagnetic* if $0 \leq \mu \leq \mu_c$ and *ferromagnetic* if $\mu > \mu_c$. The specific value of μ_c is not important here because the authors did not assume the total magnetization to be conserved, whereas in most experiments, the total magnetization is conserved as a consequence an absence of coupling between the effective spin degree of freedom (hyperfine structure) and the rest of the system.

Berdnikov *et al.*[21] and LeBlanc *et al.*[22] reviewed the local density approximation by taking into account of the conservation of magnetization. Two lagrange multipliers μ_σ are introduced to act as chemical potentials for the two spin species and serve to impose the constrains $\int d^3\mathbf{R}\rho_\sigma(\mathbf{R}) = N_\sigma$. The separate constraint on each spin component arises from the assumption that the two spin components correspond to the lowest two Zeeman split hyperfine levels of a Fermi gas. Since the Zeeman splitting near a Feshbach resonance is typically far greater than all other energy scales and the total energy must be conserved in these thermally isolated gases, we arrive at the constraint that the population of the two Zeeman components cannot change for fermionic atoms where the only interaction is between different spin components. Thus, unlike in solid state ferromagnets, the magnetization can be conserved on very long time scales. This mean-field calculation in local density approximation captures many qualitative features expected in a ferromagnetic phase transitions, which are already existing in the simplest Stoner model: as we tune the gas parameter $k_F a$ stronger, there occurs a minimum in kinetic energy, a maximum in potential energy or the cloud size, the emergence of magnetization or a maximum in atom loss rate and so on. Most importantly, the mean field calculation predicted a continuous (second-order) ferromagnetic phase transition at $k_F a = \pi/2$ or $k_F^0 a \approx 1.84$, with k_F being the Fermi wave vector at the trap center in the interacting cloud and k_F^0 the Fermi wave vector at the trap center for the unmagnetized noninteracting gas. The inhomogeneity caused by the trap encoded into local density approximation leads to no correction on this characteristic feature.

The authors [22] also extended the treatment to write the free energy as a functional not only of the density $\rho(\mathbf{r})$, but also of the magnetization order parameter $\mathbf{M}(\mathbf{r})$. This generalization enables the authors to consider not only the density profiles, but also the

spin textures of the interacting two-component Fermi gas in a harmonic trap. They wrote $n_\uparrow(\mathbf{r}) = \frac{1}{2}n(\mathbf{r})[1+m(\mathbf{r})], \quad n_\downarrow(\mathbf{r}) = \frac{1}{2}n(\mathbf{r})[1-m(\mathbf{r})]$ and the energy functional splits into two parts as $E = E_a[n(\mathbf{r})] + E_b[n(\mathbf{r}), m(\mathbf{r})]$ where the first term is the LDA and the second term represents magnetization effects. Promoting the magnetization to vectors and including gradient terms leading to the Landau-Ginzburg form of free-energy functional which describes long-wavelength configurations of the magnetization order parameter

$$E_b = \int d^3\mathbf{R} \frac{\zeta}{2}|\nabla \mathbf{M}|^2 + \frac{\beta}{4}\left(|\mathbf{M}|^2 + \cdots\right)^2, \tag{5.23}$$

where the stiffness $\zeta(\mathbf{R})$ depends on $\mathbf{R}$ only through the density, and it can be computed in the uniform Fermi gas assuming that the magnetization variation is slow on the scale of the interparticle spacing but fast on the length scale over which the total density varies. The above energy functional can then be used to study the energetics of various magnetization patterns in the trapped Fermi gas. The authors compared energies of a hedgehog configuration and a domain wall configuration [22], and also a twist configuration [21] of the magnetization. The conclusion the authors have reached is that in 3D, domain walls are preferred for small traps, while for large traps hedgehog has the lowest energy.

5.4.3 Second order perturbation theory

The pioneering work discussed above suggests that mean field theory predicts a continuous (second-order) ferromagnetic phase transition at $k_F a = \pi/2$ in a two-component Fermi gas at zero temperature and local density approximation leads to negligible qualitative corrections. Duine and MacDonald [28] evaluated the free energy of a *homogeneous* spin-polarized Fermi gas to *second order* in its interaction parameter. Taking into account all contributions to second order in $g = 4\pi a\hbar^2/m$, the energy density of the Hamiltonian for a spatially homogeneous system is then expressed as

$$\varepsilon = \frac{1}{V}\sum_{\mathbf{k},\sigma} \epsilon_{\mathbf{k}} n_\sigma(\epsilon_{\mathbf{k}}) + \frac{g}{V^2} N_\uparrow N_\downarrow - \frac{2g^2}{V^3} \sum_{\mathbf{k}_{1,2,3,4}} \frac{n_{\mathbf{k}_1\uparrow} n_{\mathbf{k}_2\downarrow}(n_{\mathbf{k}_3\uparrow} + n_{\mathbf{k}_4\downarrow})}{\epsilon_{\mathbf{k_1}} + \epsilon_{\mathbf{k_2}} - \epsilon_{\mathbf{k_3}} - \epsilon_{\mathbf{k_4}}}, \tag{5.24}$$

where $n_\sigma(\epsilon_{\mathbf{k}})$ denotes the Fermi distribution and the second sum is over wave vectors such that $\mathbf{k}_1 + \mathbf{k}_2 = \mathbf{k}_3 + \mathbf{k}_4$. Retaining only the leading interaction correction, one recovers the conventional mean field theory. The second order correction takes into account the so-called unitary limit, i.e. the energy dependence of the vacuum scattering amplitude to all orders in $k_F a$, to second order. Note that the interaction is expressed in terms of the Fermi wave vector at the center of a trapped noninteracting Fermi gas. The authors found that mean field theory (or Hatree-Fock theory) underestimates the tendency toward ferromagnetism, which means in second order perturbation theory, the ferromagnetic transition would occur at an even smaller interaction parameter. At zero temperature, the system becomes partially polarized at $k_F a \approx 1.054$ and fully polarized at $k_F a \approx 1.112$. Moreover, the authors claim that *the ferromagnetic transition is first order at low temperatures*, in contrast to mean field theory which predicts that the transition remains continuous down to zero temperature. For higher temperatures, interactions have to be stronger to polarize the system, and for $T > T_{\rm tc} \simeq 0.2 T_F$, the transition is continuous. The authors argued that the coupling of the order parameter to gapless modes leads to nonanalytic terms in the free energy and generically drives the transition first order. Theories of this kind of phase transition are still qualitative. In the current case, the gapless modes that drive the transition first order are particle-hole excitations. The coupling of these excitations to the magnetization is neglected in mean field theory, which therefore always predicts a continuous transition. Eq.(5.24) takes the coupling between the magnetization and the particle-hole excitations into account to lowest order.

Conduit *et al.* [29] revisited the second order perturbation theory and adapted the studies of Duine and MacDonald [28] to the atomic trap geometry. The authors again invoked the local density approximation, which allows the variational minimization as in [22]. This leads to two equations for the particle number density $n_\sigma(\mathbf{r})$ which must be solved self-consistently. The results obtained by this procedure is again in qualitative agreement with experiment. The marked divergence still arises in the experimental prediction of the interaction strength at the onset of ferromagnetism at $k_F^0 a \approx 2.2$ or $k_F a \approx 1.9 \pm 0.2$. The theoretical prediction

from mean field theory, as we recall, is $k_F^0 a \approx 1.9$ or $k_F a = \pi/2$, whereas it is at $k_F^0 a \approx 1.1$ if second order corrections are taken into account. It's even worse than mean field theory in comparison with experiment. This discrepancy prevents the authors from drawing a definitive conclusion on whether the transition is first order or continuous. The authors then argued that the experiment was carried out under nonadiabatic conditions, with atoms prepared in the disordered nonferromagnetic state and the magnetic field ramped to the repulsive side of the resonance in 4.5 ms and then held fixed for a further 2 ms. This discrepancy motivated a simple nonequilibrium theory that takes account of the dynamics of magnetic defects and three-body losses. The formalism or argument developed in this way displays reasonable agreement with experiment.

5.4.4 QMC calculations using SLA

The Jo *et al.* experiment [15] has generated a great deal of theoretical research [22, 30, 31, 32, 33, 34]. The results have been debated as to whether a ferromagnetic transition or a strong correlation effect was seen. Predictions of the critical ratio of interaction strength to interatomic spacing for the ferromagnetic transition from mean field theory [13, 22], second order corrections [28, 34] and QMC calculations [30, 32, 33] are on the order of $k_F a \sim 1$; about two times lower than that from the Jo *et al.* experiment. Quantitative comparison with experiment has not been achieved. In almost all calculations, a positive interaction [30, 32] or a Jastrow factor with two-body nodes [33] is assumed, using the scattering length approximation(SLA). The earliest Fixed-node diffusion Monte Carlo calculations employed the repulsive Pöschl-Teller potential ($k_F a \approx 0.86$) [30], hard spheres or repulsive soft spheres ($k_F a \approx 0.82$) [32] and included backflow effects ($k_F a \approx 0.96$) [33]. For attractive interactions modeled by spherical square wells or attractive Pöschl-Teller potential, either variational Monte Carlo ($k_F a \approx 0.86$) [32] or fixed-node diffusion Monte Carlo [33] ($k_F a \approx 0.89$) calculates the upper-branch metastable state by imposing a nodal condition in the many-body wave function. The nodal condition ensures that the calculation consist of unbound fermionic atoms and no dimers or other bound molecules, by introducing a Jastrow factor in the form

of the scattering solution of the attractive potential corresponding to positive energy. As shown in Sec. (5.5.2), the nodal structure obtained this way deviates significantly from the true nodes in the upper branch. This explains why all these calculations gave results similar to those from repulsive potentials, and all of them reproduced the predicted behavior of the mean field theory and second order corrections.

5.5 Exact diagonalization calculations on grid

With more experimental effort expected in the study of related systems, precise and reliable comparisons from quantum simulations will be important. Yet accurate many-body calculations will not be possible without a quantitative understanding of the effective interactions and their effect on the different states. Even the identification of the atomic scattering state in a dense system requires explanation.

In this section, we explicitly include the molecular bound states and treate the interaction exactly. We use the exact matrix diagonalization methods outlined in Chapter 4 to investigate the energy spectrum of systems of two, three and four spin-$\frac{1}{2}$ fermions interacting through a contact interaction both exactly, and within the scattering length approximation. The energy spectrum as a function of the two-body interaction strength is obtained by using an exact numerical method on a lattice and then extrapolated to the continuum limit. The formation of molecular bound states and the ferromagnetic transition of the excited scattering state are examined systematically as a function of the 2-body scattering length. Identification of the upper branch (scattering states) is discussed and a general approach valid for systems with many particles is given. To compare with the exact solutions, calculations are also made with the SLA by replacing the attractive contact interaction with a zero boundary condition. We show that an adiabatic ferromagnetic transition occurs, but at a critical transition point $k_F a$ much higher than predicted from previous calculations, almost all of which use the scattering length approximation. The exact critical interaction strength calculated in the 4-particle system is consistent with that reported by experiment.

We consider a system of two-component fermions moving in a periodic box with length

L to model a gas of ^{6}Li atoms with two hyperfine species at non-zero density. All lengths are expressed in units of L and all energies in units of $K_0 = \frac{\hbar^2}{2m}(\frac{2\pi}{L})^2$. In the case $a \gg r_0$ (where r_0 is a measure of the effective interaction range), the interatomic potential can be modeled as a regularized δ-function Eq. (5.2). We solve the Schrödinger equation by putting the system on a lattice with n points in each direction and recover the continuum limit by extrapolation. We then approximate the kinetic energy by two different discrete Laplacian operators [35]: (1) the Hubbard model with nearest neighbor hopping and (2) a long range hopping model including up to the next nearest neighbors. We model the bare two-particle interaction by a point contact potential on the grid

$$V^{\text{grid}}(\mathbf{r}, \mathbf{r}') = -\frac{U}{\Delta^3}\delta_{\mathbf{r},\mathbf{r}'}, \tag{5.25}$$

where $\Delta = L/n$ is the grid spacing. Here $U > 0$ is the strength of the attractive interaction; on the repulsive side of resonance $U > U_\infty$, we have positive scattering length for unpaired atoms and the mapping relation between the grid and continuum is [36]

$$\frac{m}{4\pi\hbar^2 a} = \frac{1}{U_\infty} - \frac{1}{U}, \tag{5.26}$$

where the unitarity point $a \to \infty$ occurs at $U_\infty^{-1} = (2\pi)^{-3}\int d^3\mathbf{k}(2\epsilon_{\mathbf{k}})^{-1} = \gamma m/(\hbar^2\Delta)$. Here $\epsilon_{\mathbf{k}}$ is the single particle dispersion relation and γ is a numerical constant defined by the discrete Laplacian. For choice (1) above, $\gamma \approx 0.2527$; for choice (2), $\gamma \approx 0.2190$. When only nearest neighbor hopping is included, our Hamiltonian is the standard attractive Hubbard model, but scaled by $1/\Delta^2$. Note our U value scales as Δ, while in the notation of the Hubbard model, U_∞ is a constant.

In the SLA, U has the opposite sign. In particular, when the scattering length a is large, Eq. (5.25) is replaced by a hard-sphere potential with radius a. If a is smaller than the grid spacing, a finite but negative value of U can be used in the SLA, leading to the repulsive Hubbard model, which clearly has a different strongly interacting or large a limit [31] from that of Eq. (5.25).

To determine the eigenvalues and eigenstates, we start from a set of random trial states $|\psi_\alpha^0\rangle$ where $1 \leq \alpha \leq M$, and evolve the states $|\psi^{i+1}\rangle = (\mathbf{1} - \tau\hat{H})|\psi^i\rangle$. At each step of the evolution, the state vectors are properly symmetrized and orthogonalized. As $i \to \infty$, the states converge to the lowest M eigenstates of the Hamiltonian $\hat{H}$ within a given symmetry sector. The errors are controlled and can be reduced arbitrarily with increasing the number of grid points or number of iterations. As discussed below, the computational cost grows rapidly with system size, but significant reduction can be achieved by invoking symmetries.

5.5.1 Two-particle model

The two-body bound state solution has been obtained in Chapter 2 using the Bethe-Peierls boundary condition and shown in Fig (2.7). To assess the accuracy of iterative diagonalization, we test the method on the two-particle scattering state. At nonzero density, the ground state two-body binding energy and the lowest s-wave two-body scattering energy is plotted in Fig (5.2) as a function of the dimensionless scattering length $k_F a$, where $k_F = (3\pi^2\rho)^{1/3}$ is the Fermi wave vector and ρ the particle density. Both discrete representations of the kinetic energy operator were used and they converge to the same continuum limit: $n \to \infty$; the long-range hopping is found to be less sensitive to the lattice spacing. Solving the two-particle problem also enables us to construct repulsive pseudo-potentials in the SLA by inverting the 2-particle Schrödinger equation.

5.5.2 Two fixed point potentials

The simplest case where the scattering length approximation may fail is the scattering of a single particle off of two fixed contact potentials. This problem can be solved exactly in infinite space [37]. The scattering wave function is written as the sum of the incident plane wave, a wave scattered from potential one, and a wave scattered from potential two; i.e.

$$\psi(\mathbf{r}) = e^{i\mathbf{k}\cdot\mathbf{r}} + A\frac{e^{ik|\mathbf{r}-\mathbf{R}_1|}}{|\mathbf{r}-\mathbf{R}_1|} + B\frac{e^{ik|\mathbf{r}-\mathbf{R}_2|}}{|\mathbf{r}-\mathbf{R}_2|}. \tag{5.27}$$

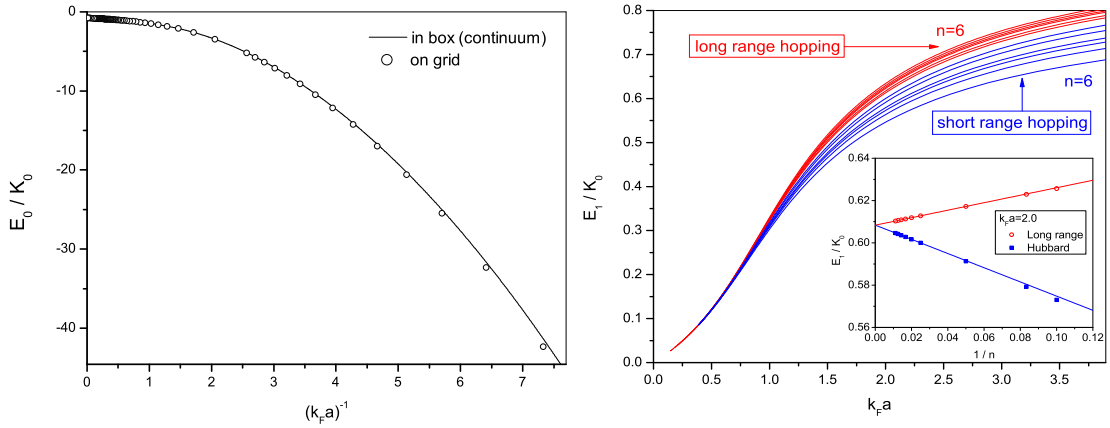

Figure 5.2: **Right**: The two-body binding energy as a function of $(k_F a)^{-1}$. The open circles are numerical solutions on a grid and the line corresponds to the exact analytic solution in a continuum box. Perfect agreement is obtained for large scattering length a and deviation can be observed when the scattering length becomes comparable with the grid spacing. **Left**: The two-body s-wave scattering energy E_1 as a function of $k_F a$ for grid sizes: $n = 6, 8, 10, 12, 20, 40$. The inset shows the scaling with respect to $1/n$ at $k_F a = 2.0$ with grid sizes up to $n = 90$. The long-range hopping model converges to the continuum limit faster than the Hubbard model.

The outgoing amplitude A is given by in terms of the total wave amplitude at $\mathbf{R}_1$ by

$$A = \frac{\eta_0}{k}\left\{e^{i\mathbf{k}\cdot\mathbf{R}_1} + B\frac{e^{ik|\mathbf{R}_1-\mathbf{R}_2|}}{|\mathbf{R}_1-\mathbf{R}_2|}\right\}, \tag{5.28}$$

where η_0/k is the s-wave scattering amplitude for potential one: from the assumption of identical potentials, η_0/k is also the s-wave scattering amplitude from potential two. Similarly,

$$B = \frac{\eta_0}{k}\left\{e^{i\mathbf{k}\cdot\mathbf{R}_2} + A\frac{e^{ik|\mathbf{R}_1-\mathbf{R}_2|}}{|\mathbf{R}_1-\mathbf{R}_2|}\right\}. \tag{5.29}$$

This solution can be verified again by invoking Bethe-Peierls boundary condition. The nodal surface of the zero-energy scattering state is given as the solution of:

$$\frac{1}{|\mathbf{r}-\mathbf{R}_1|} + \frac{1}{|\mathbf{r}-\mathbf{R}_2|} = \frac{1}{a} + \frac{1}{|\mathbf{R}_1-\mathbf{R}_2|}, \tag{5.30}$$

where $\mathbf{R}_1$ and $\mathbf{R}_2$ are the location of the two fixed scatterers. In the SLA, one would model the state by the ground state with nodes defined by $|\mathbf{r}-\mathbf{R}_1| = a$ and $|\mathbf{r}-\mathbf{R}_2| = a$. The nodal

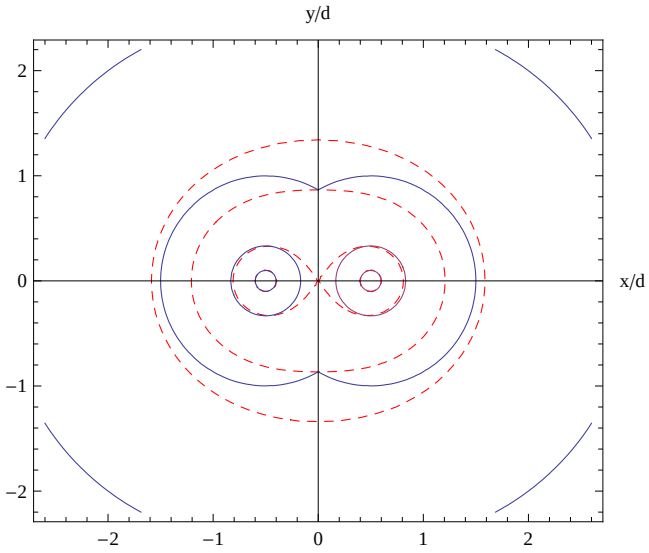

Figure 5.3: Nodal surface for the scattering wavefunction in a potential generated by two fixed particles located at $(\pm d/2, 0, 0)$ in infinite space with $a/d = 1/10, 1/3, 1, 5/2$ (expanding outward), where d denotes the distance between the two fixed scatterers. The solid (blue) lines correspond to the nodes in SLA and the dashed (red) lines to the exact nodes. SLA gives a reasonable approximation to the nodal surface for $a/d < 1$ but the deviation becomes significant for large scattering lengths.

surfaces described by Eq. (5.30) are shown in Fig (5.3) in comparison with corresponding spheres in SLA. Clearly the deviation from SLA becomes significant as $a \sim |\mathbf{R}_1 - \mathbf{R}_2|$. In particular, the spherical surfaces in SLA becomes infinitely large at unitarity limit while Eq. (5.30) gives rise to a finite surface. This result suggests that introducing a node in the two-body Jastrow factor in the form $f(r) \sim (1 - a/r)$ is insuffcient to characterize the effective pairwise repulsion on the upper-branch [38].

To study the effect of the SLA at finite density, we solved the same problem numerically in a finite periodic box. The results are summarized in Fig (5.4). It can be seen from the graph that at large scattering length (i.e. at high density), the SLA significantly overestimates the scattering energy for the 3-body problem, i.e. the effect of low-lying molecular states cannot be ignored. The exact solution achieves a lower energy by distorting the nodal surfaces away from the union of two spheres required by the SLA. As we show below, this also applies to a system of more fermions.

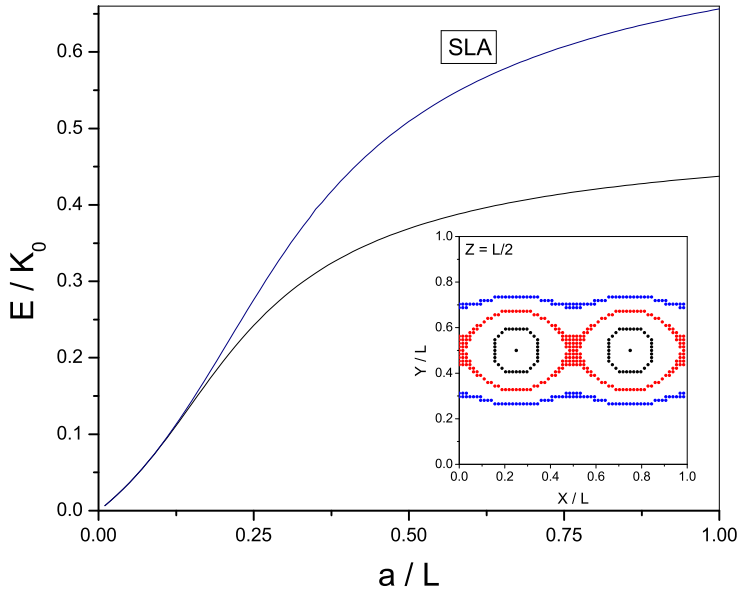

Figure 5.4: The scattering energy of a particle moving in the potential generated by two fixed particles located at $x = L/4$ and $x = 3L/4$, with $y = L/2$ and $z = L/2$. The SLA is obtained by replacing each potential by a hard sphere (zero boundary condition) with the same scattering length. The SLA gives accurate energies in weakly-interacting limit ($a/L < 0.2$) but overestimates the scattering energy for a comparable with L. The inset shows the nodal region ($|\psi_i| < 10^{-4}$) for the scattering states with $a/L = 0.1(\text{black}), 0.2(\text{red}), 0.4(\text{blue})$. The surfaces become noticeably non-spherical for $a/L > 0.1$.

5.5.3 Energetics of four particle model

Now consider a minimal model for the ferromagnetic transition: four spin-1/2 atoms in a cube with periodic boundary conditions and interacting with a contact potential. In short, the spin polarized state $\Psi(1234) = \psi_A(1234) \otimes |\uparrow\uparrow\uparrow\uparrow\rangle$ has a totally antisymmetric spatial part $\psi_A(1234)$: for a contact interaction it is noninteracting with an energy of $4K_0$ in a zero total momentum eigenstate that has translational invariance. On the other hand, the unpolarized states $\Psi(1234) = \psi_{MA} \otimes \chi_{MS} + \psi_{MS} \otimes \chi_{MA}$ are affected by interactions: for a contact interaction, only particles with like spins can be regarded as noninteracting due to the antisymmetries. The permutation symmetries and the associated transformation rules are analyzed in Chapter 4.

For a system of four particles on a grid with n points in each direction, the discretized configuration space has n^{12} grid points. Translational symmetries along the three spatial directions reduce the size of the configuration space by a factor of n^3. Cubic symmetry

of the periodic box reduces the number of independent wavefunction values by a factor of 48 and permutation symmetries give an additional 24-fold reduction. We evolve pairs of non-magnetic states $\{\psi_{MS}, \psi_{MA}\}$ within the reduced domain, and whenever the value of the wavefunctions on a grid point outside the reduced domain is needed in off-diagonal projections, the exterior point is mapped back into the reduced domain by symmetry transformations.

The ferromagnetic transition is identified as the crossing between the lowest singlet scattering state and the fully ferromagnetic state. To investigate the effect of using the SLA in multi-particle scattering process, the attractive contact interaction is replaced by a zero boundary condition and the resulting critical ferromagnetic density is estimated.

Fig. (5.5) shows the energy spectrum of a four-particle system for $n = 10$ as a function of the inverse scattering length $(k_F a_s)^{-1}$. In this calculation, the lowest 30 states were followed. Note that we only considered states with the same symmetries as the ground state, i.e. with even parity with respect to reflection in x, y or z. The resulting energy levels can be classified into three categories by their behavior at strong coupling: two-molecule states, molecule-atom-atom states and four-atom scattering states. Level avoiding [39] can be observed between states belonging to different categories.

The formation of molecular bound states is characterized by the binding energy diverging linearly as $U \to \infty$, or equivalently, $a \to 0^+$. In particular, the ground state wavefunction can be approximately written as $\psi_0(13)\psi_0(24) - \psi_0(14)\psi_0(23)$ where ψ_0 is the two-body bound state, and the ground state energy is approximately twice the two-particle binding energy. As seen in Fig. (5.5) the two-molecule states have an energy slope $(\partial E/\partial U)$ about twice as large as the molecule-atom-atom states. As $U \to \infty$ molecules become tightly bound; their energy spacings can be understood in terms of colliding molecules. For a lattice model, in contrast to a continuum model, the greater the internal binding energy, the greater the total mass of the molecule [40].

The scattering state of strongly repulsive atoms is an excited branch and all cold atom experiments performed in this regime are metastable. In Jo *et al.* experiment, the magnetic

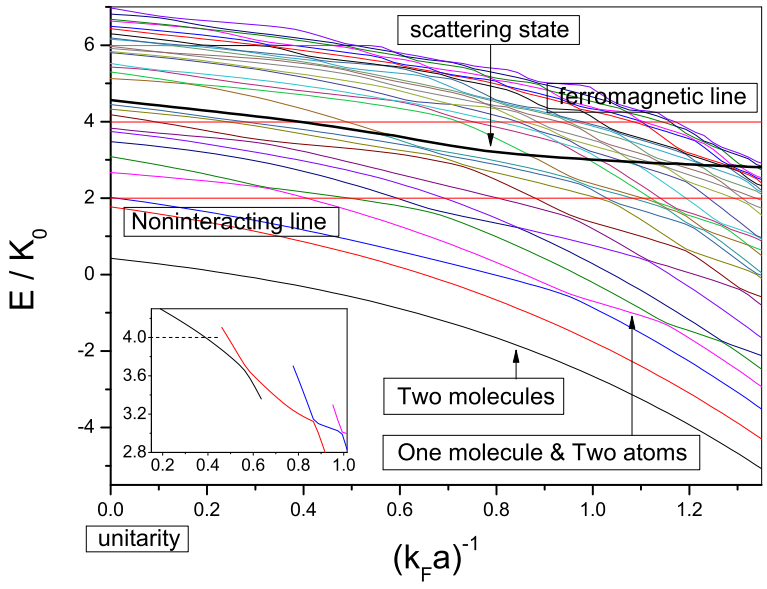

Figure 5.5: The energy spectrum of the lowest 30 s-states of four fermions with contact interactions on a 3D grid with $n = 10$. The energy levels can be classified into two-molecule states, molecule-atom-atom states and four-atom states. The ferromagnetic transition can be identified as the lowest scattering state (heavy dark line) crossing the horizontal ferromagnetic line around $(k_F a_s)^{-1} \approx 0.43 \sim 0.46$. The inset shows an enlargement of the lowest scattering state and the associated avoided crossings.

field ramp (~ 4.5ms) marches toward the resonance from the repulsive side $a \gtrsim 0$. At low density or in the weakly interacting regime, the four-atom scattering state approaches the noninteracting line $2K_0$ and the SLA is an accurate approximation. But there are some difficulties in defining the scattering state at high density or in the strongly interacting regime because of the level avoiding phenomena. As shown in the inset of Fig (5.5), if the coupling coefficient U is tuned toward the resonance U_∞, it is energetically more favorable to jump through the successive avoided crossings. Thus, the change in the scattering energy due to an adiabatic tuning of the interaction can then be determined by following the excited branch curve. It is drawn in bold in Fig (5.5).

There is another way to identify the upper branch (scattering states) quantitatively by using the momentum distribution and the pairing order. First, consider the wavefunctions for the relative motion of two particles interacting through a large scattering length of Eq. (5.2). The zero-energy scattering state in coordinate space $\psi(\mathbf{r}) \propto r^{-1} - a^{-1}$ takes the form $\psi(\mathbf{k}) \propto 4\pi k^{-2} - (2\pi)^3 a^{-1}\delta(\mathbf{k})$ in momentum space and diverges at $\mathbf{k} = 0$. By contrast,

the bound state $\psi(\mathbf{r}) \propto r^{-1}e^{-r/a}$ takes the form $\psi(\mathbf{k}) \propto 4\pi(k^2 + a^{-2})^{-1}$ in momentum space and remains finite at $\mathbf{k} = 0$. The momentum distribution $n(\mathbf{k})$ for scattering states is different from bound states at $\mathbf{k} = 0$: scattering states have a larger fraction of particle occupation at $\mathbf{k} = 0$.

We also consider the pairing order defined by:

$$g_2 \equiv n\Big\langle \sum_{i<j} \delta_{\mathbf{r}_i,\mathbf{r}_j} \Big\rangle_\alpha \tag{5.31}$$

for each state $|\psi_\alpha\rangle$. The quantity g_2 measures double occupancy, and is related to the energy slope:

$$\frac{\partial E_\alpha}{\partial U} = \Big\langle \frac{\partial \hat{H}}{\partial U} \Big\rangle_\alpha = -\frac{1}{\Delta^2 L} g_2. \tag{5.32}$$

For the scattering state, double occupancy decreases monotonically as the interaction strength is increased (see e.g. Ref. [31]). Thus the scattering state in each lattice system is characterized by a vanishing energy slope as $U \to \infty$,

$$g_2 \to 0, \quad \frac{\partial E_\alpha}{\partial U} \to 0, \tag{5.33}$$

as can be seen in Fig (5.5). The pairing density is also related to the tail of the momentum distribution, which describes the short range physics. At large k, the momentum distribution takes the form $n(\mathbf{k}) \to C/k^4$, where the coefficient C is called the *contact* in the Tan relations [41]. In the continuum limit $\Delta \ll a$, the contact C can be related to the energy slope, and hence g_2, through the adiabatic sweep theorem $\frac{dE}{da^{-1}} = -\frac{\hbar^2}{4\pi m} C$, which in our system yields:

$$g_2 = L\Big[\gamma - \frac{\Delta}{4\pi a}\Big]^2 C, \tag{5.34}$$

where γ is the numerical constant appearing in the definition of U_∞. For bound states this gives a finite g_2 and a finite energy slope.

Thus, in addition to the momentum distribution at $\mathbf{k} = 0$, we can identify the scattering state from the other states by the magnitude of g_2: scattering states have a smaller fraction

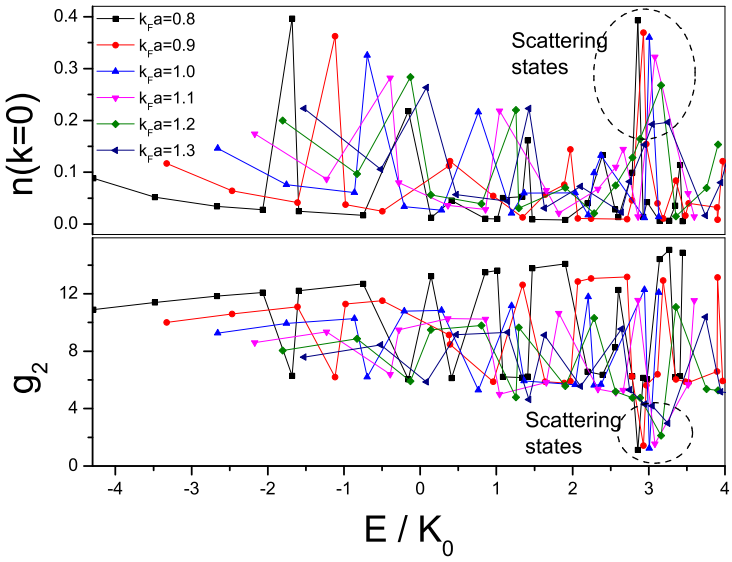

Figure 5.6: The momentum distribution $n(\mathbf{k}=0)$ and the pairing parameter g_2 of the lowest 30 s-states of four fermions with contact interactions on a 3D grid with $n = 10$ versus energy. Scattering states have, by definition, $E/K_0 > 2$ and can be identified by the large magnitude of $n(\mathbf{k}=0)$ and small magnitude of g_2 compared to the other states. The peak structure at the scattering state diminishes as the interaction parameter $k_F a$ increases.

of double occupation $\mathbf{r}_i = \mathbf{r}_j$. Note that the contact C measures the local density of pairs [42]. The momentum distribution $n(\mathbf{k}=0)$ and the pair parameter g_2 are plotted in Fig (5.6) as functions of the energy for $k_F a = 0.8 \sim 1.3$. Scattering states are, by definition, in the range $E/K_0 > 2$ and can be identified by the peaks of $n(\mathbf{k}=0)$ and low values of g_2.

The ferromagnetic transition in the four-atom system occurs when the scattering state energy equals the noninteracting energy, $4K_0$. For a $n = 10$ grid, the transition occurs at $U/U_\infty \approx 1.07$, or equivalently, $(k_F a_s)^{-1} = 0.43 \sim 0.46$. Shown in Fig (5.7) is the energy of the four-particle unpolarized scattering state as a function of the scattering length $k_F a$ on grids with $n = 6, 8, 10, 12$ and their extrapolation to the continuum limit, $n = \infty$. Avoided crossings between levels appear as kinks. The excited scattering state from the solution of the four-particle problem crosses the ferromagnetic line at $k_F a \approx 1.8$, which is in remarkable agreement with the reported experimental value of $k_F a = 1.9 \pm 0.2$ [15].

Also shown is the scattering energy using the SLA; this gives a ferromagnetic transition at $k_F a \approx 1.08 \sim 1.09$ for grid sizes $n = 8, 10, 12$, consistent with previous calculations [13, 14, 30, 32, 33, 34].

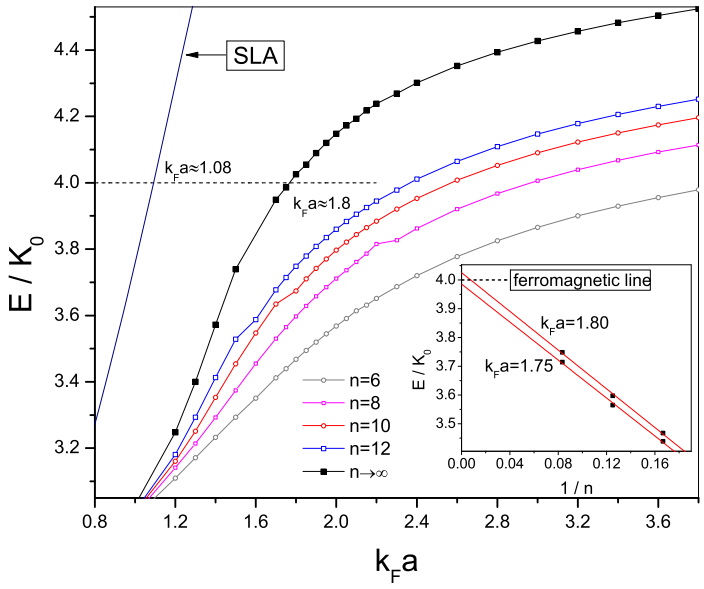

Figure 5.7: The four particle scattering energy as a function of the scattering length. The energy of the ferromagnetic state is shown as the dashed horizontal line. The extrapolation to continuum is performed based on calculations on grids with $n = 6, 8, 10, 12$, which exhibits the 1^{st}-order linear scaling $1/N$ to high accuracy. The transition to the ferromagnetic phase occurs at $k_F a \approx 1.8$ while the SLA gives the transition at $k_F a \approx 1.08$. The inset shows the scaling with respect to $1/n$ near the transition point $k_F a = 1.75$ and 1.8.

The discrepancy between the critical values of $k_F a$ reflects the limitations of perturbation theory in the regime of strong coupling. Compared to repulsive potentials, using Jastow factor with nodes and including backflow effects for attractive potentials improves the result by making nontrivial modifications to the nodal structure, but still gives answers not qualitatively different from the repulsive potential, and fails to reveal the inadequacy of the SLA. These observations suggest that lower-lying molecular states are responsible for delaying the formation of the ferromagnetic phase. However, calculations with more than 4 atoms are needed to determine finite size effects. Such calculations are not feasible with the current method but might be possible with stochastic methods.

5.5.4 Dynamics of four-particle model

Because of the limited lifetime of the strongly interacting gas, however, the magnetic field ramp in experiment is not adiabatic and can lead to different explanations[43, 44]. A recent work [45] takes into account the effect of atom loss by including a fictitious three-body term

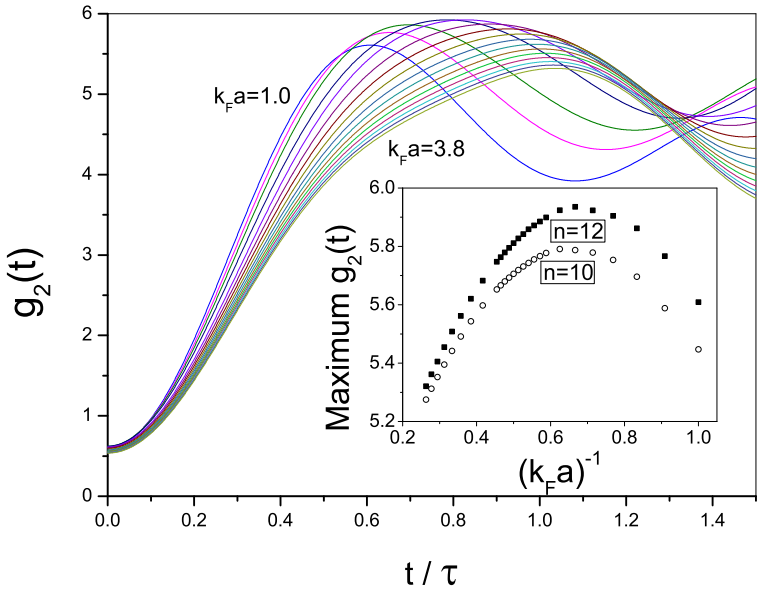

Figure 5.8: The first oscillation period in the evolution of $g_2(t)$ after a quench from a non-interacting state to an interaction strength $k_F a$, where $\tau = \hbar/\epsilon_F$. The inset shows the nonmonotonic behavior of the maximum value of $g_2(t)$ in the first oscillation period as a function of the final interaction strength $k_F a$. This calculation in done for four particles on a grid with $n = 12$.

in the effective Hamiltonian of the Fermi gas and found that the critical interaction strength required to stabilize the ferromagnetic state increases significantly. A full T-matrix analysis [43] suggests that the pairing instability can prevail over the ferromagntic instability and the experimentally measured atom loss rate can be qualitatively explained in terms of the growth rate of the pairing order parameter after a quench.

Thus, it is an interesting problem to study the dynamics of the pairing instability after a quench using the wave functions obtained in this work. Since the contact C is identified as the integral over space of the expectation value of a local operator that measures the density of pairs [42], we characterize the pairing instability by the count of double occupancy g_2 in Eq (5.34). To study the dynamics of the pair formation, we choose the initial state to be the unpolarized four-particle ground-state in the noninteracting limit and expanded in the basis of the lowest 16 eigenstates with the final interaction after the quench. The time evolution is then evaluated using the eigenstate expansion $|\psi(t)\rangle = \sum_m c_m e^{-\frac{i}{\hbar}E_m t}|\phi_m\rangle$. The pairing density $g_2(t) = \langle\psi(t)|g_2|\psi(t)\rangle$ is used to characterize the pair formation and the atom loss into molecules. The evolution diagram of $g_2(t)$ is shown in Fig (5.8). The

nonmonotonic dependence of the maximum value of $g_2(t)$ in the first oscillation period on the final scattering length $k_F a$ after the quench is in qualitative agreement with experiment and the full T-matrix theory [43].

5.5.5 Summary

In summary, we have assessed the accuracy of the scattering length approximation at high density or strong interaction $k_F a \gtrsim 1$. It is demonstrated that if molecular states mix with excitations, non-magnetic states are stabilized. Identification of the upper branch in many-body calculations is discussed. The corresponding nodal structures of the states are examined. The calculated critical interaction strength $k_F a$ for ferromagnetic transition is shown to be underestimated by a factor of two with respect to the scattering length approximation. Although we solved the problem only for 4 particles, this minimal model suffices to show that ignoring the molecular states with the scattering length approximation leads to inaccurate results in the strongly interacting regime. Hence it leads to severe errors in many-body calculations. That we get very good agreement with experimental estimates is encouraging but could be a result of cancellation of errors between the 4 particle system and the thermodynamic limit. We investigated the dynamics of pair formation. Non-monotonic behavior of the pairing parameter $\sum_{i<j} \delta_{\mathbf{r}_i,\mathbf{r}_j}$ is observed as a function of the final interaction strength $k_F a$ after a quench.

5.6 VMC calculations for four particles at unitarity

The unitarity limit describes interacting particles where the range of the interaction is zero and the scattering length is infinite. Quantum Monte Carlo calculations of the ground state energy of dilute Fermion gases on the BCS-BEC crossover [46][47][48] and at unitarity [49][50][51][7] have achieved high accuracies. Precise benchmark calcluation has also been performed to calculate the unpolarized ground state energy of four spin-1/2 fermions [52]. As discussed in Chapter 2, all these QMC calculations employed the short-range approximation by taking an interaction model with a finite range and a fixed (finite or infinite) scattering

length. These models may be in continuous space or on a lattice. Then the zero range limit $r_c \to 0$ should be taken the end of the calculation. In this section, we make the first attempt of a QMC calculation of the unitary Fermion gases directly in the zero-range limit, eliminating the need for short-range approximations employed by existing QMC calculations in literature.

5.6.1 Trial wavefunction

In the zero range model of unitary fermions, one replaces the interaction by Bethe-Peierls boundary conditions on the N-body wavefunction. Thus to perform a variational Monte Carlo calculation of the zero range model, the first step is the construction of a trial wavefunction which satisfies the correct boundary conditions Eq. (2.53) in Chapter 2:

$$\Psi(\mathbf{r}_1, \cdots, \mathbf{r}_i, \cdots, \mathbf{r}_j, \cdots, \mathbf{r}_N) \to A_{ij}(\mathbf{R}_{ij}; \mathbf{r}_{k\neq i,j}) \left(\frac{1}{r_{ij}} - \frac{1}{a} \right) + O(r_{ij}). \tag{5.35}$$

The key requirement is that when two fermions i and j with unlike spins approach each other with the center of mass position fixed and the positions of all the other particles fixed, the singular part of the wavefunction diverges like r_{ij}^{-1}, the constant part must be proportional to a^{-1} and all the other terms vanish as $r_{ij} \to 0$ at least as rapidly as $O(r_{ij})$.

For short-range models, a commonly chosen form [46] on the BEC side of resonance ($a > 0$) is the geminal wavefunction with 2-particle orbitals

$$\Psi = \mathcal{A}\{\phi(r_{11'}\phi(r_{22'}) \cdots \phi(r_{N_\uparrow N_\downarrow}))\}, \tag{5.36}$$

where the indices i and i' refer to particles with up-spin and down-spin respectively, and the function $\phi(r)$ is the two-body bound state solution with energy ϵ_b. This form, however, fails to satisfy the Bethe-Peierls boundary conditions in the zero-range limit even if the pair orbital ϕ does. Take for example a system of four fermions,

$$\Psi = \phi(\mathbf{r}_1 - \mathbf{r}_{1'})\phi(\mathbf{r}_2 - \mathbf{r}_{2'}) - \phi(\mathbf{r}_1 - \mathbf{r}_{2'})\phi(\mathbf{r}_2 - \mathbf{r}_{1'}). \tag{5.37}$$

Suppose particle $\mathbf{r}_1$ and $\mathbf{r}_{1'}$ get close ($\mathbf{r}_1 = \mathbf{r}_{1'} = \mathbf{R}_{11'} \equiv \frac{1}{2}(\mathbf{r}_1 + \mathbf{r}_{1'})$), the orbital $\phi(\mathbf{r}_1 - \mathbf{r}_{1'})$ becomes singular while $\phi(\mathbf{r}_2 - \mathbf{r}_{2'})$ remains finite:

$$\begin{aligned}\Psi &\sim \phi(\mathbf{r}_2 - \mathbf{r}_{2'})\left(\frac{1}{r_{11'}} - \frac{1}{a}\right) - \phi(\mathbf{R}_{11'} - \mathbf{r}_{2'})\phi(\mathbf{r}_2 - \mathbf{R}_{11'}) \\ &\sim \frac{1}{r_{11'}} - \frac{1}{a} - \frac{\phi(\mathbf{R}_{11'} - \mathbf{r}_{2'})\phi(\mathbf{r}_2 - \mathbf{R}_{11'})}{\phi(\mathbf{r}_2 - \mathbf{r}_{2'})}.\end{aligned}$$

In the above expression, the constant term in the limit $r_{1\uparrow 1\downarrow} \to 0$ is

$$\frac{1}{a} + \frac{\phi(\mathbf{R}_{11'} - \mathbf{r}_{2'})\phi(\mathbf{r}_2 - \mathbf{R}_{11'})}{\phi(\mathbf{r}_2 - \mathbf{r}_{2'})} \neq \frac{1}{a} \tag{5.38}$$

and violates Bethe-Peierls boundary condition. The boundary condition can be corrected by introducing Jastrow-like factors $f(\mathbf{r})$ into the geminal wavefunction to suppress the unnecessary terms

$$\Psi = \phi(\mathbf{r}_{11'})\phi(\mathbf{r}_{22})f(\mathbf{r}_{12'})f(\mathbf{r}_{21'})f(\mathbf{r}_{12})f(\mathbf{r}_{1'2'}) - \phi(\mathbf{r}_{12'})\phi(\mathbf{r}_{21'})f(\mathbf{r}_{11'})f(\mathbf{r}_{22'})f(\mathbf{r}_{12})f(\mathbf{r}_{1'2'}), \tag{5.39}$$

where $f(\mathbf{r}) \to O(r)$ as $r \to 0$. For example, take $r_{11'} \to 0$

$$\begin{aligned}\Psi &= \underbrace{\phi(\mathbf{r}_{11'})}_{\left(\frac{1}{r_{11'}} - \frac{1}{a}\right)}\phi(\mathbf{r}_{22'})\underbrace{f(\mathbf{r}_{12'})f(\mathbf{r}_{21'})f(\mathbf{r}_{12})f(\mathbf{r}_{1'2'})}_{\text{const} + O(r_{11'}^2)} - \underbrace{\phi(\mathbf{r}_{12'})\phi(\mathbf{r}_{21'})f(\mathbf{r}_{11'})f(\mathbf{r}_{22'})f(\mathbf{r}_{21})f(\mathbf{r}_{1'2'})}_{O(r_{11'})} \\ &\sim \frac{1}{r_{11'}} - \frac{1}{a} + O(r_{11'}).\end{aligned}$$

Thus the Bethe-Pierls boundary condition is satisfied. This form can be generalized to an unpolarized N-body wavefunction $N_\uparrow = N_\downarrow = N/2$

$$\Psi = \mathcal{A}\left\{\prod_{i=1}^{N/2}\frac{\phi_{ii'}}{f_{ii'}}\right\}\prod_{i<j=1}^{N} f_{ij}. \tag{5.40}$$

Note that the antisymmetrized part includes pairs of unlike spins only and the Jastrow part includes all pairs.

5.6.2 Ground state quantum Monte Carlo algorithms

This section outlines the ground state quantum Monte Carlo methods in the continuum. A basic concept in QMC methods is the walker, a hyper-dimensional particle coordinates:

$$\mathbf{R} = \{\mathbf{r}_1, \mathbf{r}_2, \cdots, \mathbf{r}_N\}. \tag{5.41}$$

The ground state wavefunction is obtained by repeatedly applying a projector $G(\hat{H})$ which inverts the spectrum of the Hamiltonian $\hat{H}$ to an initial trial wavefunction

$$|\Psi^n\rangle = G(\hat{H})|\Psi^{n-1}\rangle. \tag{5.42}$$

The projector may depend on some parameters, for example, the time step τ. In coordinate representation

$$\Psi(\mathbf{R}, t+\tau) = \int d^D\mathbf{R}' G(\mathbf{R}, \mathbf{R}'; \tau)\Psi(\mathbf{R}', t). \tag{5.43}$$

If we interpret $\Psi(\mathbf{R}', t)$ as a probability distribution at time t and $G(\mathbf{R}, \mathbf{R}'; \tau)$ as a transition probability (independent of time) from $\mathbf{R}$ to $\mathbf{R}'$, Eq. (5.43) suggests that $\Psi(\mathbf{R}, t+\tau)$ is the probability distribution at time $t+\tau$. In both diffusion and reptation algorithms, the projector takes the form of the imaginary time evolution operator with an energy shift E_T

$$G(\mathbf{R}, \mathbf{R}'; t) = \langle \mathbf{R}|e^{-t(H-E_T)}|\mathbf{R}'\rangle. \tag{5.44}$$

which satisfies the imaginary-time Schrodinger equation

$$\frac{\partial G(\mathbf{R}, \mathbf{R}'; t)}{\partial t} = (E_T - \hat{H})G(\mathbf{R}, \mathbf{R}'; t) \tag{5.45}$$

with the initial condition $G(\mathbf{R}, \mathbf{R}'; t=0) = \delta(\mathbf{R} - \mathbf{R}')$. The diffusion method interprets the projection as a series of diffusion-drift-branching processes. The Trotter decomposition of the propagator

$$e^{-\tau(\hat{H}-E_T)} \approx e^{-\tau\hat{T}}e^{-\tau(V-E_T)}. \tag{5.46}$$

enables us to consider the effect of each factor separately. The propagator corresponding to the kinetic term $G_0 \equiv e^{-\tau \hat{T}}$ satisfies the diffusion equation

$$\frac{\partial G_0(\mathbf{R}, \mathbf{R}'; \tau)}{\partial \tau} = \frac{1}{2} \nabla^2_{\mathbf{R}} G_0(\mathbf{R}, \mathbf{R}'; \tau) \tag{5.47}$$

and the solution is given by a Gaussian ($m = \hbar = 1$),

$$G_0(\mathbf{R}, \mathbf{R}'; \tau) = \frac{1}{(2\pi\tau)^{DN/2}} e^{-\frac{(\mathbf{R}-\mathbf{R}')^2}{2\tau}}, \tag{5.48}$$

which describes diffusion process in a DN-dimensional space. The propagator corresponding to the interaction term $G_1 \equiv e^{-\tau(V - E_T)}$ satisfies the population equation

$$\frac{\partial G_1(\mathbf{R}, \mathbf{R}'; \tau)}{\partial \tau} = [E_T - V(\mathbf{R})] G_1(\mathbf{R}, \mathbf{R}'; \tau), \tag{5.49}$$

and the solution is given by exponential growth or decay

$$G_1(\mathbf{R}, \mathbf{R}'; \tau) = e^{-\tau[V(\mathbf{R}) - E_T]} \delta(\mathbf{R} - \mathbf{R}'). \tag{5.50}$$

The complete propagator, based on Trotter decomposition in the short time limit $\tau \to 0$, takes the form

$$G(\mathbf{R}, \mathbf{R}'; \tau) \equiv G_0(\mathbf{R}, \mathbf{R}'; \tau) \rho(\mathbf{R}, \mathbf{R}'; \tau), \tag{5.51}$$

where the symmetric branching factor $\rho(\mathbf{R}, \mathbf{R}'; \tau) = e^{-\tau[\frac{V(\mathbf{R}) + V(\mathbf{R}')}{2} - E_T]}$. This decomposition fails for a system with δ-function interactions. A better approach is to determine the exact propagator for two particles and then use that to construct a many-body propagator. In three dimensions, the imaginary time evolution operator $G_{12} \equiv e^{-\tau \hat{\mathcal{H}}_{12}}$ associated with the Hamiltonian for the relative motion of two particles interacting through the regularized δ-function potential

$$\hat{\mathcal{H}}_{12} = -\frac{\hbar^2}{m} \nabla^2_{\mathbf{r}_{12}} + \frac{4\pi\hbar^2 a}{m} \delta(\mathbf{r}_{12}) = \frac{\hbar^2}{m} \left[-\nabla^2_{\mathbf{r}} + 4\pi a \delta(\mathbf{r}) \right]_{\mathbf{r}=\mathbf{r}_{12}} \tag{5.52}$$

can be evaluated analytically ($m = \hbar = 1$) [53]

$$\rho_\delta(\mathbf{r}, \mathbf{r}'; \tau) \equiv \frac{G_{12}(\mathbf{r}, \mathbf{r}'; \tau)}{G_0(\mathbf{r}, \mathbf{r}'; \tau)} = 1 + \left(\frac{2\tau}{rr'}\right) \exp\left[-\frac{(r+r')^2 - |\mathbf{r}-\mathbf{r}'|^2}{4\tau}\right] \left[1 + \frac{\sqrt{\pi\tau} e^{z^2} \mathrm{erfc}(z)}{a}\right], \tag{5.53}$$

where $z = \frac{r+r'-2\tau/a}{\sqrt{4\tau}}$ and $G_0(\mathbf{r}, \mathbf{r}'; \tau) = (4\pi\tau)^{-3/2} \exp(-\frac{|\mathbf{r}-\mathbf{r}'|^2}{4\tau})$ is the propagator associated with the non-interacting Hamiltonian Eq. (5.48) for relative motion in three dimensions. There are several noteworthy limiting regimes

$$\begin{aligned}
&\lim_{a\to\pm\infty} G_{12}(\mathbf{r}, \mathbf{r}'; \tau) = G_0(\mathbf{r}, \mathbf{r}'; \tau) + \left(\frac{2\tau}{rr'}\right) \frac{1}{(4\pi\tau)^{3/2}} \exp\left[-\frac{(r+r')^2}{4\tau}\right], \quad \text{unitary limit} \\
&\lim_{a\to 0^-} G_{12}(\mathbf{r}, \mathbf{r}'; \tau) = G_0(\mathbf{r}, \mathbf{r}'; \tau), \quad \text{BCS limit} \\
&\lim_{a\to 0^+} G_{12}(\mathbf{r}, \mathbf{r}'; \tau) = \frac{1}{2\pi a} \exp\left(\frac{\tau}{a^2}\right) \exp\left(-\frac{r+r'}{a}\right), \quad \text{BEC limit.}
\end{aligned} \tag{5.54}$$

which agree with the solutions of Schrödinger equation obtained in Chapter 2, Sect. (2.3). Then the many-body propagator associated with the Hamiltonian Eq. (5.1) for a system of spin-1/2 fermions can again be approximated by Eq. (5.51) with $\rho(\mathbf{R}, \mathbf{R}'; \tau) = e^{\tau E_T} \prod_{i=1}^{N_\uparrow} \prod_{j=1}^{N_\downarrow} \rho_\delta(\mathbf{r}_i - \mathbf{r}_j, \mathbf{r}'_i - \mathbf{r}'_j; \tau)$ [54, 55]. This is called the *pair-product* form of the propagator or action. The basic diffusion algorithm can be summarized as follows:

- Sample $\Psi^{(0)}(\mathbf{R})$ with the Metropolis algorithm: generate M_0 walkers $\mathbf{R}_1, \cdots, \mathbf{R}_{M_0}$;
- Diffuse each walker as $\mathbf{R}' = \mathbf{R} + \xi$, where ξ is sampled from $g(\xi) = (2\pi\tau)^{-DN/2} e^{-\xi^2/2\tau}$;
- For each walker, compute the factor $p = \rho(\mathbf{R}, \mathbf{R}'; \tau)$, and branch the walker:
  - If $p \leq 1$, the walker survives with probability p;
  - If $p > 1$, the walker continues and new walkers with same coordinates are created;
  - Number of copies of the current walker $= \lfloor p + \eta \rfloor$ where $\eta \in (0, 1)$.
- Adjust E_T so that the population fluctuates around target M_0.
  - Population control feedback: $E_T(t+T) = E_T(t) + \frac{1}{T} \ln\left(\frac{M_0}{M(t)}\right)$.

- After many iteractions, the walkers are distributed with the ground state distribution $\Psi_0(\mathbf{R})$.

5.6.3 Importance sampling algorithm of variational Monte Carlo

Multiply each side of Eq. (5.43) by a trial wavefunction Ψ_T and define $P(\mathbf{R}) = \Psi_T(\mathbf{R})\Psi(\mathbf{R})$,

$$P(\mathbf{R}, t+\tau) = \int d^D\mathbf{R}'\tilde{G}(\mathbf{R}, \mathbf{R}'; \tau)P(\mathbf{R}', t), \tag{5.55}$$

where the importance sampled propagator is $\tilde{G}(\mathbf{R}, \mathbf{R}'; \tau) = \Psi_T(\mathbf{R})G(\mathbf{R}, \mathbf{R}'; \tau)\Psi_T^{-1}(\mathbf{R}')$. Rewrite the logarithmic ratio

$$\begin{aligned}
\log\frac{\Psi_T(\mathbf{R})}{\Psi_T(\mathbf{R}')} &= \log\Psi_T(\mathbf{R}) - \log\Psi_T(\mathbf{R}') \\
&\approx (\mathbf{R}-\mathbf{R}')\cdot\nabla\log\Psi_T(\mathbf{R}') + \frac{1}{2}[(\mathbf{R}-\mathbf{R}')\cdot\nabla]^2\log\Psi_T(\mathbf{R}') \\
&\approx (\mathbf{R}-\mathbf{R}')\cdot\nabla\log\Psi_T(\mathbf{R}') + \frac{\tau}{2}\nabla^2\log\Psi_T(\mathbf{R}') \\
&= (\mathbf{R}-\mathbf{R}')\cdot\mathbf{V}(\mathbf{R}') - \frac{\tau}{2}\mathbf{V}^2(\mathbf{R}') - \tau\Psi_T^{-1}(\mathbf{R}')\hat{H}_0\Psi_T(\mathbf{R}'),
\end{aligned}$$

where we have defined the quantum velocity $\mathbf{V}(\mathbf{R}) = \nabla_{\mathbf{R}}\log\Psi_T(\mathbf{R})$. Combined with Eq. (5.51),

$$\tilde{G}(\mathbf{R}, \mathbf{R}'; \tau) \equiv G_0(\mathbf{R}, \mathbf{R}' + \tau\mathbf{V}'; \tau)\rho(\mathbf{R}, \mathbf{R}'; \tau). \tag{5.56}$$

where $\rho(\mathbf{R}, \mathbf{R}'; \tau) = e^{-\tau[\frac{E_L(\mathbf{R})+E_L(\mathbf{R}')}{2} - E_T]}$ and the local energy $E_L(\mathbf{R}) = \Psi_T^{-1}(\mathbf{R})\hat{H}\Psi_T(\mathbf{R})$. The importance sampling diffusion algorithm can be summarized as

- Sample initial walkers from $|\Psi_T(\mathbf{R})|^2$: generate M_0 walkders $\mathbf{R}_1, \cdots, \mathbf{R}_{M_0}$;
- Drift and diffuse each walker $\mathbf{R}' = \mathbf{R} + \xi + \tau\mathbf{V}(\mathbf{R})$, where ξ sampled from $g(\xi) = (2\pi\tau)^{-DN/2}e^{-\xi^2/2\tau}$;
- For each walker, compute the factor $p = \rho(\mathbf{R}, \mathbf{R}'; \tau)$, and branch the walker:
  - If $p \leq 1$, the walker survives with probability p;
  - If $p > 1$, the walker continues and new walkers with same coordinates are created;

– Number of copies of the current walker $= \lfloor p + \eta \rfloor$ where $\eta \in (0, 1)$.

- After many iteractions, the walkers distribute as the ground state $\Psi_T(\mathbf{R})\Psi_0(\mathbf{R})$.

Due to time-step error, even if the trial wavefunction is chosen to be the exact ground state wavefunction $\Psi_T = \Psi$, $E_L = E_0$, the probability distribution $|\Psi_0|^2$ is actually sampled only in the continuous time limit $\tau \to 0$. This problem can be solved by interpreting the drift-diffusion part as a Metropolis accept/reject process where $T(\mathbf{R}, \mathbf{R}'; \tau) \equiv G_0(\mathbf{R}, \mathbf{R}' + \tau\mathbf{V}; \tau)$ is the so-called proposal probability. Walker drifts, diffuses and the move is accepted with probability

$$q = \min\left\{1, \frac{|\Psi_T(\mathbf{R}')|^2 T(\mathbf{R}, \mathbf{R}'; \tau)}{|\Psi_T(\mathbf{R})|^2 T(\mathbf{R}', \mathbf{R}; \tau)}\right\}. \tag{5.57}$$

The advantages of the importance sampling algorithm are

- The drift term pushes the walkders where Ψ_T is large;
- $E_L(\mathbf{R})$ is better behaved than the potential $V(\mathbf{R})$;
- As $\Psi \to \Psi_0(\mathbf{R})$, $E_T \to E_0$ and braching factor is smaller.

The importance sampling algorithm of variational Monte Carlo is simply the diffusion algorithm without branching.

5.6.4 VMC energy for four fermions at unitarity

We now present a preliminary VMC calculation on the zero range model of four spin 1/2 unitary fermions moving in a periodic box with length L. Using the notation in Sect. (5.6.1), we use the following parameterization

$$\phi(\mathbf{r}) = \phi_0(\mathbf{r}) + \alpha r e^{-\beta r^2}, \tag{5.58}$$

where α and β are variational parameters and $\phi_0(\mathbf{r})$ satisfies the Bethe-Peierls boundary condition. Possible choices for $\phi_0(\mathbf{r})$ are the exact solution of the two-body problem in the same periodic box, or one can use trigonometric substitutions for cartesian coordinates to

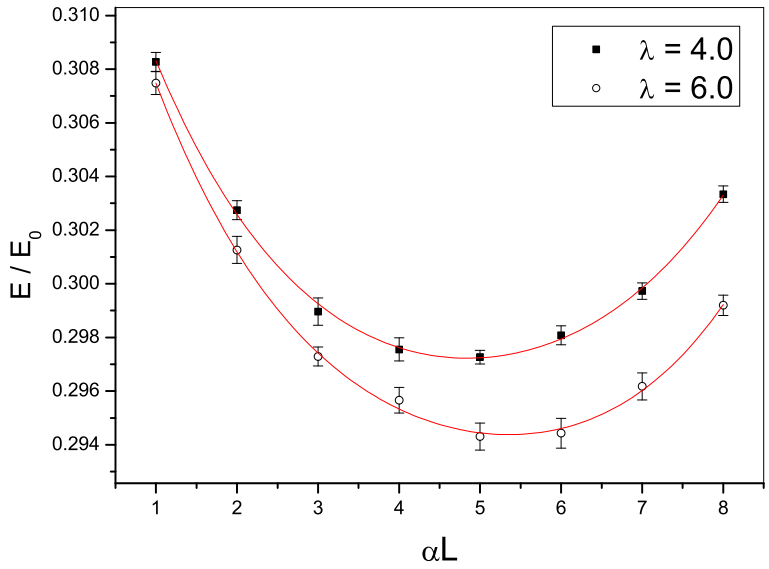

Figure 5.9: The energy expectation value of four spin 1/2 fermions at unitarity as a function of the variational parameter α for $\lambda = 4.0, 6.0$, expressed in units of E_0, the energy for the non-interacting system. The results are fitted to a 4^{th} order polynomial.

impose periodic boundary conditions

$$\phi_0(\mathbf{r}) = \frac{e^{-\tilde{r}/a}}{\tilde{r}}, \tag{5.59}$$

where $\tilde{r} = \sqrt{\sum_{\alpha=1}^{3} \tilde{x}_\alpha^2}$ and $\tilde{x}_\alpha = \frac{L}{\pi} \sin(\frac{\pi x_\alpha}{L})$. At unitarity, the scattering length $a = \infty$. The factors $f(\mathbf{r})$ which vanishes as $O(r^\nu)$ as $r \to 0$ are chosen to take the form

$$f(\mathbf{r}) = \left(\frac{\lambda r}{1 + \lambda r} \right)^{\nu \exp(-r^2/R_c^2)}. \tag{5.60}$$

where λ and ν are variational parameters, and R_c is fixed approximated 15% of the length of box. We fix the parameter $\beta = 10$, $\nu = 1$ and perform a simple optimization of the energy with respect to parameters α and λ, as shown in Fig. (5.9). The results obtained from minimization over the two parameters α and λ is about $E/E_0 \approx 0.29$, where E_0 is the energy for the non-interacting system. The benchmark calculation in literature gives $E/E_0 \approx 0.21$ [52]. Optimizations over more parameters are required to obtain improve the quality of the trial wavefunction before the application of the diffusion or reptation

algorithm.

5.6.5 Summary

In this section, by constructing a many-body wavefunction satisfying the Bethe-Peierls boundary conditions, we attempted the first variational Monte Carlo calculations of the zero-range model of unitary Fermion gases, eliminating the need for short-range approximations employed by existing QMC calculations in literature. The pair-product form for the many-body imaginary time evolution operator is also provided to facilitate the ground state Monte Carlo calculation (diffusion or reptation) if the variational trial wavefunction is fully optimized.

References

[1] Stefano Giorgini, Lev P. Pitaevskii, and Sandro Stringari. Theory of ultracold atomic fermi gases. *Rev. Mod. Phys.*, 80:1215–1274, Oct 2008.

[2] Kerson Huang and C. N. Yang. Quantum-mechanical many-body problem with hard-sphere interaction. *Phys. Rev.*, 105:767–775, Feb 1957.

[3] T. D. Lee and C. N. Yang. Many-body problem in quantum mechanics and quantum statistical mechanics. *Phys. Rev.*, 105:1119–1120, Feb 1957.

[4] J. Bardeen, L. N. Cooper, and J. R. Schrieffer. Microscopic theory of superconductivity. *Phys. Rev.*, 106:162–164, Apr 1957.

[5] C. J. Pethick and H. Smith. *Bose-Einstein Condensation in Dilute Gases*. Cambridge University Press, first edition, 2002.

[6] D. S. Petrov, C. Salomon, and G. V. Shlyapnikov. Weakly bound dimers of fermionic atoms. *Phys. Rev. Lett.*, 93:090404, Aug 2004.

[7] J. Carlson, Stefano Gandolfi, Kevin E. Schmidt, and Shiwei Zhang. Auxiliary-field quantum monte carlo method for strongly paired fermions. *Phys. Rev. A*, 84:061602, Dec 2011.

[8] D. M. Eagles. Possible pairing without superconductivity at low carrier concentrations in bulk and thin-film superconducting semiconductors. *Phys. Rev.*, 186:456–463, Oct 1969.

[9] A. J. Leggett, A. (Editor) Pekalski, and J. (Editor) Przystawa. *Modern Trends in the Theory of Condensed Matter*. Springer, 1980.

[10] W. J. Heisenberg. Zur theorie des ferromagnetismus. *Z. Phys.*, 49:619–636, 1928.

[11] F. Bloch. Bemerkung zur elektronentheorie des ferromagnetismus und der elektrischen leitf?higkeit. *Zeitschrift fr Physik A Hadrons and Nuclei*, 57:545–555, 1929. 10.1007/BF01340281.

[12] F. H. Zong, C. Lin, and D. M. Ceperley. Spin polarization of the low-density three-dimensional electron gas. *Phys. Rev. E*, 66:036703, Sep 2002.

[13] E. C. Stoner. *Phil. Mag.*, 15:1018, 1933.

[14] R. A. Duine and A. H. MacDonald. Itinerant ferromagnetism in an ultracold atom fermi gas. *Phys. Rev. Lett.*, 95:230403, Nov 2005.

[15] Gyu-Boong Jo, Ye-Ryoung Lee, Jae-Hoon Choi, Caleb A. Christensen, Tony H. Kim, Joseph H. Thywissen, David E. Pritchard, and Wolfgang Ketterle. Itinerant ferromagnetism in a fermi gas of ultracold atoms. *Science*, 325(5947):1521–1524, 2009.

[16] Z. Hadzibabic, S. Gupta, C. A. Stan, C. H. Schunck, M. W. Zwierlein, K. Dieckmann, and W. Ketterle. Fiftyfold improvement in the number of quantum degenerate fermionic atoms. *Phys. Rev. Lett.*, 91:160401, Oct 2003.

[17] Jelena Stajic, Qijin Chen, and K. Levin. Density profiles of strongly interacting trapped fermi gases. *Phys. Rev. Lett.*, 94:060401, Feb 2005.

[18] Qijin Chen, Jelena Stajic, and K. Levin. Thermodynamics of interacting fermions in atomic traps. *Phys. Rev. Lett.*, 95:260405, Dec 2005.

[19] Joseph Kinast, Andrey Turlapov, John E. Thomas, Qijin Chen, Jelena Stajic, and Kathryn Levin. Heat capacity of a strongly interacting fermi gas. *Science*, 307(5713):1296–1299, 2005.

[20] Wilhelm Zwerger. Itinerant ferromagnetism with ultracold atoms. *Science*, 325(5947):1507–1509, 2009.

[21] Ilya Berdnikov, P. Coleman, and Steven H. Simon. Itinerant ferromagnetism in an atom trap. *Phys. Rev. B*, 79:224403, Jun 2009.

[22] L. J. LeBlanc, J. H. Thywissen, A. A. Burkov, and A. Paramekanti. Repulsive fermi gas in a harmonic trap: Ferromagnetism and spin textures. *Phys. Rev. A*, 80:013607, Jul 2009.

[23] B. DeMarco and D. S. Jin. Onset of fermi degeneracy in a trapped atomic gas. *Science*, 285(5434):1703–1706, 1999.

[24] M. J. Holland, B. DeMarco, and D. S. Jin. Evaporative cooling of a two-component degenerate fermi gas. *Phys. Rev. A*, 61:053610, Apr 2000.

[25] M. Houbiers, R. Ferwerda, H. T. C. Stoof, W. I. McAlexander, C. A. Sackett, and R. G. Hulet. Superfluid state of atomic ^{6}Li in a magnetic trap. *Phys. Rev. A*, 56:4864–4878, Dec 1997.

[26] L. Salasnich, B. Pozzi1, A. Parola1, and L. Reatto. Thermodynamics of multi-component fermi vapours. *J. Phys. B: At. Mol. Opt. Phys.*, 33:3943, Apr 2000.

[27] T. Sogo and H. Yabu. Collective ferromagnetism in two-component fermi-degenerate gas trapped in a finite potential. *Phys. Rev. A*, 66:043611, Oct 2002.

[28] R. A. Duine and A. H. MacDonald. Itinerant ferromagnetism in an ultracold atom fermi gas. *Phys. Rev. Lett.*, 95:230403, Nov 2005.

[29] G. J. Conduit and B. D. Simons. Repulsive atomic gas in a harmonic trap on the border of itinerant ferromagnetism. *Phys. Rev. Lett.*, 103:200403, Nov 2009.

[30] G. J. Conduit, A. G. Green, and B. D. Simons. Inhomogeneous phase formation on the border of itinerant ferromagnetism. *Phys. Rev. Lett.*, 103:207201, Nov 2009.

[31] Chia-Chen Chang, Shiwei Zhang, and David M. Ceperley. Itinerant ferromagnetism in a fermi gas with contact interaction: Magnetic properties in a dilute hubbard model. *Phys. Rev. A*, 82:061603, Dec 2010.

[32] S. Pilati, G. Bertaina, S. Giorgini, and M. Troyer. Itinerant ferromagnetism of a repulsive atomic fermi gas: A quantum monte carlo study. *Phys. Rev. Lett.*, 105:030405, Jul 2010.

[33] Soon-Yong Chang, Mohit Randeria, and Nandini Trivedi. Ferromagnetism in the upper branch of the feshbach resonance and the hard-sphere fermi gas. *Proceedings of the National Academy of Sciences*, 108(1):51–54, 2011.

[34] Alessio Recati and Sandro Stringari. Spin fluctuations, susceptibility, and the dipole oscillation of a nearly ferromagnetic fermi gas. *Phys. Rev. Lett.*, 106:080402, Feb 2011.

[35] James R. Chelikowsky, N. Troullier, K. Wu, and Y. Saad. Higher-order finite-difference pseudopotential method: An application to diatomic molecules. *Phys. Rev. B*, 50:11355–11364, Oct 1994.

[36] Y. Castin. Simple theoretical tools for low dimension bose gases. *J. Phys. IV France*, 116:89–132, 2004.

[37] K. A. Brueckner. Multiple scattering corrections to the impulse approximation in the two-body system. *Phys. Rev.*, 89:834–838, Feb 1953.

[38] Soon-Yong Chang, Mohit Randeria, and Nandini Trivedi. Ferromagnetism in the upper branch of the feshbach resonance and the hard-sphere fermi gas. *Proceedings of the National Academy of Sciences*, 108(1):51–54, 2011.

[39] L. D. Landau and E. M. Lifshitz. *Quantum Mechanics, Non-relativisitic Theory.* Butterworth-Heinemann, third edition, 1981.

[40] Daniel C. Mattis. The few-body problem on a lattice. *Rev. Mod. Phys.*, 58:361–379, Apr 1986.

[41] Shina Tan. Large momentum part of a strongly correlated fermi gas. *Annals of Physics*, 323(12):2971 – 2986, 2008.

[42] Eric Braaten and Lucas Platter. Exact relations for a strongly interacting fermi gas from the operator product expansion. *Phys. Rev. Lett.*, 100:205301, May 2008.

[43] David Pekker, Mehrtash Babadi, Rajdeep Sensarma, Nikolaj Zinner, Lode Pollet, Martin W. Zwierlein, and Eugene Demler. Competition between pairing and ferromagnetic instabilities in ultracold fermi gases near feshbach resonances. *Phys. Rev. Lett.*, 106:050402, Feb 2011.

[44] Hui Zhai. Correlated versus ferromagnetic state in repulsively interacting two-component fermi gases. *Phys. Rev. A*, 80:051605, Nov 2009.

[45] G. J. Conduit and E. Altman. Effect of three-body loss on itinerant ferromagnetism in an atomic fermi gas. *Phys. Rev. A*, 83:043618, Apr 2011.

[46] G. E. Astrakharchik, J. Boronat, J. Casulleras, and S. Giorgini. Equation of state of a fermi gas in the bec-bcs crossover: A quantum monte carlo study. *Phys. Rev. Lett.*, 93:200404, Nov 2004.

[47] G. E. Astrakharchik, J. Boronat, J. Casulleras, and S. Giorgini. Momentum distribution and condensate fraction of a fermion gas in the bcs-bec crossover. *Phys. Rev. Lett.*, 95:230405, Dec 2005.

[48] S. Y. Chang, V. R. Pandharipande, J. Carlson, and K. E. Schmidt. Quantum monte carlo studies of superfluid fermi gases. *Phys. Rev. A*, 70:043602, Oct 2004.

[49] J. Carlson, S.-Y. Chang, V. R. Pandharipande, and K. E. Schmidt. Superfluid fermi gases with large scattering length. *Phys. Rev. Lett.*, 91:050401, Jul 2003.

[50] Vamsi K. Akkineni, D. M. Ceperley, and Nandini Trivedi. Pairing and superfluid properties of dilute fermion gases at unitarity. *Phys. Rev. B*, 76:165116, Oct 2007.

[51] Xin Li, Jind řich Kolorenč, and Lubos Mitas. Atomic fermi gas in the unitary limit by quantum monte carlo methods: Effects of the interaction range. *Phys. Rev. A*, 84:023615, Aug 2011.

[52] Shahin Bour, Xin Li, Dean Lee, Ulf-G. Meißner, and Lubos Mitas. Precision benchmark calculations for four particles at unitarity. *Phys. Rev. A*, 83:063619, Jun 2011.

[53] K. Wódkiewicz. Fermi pseudopotential in arbitrary dimensions. *Phys. Rev. A*, 43:68–76, Jan 1991.

[54] Michele Casula, D. M. Ceperley, and Erich J. Mueller. Quantum monte carlo study of one-dimensional trapped fermions with attractive contact interactions. *Phys. Rev. A*, 78:033607, Sep 2008.

[55] D. M. Ceperley. Path integrals in the theory of condensed helium. *Rev. Mod. Phys.*, 67:279–355, Apr 1995.